國立臺灣大學醫學院暨工學院醫學工程研究所

博士論文

Department of Biomedical Engineering

College of Medicine and College of Engineering

National Taiwan University

Doctoral Dissertation

應用超臨界流體技術製備基於 PLA/PBAT/PBS/nHA 之生物可降解支架於組織之應用

Investigation of the PLA/PBAT/PBS/nHA-Based Biodegradable Scaffold Using Supercritical Fluid Technology for Tissue Applications

陳沛華

Pei-Hua Chen

指導教授: 林峯輝 博士

Advisor: Feng-Huei Lin, Ph.D.

中華民國 一一四 年 七 月

July 2025

doi:10.6342/NTU202502722

國立臺灣大學博士學位論文
口試委員會審定書

PhD DISSERTATION ACCEPTANCE CERTIFICATE
NATIONAL TAIWAN UNIVERSITY

應用超臨界流體技術製備基於 PLA/PBAT/PBS/nHA
之生物可降解支架於組織之應用

Investigation of the PLA/PBAT/PBS/nHA-Based Biodegradable Scaffold Using Supercritical Fluid Technology for Tissue Applications

本論文係 陳沛華（D10528004）在國立臺灣大學 醫學院暨工學院醫學工程研究所 完成之博士學位論文，於民國 114 年 07 月 15 日承下列考試委員審查通過及口試及格，特此證明。

The undersigned, appointed by the Department of Biomedical Engineering on 15-07-2025 have examined a PhD dissertation entitled above presented by Pei-Hua Chen (D10528004) candidate and hereby certify that it is worthy of acceptance.

口試委員 Oral examination committee:

林峰輝		
（指導教授 Advisor）		
陳致宇	張玉宏	姜仲霖
蘇元復	陳顯禮	劉華昌

系主任/所長 Director: 林頌然

doi:10.6342/NTU202502722

序言與謝辭

身為一位長期投入臨床第一線的骨科醫師，深知骨科疾病與骨缺損對病患生活品質所帶來的重大影響。在診療的過程中，我見證了眾多病患因嚴重骨折、骨缺損或骨質疏鬆而苦無理想重建材料，進而導致復原延宕、功能受限，甚至喪失行動能力。正因如此，促使我走入實驗與研究的領域，希冀透過材料科學與生醫技術的融合，進一步改善臨床治療成效，造福更多病患。

本研究能夠順利完成，首先必須感謝我的指導教授 — 林峯輝教授。自研究開始進行時，林教授即以其深厚的學術素養與研究經驗，引導我從臨床問題中萃取研究核心，並一步步協助我建立清晰的研究架構，使本論文能臻完善。老師嚴謹治學的精神，將永遠銘刻於我心，是我研究路途上的重要典範。

誠摯感謝論文上給予支持的各位教授 — 蘇至善教授、陳錦文教授。各位教授於口試期間提供精闢見解與實質建議，協助我進一步反思與修正論文內容，使研究更具深度與可行性，給予我極大的助益，深表感激。本研究得以順利推展，亦有賴於臺北醫學大學以及衛生福利部雙和醫院骨科部的支持與協助。感謝研究期間提供資源、儀器設備與寶貴意見的所有同仁們，您們的專業與配合讓研究歷程更加順利，也使這份工作更加具備臨床實用價值。

最後，我要感謝我的家人，尤其是父母。感謝他們在我攻讀博士學位期間無怨無悔地支持、理解與包容。當研究陷入瓶頸之時，家人的鼓勵與陪伴成為我最大的力量來源。若無他們默默的犧牲與奉獻，我不可能走到今日。

博士論文的完成不僅是一段學術旅程的終點，更是我作為醫師與研究者角色整合的重要里程碑。未來我將秉持初心，讓研究不止於論文，而能真正回饋於臨床、造福於患者。

doi:10.6342/NTU202502722

摘要

本研究之宗旨在於開發一種具備良好物理、機械特性，同時具備良好生物可相容性的新型生物可分解性、高分子共混材料，期望能應用於人體組織工程的領域。本研究計畫以聚乳酸（polylactic acid, PLA）、聚丁二酸丁二酯（poly(butylene succinate), PBS）與聚己二酸/對苯二甲酸丁二酯（poly(butylene adipate-co-terephthalate), PBAT）為基礎，在其中添加不同比例含量之奈米羥基磷灰石（nanohydroxyapatite, nHA），以作為功能性填料，製備 PLA/PBS/PBAT/nHA 共混材料，並系統性探討其物理性質、熱力學性質、力學性質與材料發泡後相關之變化。

本研究將此共混材料依照混和比例分為兩實驗組，分別為 A 實驗組（PLA 含量 70 wt%）與 B 實驗組（PLA 含量 80 wt%），各系列製備四種不同 nHA 添加量之樣品，均以雙螺桿擠出機，應用特殊的混練條件溫度，進行熔融混煉製程。共混材料，後續透過傅立葉轉換紅外光譜（FTIR）、X 光繞射分析（XRD）確認各組成物的存在與相容性；並以示差掃描量熱儀（DSC）分析其結晶行為。後續進行拉伸與衝擊強度測試，測試的結果顯示，當適量 nHA 添加其中，可顯著提升共混材料所表現的機械性質。其後透過掃描式電子顯微鏡（SEM）與穿透式電子顯微鏡（TEM）進一步觀察材料表面的特性，與 nHA 在基材中的分散性，SEM 與 TEM 結果均顯示 nHA 可作為有效成核劑，有助於在共混材料中提高結晶度與整體結構均勻性。熱重分析（TGA）驗證了，共混後的材料具備良好的熱性質與穩定性；吸水率實驗則指出，材料擁有良好的親水性，有利後續之生物應用。

本研究亦利用了超臨界二氧化碳（supercritical carbon dioxide, SC-CO_2）作為發泡的製程選項，進行 PLA/PBS/PBAT/nHA 共混材料之發泡處理，製作出有利細胞組織生長的多孔隙結構。本研究亦探討了不同操作策略，對孔洞結構的影響。過程

doi:10.6342/NTU202502722

中，本實驗共設計八種發泡程序，包括基本高溫高壓飽和後快速釋壓（1T-1P），以及引入中間溫度與壓力調控之策略，如中間溫度冷卻（2T-1P）、中間溫度冷卻並快速釋壓（2T-2P）與階梯式釋壓（2T-2P，stepwise ΔP）。SEM 觀察發現，(2T-2P，階梯式 ΔP)策略可產生雙峰孔洞的結構，其中小型泡孔尺寸為 105–164 μm，大型泡孔尺寸為 476–889 μm，顯示可透過操作條件有效控制泡孔分布。該結果可由經典成核理論、氣體溶解度原理與高分子熔體強度變化加以解釋。本研究最後亦評估各發泡後樣品之各項特性，包括泡孔平均尺寸、泡孔密度、膨脹比、孔隙率與開孔率等指標，並以水接觸角評估其親水性。利用動態力學分析儀（DMA）進行壓縮測試，實驗結果之應力–應變曲線顯示，發泡產品剛性與發泡策略密切相關。

綜合以上各實驗所述，本研究成功建立了製備 PLA/PBS/PBAT/nHA 共混材料之流程，與建立了發泡技術的加工條件。本研究亦製造了具有組織支架潛力應用的材料，並提供了不同孔洞大小之製備發泡參數，為未來生醫材料的開發，提供一定的數值參考依據。

關鍵詞：聚乳酸（PLA）、聚丁二酸丁二酯（PBS）、聚己二酸/對苯二甲酸丁二酯（PBAT）、奈米羥基磷灰石(nHA)、超臨界二氧化碳發泡、雙峰泡孔結構、發泡策略。

doi:10.6342/NTU202502722

Abstract

This research aims to develop an innovative biodegradable polymer blend with excellent physical, mechanical, and biocompatible properties for potential utilization in tissue engineering. The study aimed at the fabrication of PLA/PBS/PBAT/nHA composites, using polylactic acid (PLA), poly(butylene succinate) (PBS), and poly(butylene adipate-co-terephthalate) (PBAT) as the polymer matrix, and nanohydroxyapatite (nHA) as a functional filler. The influence of nHA content on the physical, thermal, mechanical, and foaming behaviors of the blends were comprehensively analyzed.

Two groups of blend formulations were designed based on PLA content: Group A with 70 wt% PLA and Group B with 80 wt% PLA. Each group consisted of four variations with different nHA concentrations. All samples were prepared using a twin-screw extruder method through a melting process. The presence and compatibility of the components were verified using FTIR and XRD, while DSC was employed to evaluate crystallization behavior. Results from tensile and impact strength tests indicated that appropriate nHA loading markedly improved the mechanical performance of the blends. SEM and TEM analyses revealed that nHA served as an effective nucleating agent, improving the crystallinity and overall structural uniformity of the composites. TGA confirmed the thermal stability of the composites, and water absorption and contact angle experiment demonstrated that nHA addition enhanced hydrophilicity, making the material suitable for biomedical applications.

Furthermore, the foaming characteristics of PLA/PBS/PBAT/nHA blends were studied using supercritical carbon dioxide (SC-CO_2) as a physical foaming agent, aimed

doi:10.6342/NTU202502722

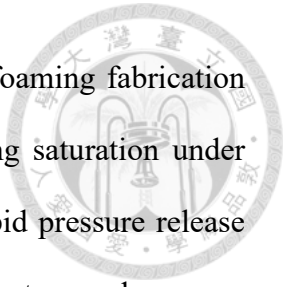

at generating porous scaffolds conducive to cell growth. Different foaming fabrication techniques were investigated, including a primary process involving saturation under conditions of saturation temperature and pressure, succeeded by rapid pressure release (1T-1P), and second strategies including intermediate steps of temperature and pressure regulation, such as cooling at an intermediate temperature (2T-1P), cooling at an intermediate temperature combined with rapid decompression (2T-2P), and stepwise decompression (2T-2P, stepwise ΔP). SEM observations revealed that the (2T-2P, stepwise ΔP) generated a bimodal cellular architecture with small cells sized between 105–164 μm and large cells from 476–889 μm, indicating that foam morphology can be precisely regulated through the adjustment of processing parameters. Key foaming characteristics such as average cell size, expansion ratio, cell density, porosity, and open-cell content were evaluated. Hydrophilicity was assessed through water contact angle measurements. Compression tests conducted using DMA revealed that foam stiffness was closely related to the foaming strategy, reflecting changes in mechanical performance.

In summary, this study successfully established the processing techniques for PLA/PBS/PBAT/nHA composites and their foaming behavior, proposing material formulations and processing parameters with strong potential for tissue scaffold applications. These findings offer important insights and constitute a key reference for advancing future biomedical materials development.

Keywords: polylactic acid, poly(butylene succinate); poly(butylene adipate-co-terephthalate); nanohydroxyapatite; polymer blends tissue scaffold; supercritical carbon dioxide foaming; bimodal cell structure.

doi:10.6342/NTU202502722

目次

doi:10.6342/NTU202502722

doi:10.6342/NTU202502722

圖次

doi:10.6342/NTU202502722

doi:10.6342/NTU202502722

doi:10.6342/NTU202502722

表次

doi:10.6342/NTU202502722

第一章 緒論

近年來隨著醫學領域研究的發展，在精準醫療以及再生醫學的快速發展下，生物醫用材料的研究已躍升為跨領域整合科學的重要樞紐之一，其涵蓋了生物工程、材料科學與臨床應用等領域[1]。隨著人口逐漸老化，重視慢性疾病與重大創傷治療需求的提升，開發新型高性能、可客製化之生物材料，成為了目前醫療研究與產學合作的目標[1,2]。特別是在組織工程（tissue engineering）領域中，新型材料的研究專注於製造可作為支架（scaffold）的生物材料。組織工程支架不僅需提供細胞附著、遷移與增殖的三維支持平台，更需在細胞生成與組織修復期間，可以隨時間降解並被人體組織取代，最後達到「結構支持」與「功能再生」的雙重需求[3-5]。目前臨床上，已有許多研究，專注於利用組織工程製成的植入物，在人體上使用的案例[5-7]。

1-1 生物醫用材料在組織工程中的角色與發展趨勢

根據先前眾多文獻的結果，目前用於治療嚴重骨缺損的骨科手術數量正逐年上升[8]，促使用於骨科植入物的研發材料受到關注[9-13]。針對骨組織工程的設計與骨科材料的製備，已有多篇綜述文獻進行深入探討，其中涵蓋了製程與功能性質等關鍵議題[14-17]。目前臨床上用於骨修復手術的植入材料中，金屬製品仍佔主流地位，但其所帶來的永久性留置、骨吸收干擾及金屬離子釋出可能產生的相關問題，逐漸促使研究者尋求更安全、可降解且具功能性的替代材料[18]。特別是在處理大面積骨缺損或複雜骨折時，傳統金屬植入物的功能已無法完全滿足目前在骨科手術上的臨床需求。因此，開發兼具機械支持、骨誘導性、生物可吸收性與細胞友善性的骨組織支架材料，成為近年不同領域研究的重點項目。相較之下，高分子複合材料

doi:10.6342/NTU202502722

因具備可調控性、不同的生物降解性，以及簡易的加工性能，在未來非常具有應用潛力[19-21]。

生物材料依其來源與結構組成，可大致分為天然高分子材料（例如多醣類、纖維素、膠原蛋白等）、金屬與合金材料（例如鎂合金、鈦合金、不鏽鋼等）、生物陶瓷（例如羥基磷灰石、生物活性玻璃等）、合成高分子材料（例如聚乳酸、聚己內酯）及複合材料系統。這些材料各自具備特定優勢與應用潛能，常被依據不同的臨床應用需求進行選擇與加工[5,7]。例如金屬材料因強度高與生物惰性佳，常應用於永久性植體，如人工關節與骨釘；而生物陶瓷則通常具備良好的骨傳導性，常用於骨科填料與塗層材料[22,23]。然而，從材料科學與臨床實務觀點來看，人體可降解高分子材料因其可分解性、以及製程的多樣性，被認為是在支架材料領域中具潛力的發展方向[24,25]。

在組織工程中，具備多孔隙生物結構的材料尤為重要，其孔隙率、孔洞尺寸及互通性（interconnectivity）對於細胞附著、生長、養分交換及組織整合均有顯著影響[26]。孔洞結構可促進組織新生並提高體內外之營養與代謝廢物的傳輸效率[27]。然而，理想的孔洞尺寸與結構需依不同組織類型調整，如骨組織與皮下組織在孔隙需求上即有所差異。文獻指出，多孔隙生醫材料，目前已廣泛應用於心血管系統、神經系統、骨組織、與眼科等領域，並獲得廣泛的討論[26]。

1-2 可降解高分子材料的潛力與 PLA 之應用限制

根據近年文獻報導，可分解性質的生醫材料在臨床上具有多項重要應用，包括組織工程、醫學影像、藥物傳、疫苗載體、生物感測、骨折固定、韌帶重建以及半月板修復等[28,29]。目前研究上，最廣泛應用的可分解合成高分子材料，包括聚己內酯（poly(ε-caprolactone), PCL）、聚乳酸（polylactic acid, PLA）、聚乙醇酸（polyglycolic

doi:10.6342/NTU202502722

acid, PGA）等等[20,28]。聚乳酸（polylactic acid, PLA）作為一種最常見、應用最廣泛的生物可分解性高分子，其具備有良好的生物相容性，以及可預期的人體降解特性。PLA 在體內降解後會產生乳酸，後續可被人體吸收代謝，不造成毒性的累積，且已被美國 FDA 核准用於多項醫療器材[28]。然而，PLA 的缺點是天然脆性與低延展性，使其在骨組織工程的應用上受到限制，特別是在需要耐衝擊或承受複雜應力條件的情況下，其力學性能表現仍不足。此外，PLA 的親水性較差，難以有效支持細胞貼附與增殖，也限制了其生物功能性。因此，如何提升 PLA 的延展性、機械特性與強度、與生物相容性等，成為研究與改質的關鍵議題[29]。

目前針對 PLA 的改質策略主要包括三大方向：高分子共混（polymer blending）、共聚反應（copolymerization）以及無機或有機填料複合（composite modification）[30,31]。其中，透過與其他具柔韌性的高分子進行共混，被認為是一個簡便且高效的改善方式。常見的共混材料包括聚己內酯（PCL）、聚丁二酸丁二酯（PBS）、聚丁二酸-對苯二甲酸丁二酯（PBAT）等。這些高分子具備有良好的可塑性與延展性，也具有良好的生物可分解特性，能在維持降解性的同時，顯著提升整體材料的機械與生物性能[32-38]。

在過去的研究中，PLA 與 PBS 或 PBAT 所形成的二元共混材料，已經過廣泛的研究與探討。研究顯示這類共混系統，不僅可加強 PLA 的脆性與機械強度，同時還可展現出良好的相容性，與加強製程的可調控性[33-38]。後續，可利用超臨界二氧化碳（SC-CO_2）技術進行物理性發泡，此發泡過程更進一步延伸了此類共混材料，在三維多孔支架製造的應用可能[39]。SC-CO_2 發泡法具有無溶劑、可控孔隙結構、低殘留毒性等優勢，這些特性使其適合應用於生醫支架製備。在適當的飽和壓力，與特定的溫度條件下，可誘導複合材料形成內部的連續性多孔結構，進而促進細胞遷移，促進與組織的再生[40]。

doi:10.6342/NTU202502722

此外，為賦予高分子材料更強的骨傳導與骨細胞活性，導入無機奈米粒子如奈米羥基磷灰石（nano-hydroxyapatite, nHA）已成為熱門策略[29]。nHA 為人體骨組織內部主要的無機成分，具備良好的生物活性、可以誘導骨細胞生長，與增加細胞間訊息傳導能力。nHA 的添加可有效模擬骨基質的分子結構，進而提升細胞黏附、骨細胞分化，最終達到增加新生骨的生成能力[41]。研究亦指出，nHA 與高分子基體之界面的交互作用，能有效提升複合材料的機械穩定強度，與強化其生物機能性，這類特性在多孔隙支架生物結構中更顯重要[29,42-46]。

然而，目前文獻中多集中於二元高分子系統（如 PLA/PBS 或 PLA/PBAT）或單一聚合物中加入 nHA 的複合性材料之研究[35,36,38]，對於 PLA/PBS/PBAT 三元共混物同時添加 nHA 的研究報導相當有限。儘管目前已有少數文獻，探討三元高分子系統在不同領域應用中的機械性質，但針對其於骨填補材料中發泡行為、雙峰泡孔結構影響、以及發泡條件控制之系統性探討仍屬欠缺[45,47,48]。PBAT 雖具高度柔韌性與延展能力，在共混系統中可顯著提升共混材料之整體韌性，惟目前其與 nHA 之交互作用機制與對發泡結構之影響仍缺乏研究[42,43]。

本研究分為兩個主要部分進行探討與實驗：(一)首先針對 PLA/PBS/PBAT 三元系統，進一步添加 nHA，進行熱物理性質，以及機械性質的探討。在調配不同比例的成分之下，經由雙軸混煉(twin screw extrusion)獲得四成分混煉材料，經由各種物性與機械性質測量，構築具備有良好生物力學強度，以及與骨組織生物活性的 PLA/PBS/PBAT/nHA 複合材料的最佳組成。經由物性測量，嘗試觀察 nHA 的加入，是否能顯著提升材料之親水性質與強度，並在穿透式電子顯微鏡(TEM)下，觀察下審視 nHA 是否均勻分佈於高分子共混材料之基質中[48]。此一新穎生物基共混材料具有良好的應用潛力，適合用於組織工程中具三維立體孔隙結構之支架材料。(二)經由第一部分的熱物性與機械性質測量之後，獲得最佳組成的四成分 PLA/PBS/PBAT/nHA 複合材料，再利用超臨界二氧化碳（SC-CO_2）進行發泡，嘗

doi:10.6342/NTU202502722

試獲得類似骨材的雙峰結構(bimodal cell structure)的多孔性材料，探討最佳發泡操作條件，針對各發泡條件所獲得的實驗數據，經由熱力學與古典成核理論加以闡述其結果，並透過分析發泡後材料的機械性質，可進一步釐清其與發泡製程條件之間的關聯性。

1-3 超臨界二氧化碳（SC-CO_2）發泡技術於組織支架製造之優勢

近年來，超臨界二氧化碳（SC-CO_2）發泡技術因其環保性、高滲透能力與溫和的操作條件，成為製備多孔生醫支架的重要方法之一[26,27,49,50]。該技術利用二氧化碳在特殊的溫度壓力條件下，能達到超臨界狀態且具備類似氣體與液體的雙重特性，能有效滲透至高分子材料內部，使其在後續減壓階段發泡形成孔洞結構。利用 SC-CO_2 製備多孔 PLA 或其複合材料的相關應用也已被廣泛提出[51]。理想的多孔支架需具開孔結構與良好互通性，以促進細胞進入與營養交換。相較於化學發泡劑，使用物理發泡劑，例如先前文獻中已廣泛被使用的二氧化碳（CO_2）或氮氣（N_2）進行高分子發泡製程，具有更高的環保性，因此已廣泛應用於各類研究中[50-52]。相較於傳統使用有機溶劑、或其他化學溶液發泡的方法，SC-CO_2 發泡技術不僅無需使用潛在毒性溶劑，避免殘留風險，同時能有效控制孔洞大小、分布與開孔率，特別適合用於製備應用於組織工程之中。這些支架必須具備良好的立體孔隙特性，以利細胞黏附與移動、並且提供養分與代謝物質交換的管道，以利後續的組織再生過程[51,52]。然而，對於含有半結晶 PLA 的聚合物共混系統而言，在 SC-CO_2 中進行發泡過程則較多複雜的條件，原因是由於二氧化碳可誘導PLA的結晶行為，使其發泡行為更具挑戰性[52]。

Yang 等人[53]在固定飽和壓力 16 MPa 下進行 PLA 發泡實驗，建立了基於 PLA 結晶結構的發泡溫度窗口，並指出在特定的發泡溫度與發泡壓力條件下，發

doi:10.6342/NTU202502722

泡結果會形成具有兩種以上孔徑大小與體積膨脹比的孔隙結構。Chen 等人[54]採用具不同 D-異構物含量的兩種 PLA 樣品進行研究，並使用二階段溫度誘導發泡法（two-step temperature-induced foaming process）；在首階段，於 16 MPa 與 150 °C 條件下飽和一小時，接著在調整後的二段溫度下進行發泡，最終建立出相對應的發泡溫度窗口。Huang 等人[55]則提出多階段溫度飽和策略，在固定壓力條件下，於高溫進行第一次飽和並冷卻後，再次加熱與冷卻，最終快速減壓形成泡孔，最終製得具雙峰孔徑開孔結構的 PLA 發泡製成物，其結果適用於組織工程之應用。

此外，將 PLA 與特殊的可降解聚合物，例如聚丁二酸丁二酯（Polybutylene Succinate, PBS）共混進行 SC-CO_2 發泡的相關研究亦有報導，其中 PBS 相被認為可作為異質成核位置，有助於氣泡的生成。Li 等人[56]探討了在固定發泡壓力 10.3 MPa 下，PBS 含量與發泡溫度對 PLA/PBS 共混系統的發泡行為影響。實驗中，先將樣品加熱至 180 °C 消除熱歷史，再降至較低溫度進行單階段發泡，並確立了有助於形成開孔結構的材料組成與溫度範圍。Wang 等人[57]採用類似的熔融飽和發泡策略，成功製備高膨脹開孔 PLA 孔洞材料，用於介面分離應用。

Yu 等人[36]進一步分析了 PLA 與 PBS 的共混材料中發泡的行為。由於 PBS 熔融強度低，可降低共混材料中的黏度特性，而 PLA 與 PBS 間的相界面亦可促進氣泡成核。研究結果指出，當 PLA/PBS 重量比為 80/20 時，透過兩階段壓力釋放過程，可產生高度開孔結構與雙峰孔徑分布。PBAT 的發泡行為則由 Wang 等人[58]探討，其結合 SC-CO_2 與氮氣作為共發泡劑，於單一減壓程序中有效改善 PBAT 泡孔的收縮現象。

近年來，針對聚合物加入添加劑後，雙階段減壓的發泡策略亦逐漸受到關注[59-61]。其方法包含先將樣品置於 SC-CO_2 中飽和一定時間，首次降壓至中間壓力後保持特定的時間，再迅速釋壓至常壓完成發泡程序。透過該策略可同時誘導形成大

doi:10.6342/NTU202502722

小不同的泡孔，其中第一次緩慢減壓形成大孔，第二次快速釋壓則生成小孔[60,61]。透過調整飽和條件與降壓速率，可有效控制泡孔大小與分布，製備出適合不同臨床組織工程所需之雙模態結構。

為了達到組織工程材料中，對於多功能、降解性醫療材料的需要，本研究提出了具有創新潛力的材料設計策略：以具有優異生物可相容性，同時具備人體可降解性的高分子材料聚乳酸（PLA）為主要基材，在製程中加入具延展性與增韌功能的聚對苯二甲酸丁二酯-己二酸酯（PBAT），與具有熱穩定及化學穩聽性質的聚丁二酸丁二酯（PBS）與作為輔助材料，最後加入具優秀骨誘導活性的奈米級羥基磷灰石（nHA）作為無機混和材料，共同構築一種新型四元可生物降解之複合高分子材料。此材料再經由超臨界二氧化碳，進行環保之物理性發泡，最後獲得適用於生物支架的複合性多孔高分子材料。

1-4 本研究之創新性與研究目標

據目前已知文獻中，尚未見針對添加奈米羥基磷灰石（nHA）之 PLA/PBS/PBAT 三元共混聚合物進行超臨界二氧化碳（SC-CO_2）發泡的相關探討或研究。由於 PBS 與 PBAT 相分散於 PLA 基材中，其聚合物間的界面有望成為潛在的成核位置，有助於促進發泡過程。本研究計畫以 PLA/PBS/PBAT 共混體系中，添加 nHA 後的混合物，採用 SC-CO_2 發泡技術進行多孔支架之製備。透過調控發泡參數（如飽和壓力、飽和時間、發泡溫度與減壓速率），系統性探討不同配方與製程條件對泡孔結構、孔徑分佈與最終機械性能的調控與影響。本研究亦導入逐漸減壓（gradual pressure reduction）發泡策略，期望在控制泡孔成核與生長行為的同時，實現雙峰泡孔結構的形成，即同時擁有大尺寸與小尺寸孔洞。這樣的結構能更有效模擬人體骨組織的多孔特性，有助於細胞從外部移行至支架內部，並促進

doi:10.6342/NTU202502722

供應血管之生成與新生骨形成，從而大幅提升此支架在臨床組織工程應用中的潛力。

此外，本研究也將針對微觀結構、孔隙率測定、基本物理機械性質測試等多項實驗方法，全面評估所製備支架材料的臨床潛力。針對不同製備上的可控條件（如溫度、壓力、維持時間等）對材料之多孔結構與物理性能之影響，進行系統性的分析，進一步探討各成分比例，在複合材料中之影響，最終期望能提供一套具有臨床應用潛力之骨填補生物材料，不僅為未來可降解多相生醫材料的研究與臨床應用建立了理論與實務基礎，亦透過綜合性的設計與實驗分析，提出一種兼具創新性與實用性的可降解多孔支架設計方案，為骨組織工程支架材料的開發提供全新的科學依據與應用方向。

doi:10.6342/NTU202502722

第二章 實驗裝置與方法

2-1 實驗材料

聚乳酸（Polylactic acid, PLA）使用產品為 Ingeo 4032D，由 NaturalWorks LLC, Minnetonka, MN, USA 製造，為一種半結晶型高分子材料，D-乳酸含量約為 1.4 wt%。PLA 的熔點為 155–170 °C，其熔融指數（在 190 °C、2.16 kg 條件下）為 7 g/10 min。聚丁二酸丁二酯（Poly(butylene succinate), PBS）使用產品為 Bio PBS FZ 91，由 PTT MCC Biochem Co. Ltd., Bangkok, Thailand 生產，亦屬於半結晶型脂肪族聚酯材料。PBS 的熔點為 115 °C，其熔融指數（在 190 °C、2.16 kg 條件下）為 5 g/10 min。聚（己二酸-對苯二甲酸丁二酯）（Poly(butylene adipate-co-terephthalate), PBAT）選用產品為 ecoflex F blend C1200，來自 BASF SE, Ludwigshafen, Deutschland，為一種柔性脂肪-芳香族共聚酯，具有良好之延展性與生物可降解性。PBAT 的熔點為 110–120 °C，其熔融指數（在 190 °C、2.16 kg 條件下）為 2.7–4.9 g/10 min。奈米羥基磷灰石（Nano-hydroxyapatite, nHA）購自 Sigma-Aldrich, UNI-ONWARD Corp, Taiwan，其純度高於 97 wt%，平均粒徑約為 72–80 奈米，分子量約為 502.3，熔點約為 1100 °C。其化學登記號碼（CAS）為 12167-74-7。這些高分子材料的基本物理特性與機械性質列於 Table 2-1。

2-2 複合材料共混物的製備

本研究使用之 PLA、PBS 與 PBAT 聚合物，在共混前均先於真空烘箱（Channel, VO45L, KO TSAO specialty Instrument & Supplies Co. Ltd, Taipei, Taiwan）中以 80 °C 乾燥 6 小時，以去除材料中的殘留水分，避免於加工過程中產生預期之外的熱裂解。這些未添加奈米羥基磷灰石（nHA）之共混材料樣品名稱與配方組成列於 Table 2-2 中。所有共混材料均以雙螺桿押出機（Process 11, Thermo Fisher

doi:10.6342/NTU202502722

Scientific, Waltham, MA, USA）進行製備，押出機配備有體積式送料器與條狀造粒機構。該押出機螺桿直徑為 11 mm，長徑比（L/D ratio）為 40。乾燥後之聚合物顆粒被送入押出機料斗進行共混操作。押出機具有六個加熱區，從進料口至模頭，各區域之溫度可獨立控制。

聚合物共混時之送料速率設定為 1 kg/h，螺桿轉速則為 50 rpm。各溫控區之設定溫度依序為 200–210–220–225–225–220 °C。在押出完成後，熔融物經由水浴冷卻，再進行條狀造粒。造粒後之樣品再行充分乾燥，準備進行標準化機械性質測試。用於測試之樣品以壓縮成型法製備，壓模條件為 200 °C 熱壓 5 分鐘，再冷卻至正常室溫。冷卻後可獲得之薄板樣品厚度為 1.2 ± 0.2 mm，並於塑膠袋中密封保存，置於陰涼處備測。此外，對於含 nHA 配方之共混樣品，其製備程序亦完全相同。這些不同配方之樣品後續將用於熱性質分析、化學組成鑑定、微觀形貌觀察與吸水性測試等多項實驗。關於雙軸混煉置備高分子摻合物(polymer blend)的操作示意圖，表示於圖 2-1。

Table 2-2 列出了本研究，於第一階段混煉實驗中 PLA 基高分子共混物的配方。樣品編號 PLA60 代表一種含有 60 wt% PLA 以及其餘兩類高分子（25 wt% PBS 和 15 wt% PBAT），且未添加奈米羥基磷灰石（nHA）的共混物。Table 2-2 中列出的樣品系列 A 與 B 分別包含不同添加量的 nHA。以樣品系列 A 為例，樣品 A0 表示含 70 重量百分濃度(wt%)之 PLA、20 重量百分濃度(wt%)之 PBS、10 重量百分濃度(wt%)之 PBAT，且未添加 nHA 的共混體。樣品 A3、A5 與 A7 則在相同 PLA/PBS/PBAT 配比下，分別添加 3、5 及 7 wt% 的 nHA。樣品系列 B 則包含 80 wt% PLA、15 wt% PBS、5 wt% PBAT，分別於 B0、B3、B5 與 B7 樣品中添加 0、3、5 及 7 wt% 的 nHA。文獻指出，含有 nHA 的奈米複合材料可有效提升骨組織的生物可相容性[13,43-46,62,63]，故本研究也使用 nHA 作為材料之一，其中添加的 nHA 平均粒徑介於文獻中報導的範圍內[63]。

doi:10.6342/NTU202502722

第二階段發泡實驗條配混配比為 PLA/PBS/PBAT = 80/15/5（wt%），並額外添加 5 wt% nHA。共混熔融後的產品經由水浴冷卻，隨即顆粒化並充分乾燥。接著，以壓縮模塑法於 200°C 加熱 5 分鐘，製備出尺寸為 3 mm × 7 mm，厚度 2 mm 的矩形試片。試片冷卻至室溫後，裝袋密封保存於低溫環境，待後續發泡實驗使用。發泡實驗的實驗流程圖，如圖 2-2 所示，混煉之後的高分子試片，置入含溫控器之高壓槽，藉由 ISCO 高壓幫浦，將二氧化碳打入高壓槽中，再預先設定之溫度與壓力策略下，進行含四種成分之混練高分子材料發泡。

2-3 分析與測試方法

2-3-1 傅立葉轉換紅外光譜分析（Fourier-transform infrared spectroscopy, FTIR）

本研究使用傅立葉轉換紅外光譜儀（FTIR, Thermo Fisher Scientific Summit LITE）搭配 ATR 技術，分析本實驗之複合材料內部的化學結構。掃描次數為 32 次，解析度為 4 cm^{-1}，測試波數範圍為 4000–500 cm^{-1}。

2-3-2 X 光繞射分析（X-ray diffraction analysis, XRD）

本實驗之複合材料的結晶強度，使用 X 光繞射儀（XRD, Rigaku）進行分析，輻射源為 Cu-Kα（λ = 1.54 Å），操作條件為 40 kV 與 15 mA。掃描速率為 10°/min，掃描範圍為 2θ = 5° 至 40°。

2-3-3 示差掃描量熱儀分析（Differential scanning calorimetry, DSC）

本實驗使用示差掃描量熱儀（DSC, Hitachi High-Tech Scientific DSC-7000, 日本）在氮氣環境下，進行熱性與結晶性行為分析。樣品重量為 4–6 mg，第一次加熱從 30 °C 以 10 °C/min 升溫至 200 °C 並保溫 5 分鐘以消除熱歷史，之後冷卻至−50 °C 並再次加熱至 200 °C。記錄熔點、冷結晶溫度、玻璃轉移溫度、冷結晶焓與熔融焓等數據。

doi:10.6342/NTU202502722

此外，亦進行非等溫結晶行為分析，樣品加熱至 200 °C 後冷卻至 50 °C，冷卻速率分別調控為 2.5、5、7.5 與 10 °C/min，在此條件下記錄熱流曲線以進行分析。

2-3-4 機械性質測試

本研究之複合材料強度，使用萬能材料試驗機（Cometech QC-508M2F, 台灣）進行拉伸測試與衝擊強度測試。拉伸測試依據 ASTM D638 Type IV，採 50 mm/min 速率進行。衝擊測試依據 ASTM D412，使用 Ceast 擺錘衝擊試驗機（Model Resil 50B）與切缺機進行，採 Izod 衝擊方式，使用 2.75 J 之錘頭。每組樣品進行了至少五次的重複測試，記錄了其平均值與標準差。

2-3-5 掃描式電子顯微鏡（Scanning electron microscope, SEM）

使用掃描式電子顯微鏡（SEM, TESCAN VEGA 3 SBH）觀察本實驗之複合材料表面形貌與 nHA 分散情形。操作電壓為 20 kV，放大倍率為 3000 倍。所有樣品先經真空乾燥並鍍金處理。樣品之元素分析則透過搭載 SEM 的能譜儀（EDX, Nova NanoSEM 230）進行。對於發泡實驗方面，本實驗使用之掃描式電子顯微鏡型號為 Nova NanoSEM 230，放大倍率可高至 10,000 倍。

2-3-6 穿透式電子顯微鏡觀察（Transmission electron microscope, TEM）

為分析 nHA 在 PLA/PBS/PBAT/nHA 複合材料中，各物質的分佈情形，本實驗用採用穿透式電子顯微鏡（TEM, Hitachi H-7650）進行觀察。超薄切片樣品於 −100 °C、氮氣環境中以低溫超薄切片機與鑽石刀製備，並放置於銅網上，以 70 kV 低電壓觀察以減少電子束損壞。

2-3-7 熱重分析（Thermo-gravimetric analysis, TGA）

本實驗使用熱重分析儀（TGA, Pyris 6, Perkin Elmer）評估樣品熱穩定性。取約 8 mg 樣品，於氮氣環境中以 10 °C/min 速率由 40 升溫至 600 °C，並記錄 TGA 熱重曲線與 DTGA 結果。

doi:10.6342/NTU202502722

2-3-8 吸水率測試

本研究亦探討聚合物複合材料之吸水性質。實驗之樣品尺寸為 20 mm × 10 mm × 2 mm，於 50 °C 真空烘箱乾燥 48 小時後秤重（使用精度 0.01 mg 之電子天平）。樣品完全浸泡於 25 °C 蒸餾水中，採用之浸泡時間，訂為第 1、2、5 與 8 天。每次浸泡後用濾紙擦拭表面水分再行秤重，依據重量差計算吸水率。

2-4 飽和與發泡步驟

為了使本實驗之聚合物複合材料能產生多孔隙結構，本研究進行了超臨界二氧化碳（SC-CO_2）之飽和與發泡程序，發泡程序的示意圖，表示於圖 2-2。在高壓（飽和壓力，P_s）與高溫（飽和溫度，T_s）條件下，SC-CO_2會藉由擴散行為，溶進入聚合物複材中，並持續一段飽和時間（t_s）。隨後進入發泡階段，操作條件包括中間變化的發泡溫度（T_f）、發泡壓力（P_f）與發泡時間（t_f），最終經由快速減壓至常壓，形成多孔發泡結構。 本研究中 PLA/PBS/PBAT/nHA 樣品之發泡操作參數的示意圖，列於第三章結果與討論之中。

樣品置於高壓容器中（Applied Separations 70770, Allentown, PA, USA），此壓力艙安裝於自製之電熱加熱裝置內，具可開蓋結構及溫控系統。本研究中溫度不確定度為±2 °C。為排除艙內空氣，系統首先以低壓 CO_2通氣 5 分鐘。接著使用電熱裝置將高壓艙內加熱至所設定之溫度，並以 ISCO 260D 高壓幫浦（Teledyne Technologies, Lincoln, NE, USA）加壓至操作壓力。本研究特別著重探討不同飽和與發泡策略對於 PLA/PBS/PBAT/nHA 複合材料之影響。各種發泡條件下的壓力、溫度等參數，詳列於後續之結果與討論章節。

doi:10.6342/NTU202502722

2-5 發泡高分子複合材料之結構與特性分析

本研究以掃描式電子顯微鏡（SEM, Nova NanoSEM 230, Hillsboro, OR, USA）觀察發泡高分子複合材料之斷面微型結構。在 SEM 觀察前，所有發泡樣品皆經真空乾燥並鍍上一層金膜以提高導電性。發泡樣品之膨脹倍率（φ）係依據下式 (1) 計算[35,56]：

$$\varphi = \frac{\rho_s}{\rho_f} \tag{1}$$

其中，ρ_s 為固體（未發泡）樣品之密度，ρ_f 為發泡樣品之密度。密度量測採用水置換法，依據 ASTM D792 標準[64,65]。

單位體積泡孔數（cell density, N_0，單位：cells/cm³）則依下式 (2) 計算[36,53,54]：

$$N_0 = \frac{6[1 - (\rho_f / \rho_s)]}{\pi D^3} \times 10^{12} \tag{2}$$

其中，D 為泡孔的平均直徑（μm），由 SEM 影像量測得之。

發泡樣品的孔隙率（porosity, ε）可由膨脹倍率計算得出，公式如下[36,54]：

$$\varepsilon = \frac{\varphi - 1}{\varphi} \tag{3}$$

對於臨床組織工程而言，開孔率（opening cell content, OCC）是重要的結構特性。OCC 由發泡樣品中開孔體積（V_{open}）與總體積（V_{total}）之比值表示，如下式 (4) 所示[56]：

doi:10.6342/NTU202502722

$$\mathrm{OCC} = \frac{V_{open}}{V_{total}} = 1 - \frac{V_{true}}{V_{total}} \quad (4)$$

其中，V_{true} 為樣品的真體積（包括閉孔體積與泡壁體積），而開孔體積則為 V_{true} 減去 V_{total}。V_{true} 的測定係以氮氣比重瓶（nitrogen pycnometer, AccuPyc II 1340, Micrometric, Norcross, GA, USA）完成。

2-6 接觸角與壓縮機械性質測試

本研究之複合材料，使用接觸角分析儀（SEO Phoenix, S.E.O. Co. Ltd., Ansung City, Republic of Korea）測量各種發泡結果之水接觸角。紀錄初始接觸角並持續觀察其在 30 分鐘內的變化情形。另使用動態機械分析儀（DMA, Perkin Elmer 7e, Waltham, MA, USA）進行壓縮應力–應變特性測試。樣品承受的壓力範圍為 7 kPa 至 1.13 MPa，負載速率固定為 10 kPa/min。文獻中亦有類似本實驗之多孔 PDLLA/生物玻璃複合材料進行的 DMA 測試報告可供參考[66]。

doi:10.6342/NTU202502722

第三章 實驗結果與討論

3-1 PLA/PBS/PBAT 複合材料之拉伸強度測試結果

本研究所使用之 PLA 為基材的高分子複合材料配方列於 Table 2-2 中。試樣編號 PLA60 代表一種未添加奈米羥基磷灰石（nHA）的聚合物複合材料，其組成為 60 wt% PLA、25 wt% PBS 與 15 wt% PBAT。Table 2-2 中的樣品系列 A 與 B 分別為含有不同添加量 nHA 的試樣。以樣品 A0 為例，其為含 70 wt% PLA、20 wt% PBS、10 wt% PBAT 的三元聚合物複合材料，未添加 nHA；而 A3、A5 與 A7 則為在與 A0 相同基材組成下，分別添加 3、5 及 7 wt% nHA 所製成之樣品。

樣品系列 B 為另一組 PLA 為基礎的三元聚合物複合系統，配方為 80 wt% PLA、15 wt% PBS 與 5 wt% PBAT。B0、B3、B5 與 B7 則分別對應添加 0、3、5 及 7 wt% nHA 之試樣。已有文獻指出，含有 nHA 之奈米複合材料有助於提升其在骨生成應用中的生物相容性。

為篩選出具可接受機械性質之配方，本研究首先對未添加奈米羥基磷灰石（nHA）之聚合物複合材料進行拉伸強度測試。這些不含 nHA 的聚合物複合材料之拉伸強度結果列於 Table 3-1 中。由表中可觀察到，PLA60 試樣之最大拉伸應力（拉伸強度）為 37.6 ± 1.8 MPa，而試樣 A0 與 B0 的最大拉伸應力皆超過 45 MPa。

儘管人體皮質骨與鬆質骨的拉伸強度會隨年齡變化，其範圍分別約為 50–150 MPa 與 10–100 MPa[13,67,68]。根據文獻報導，若聚合物材料的拉伸強度高於 40 MPa，即可滿足骨組織工程的應用需求[48]。由 Table 3-1 可見，試樣 A0 與 B0 的拉伸強度已接近人體皮質骨拉伸強度的下限。

此外，這些試樣在最大拉伸應力時的延伸率約為 8%。其拉伸模數也優於人體

doi:10.6342/NTU202502722

鬆質骨[11]。因此，本研究製備之含 70 wt% 或 80 wt% PLA 的高分子複合材料，具備良好的機械強度與生物相容潛力，可視為骨移植用途之可接受生醫材料。

3-2 PLA/PBS/PBAT/nHA 複合材料之 FTIR 量測結果

本研究使用傅立葉轉換紅外光譜儀（FTIR）分析各種 PLA/PBS/PBAT/nHA 複合材料的化學結構，其量測結果如 Figure 3-1 所示。約 3000 cm^{-1} 處的吸收峰對應於 PLA 中 $–CH_3$ 基的對稱與不對稱伸縮振動。位於 1750 cm^{-1} 的特徵峰則來自 PLA，以及 PBS 與 PBAT 中的酯基 (C=O) 伸縮振動。1181 cm^{-1} 與 1082 cm^{-1} 處的吸收峰分別為酯鍵中 C–O–C 結構的特徵振動。1040 cm^{-1} 處的吸收峰可歸因於 $C–CH_3$ 結構的存在[48,69-72]。在加入 nHA 的樣品中，於 602 cm^{-1} 與 570 cm^{-1} 處觀察到清晰的吸收峰，這些為 nHA 中 PO_4^{3-} 官能基的特徵峰[48,70,72]。

值得注意的是，在未添加 nHA 的試樣 A0 與 B0 中，並未觀察到 PO_4^{3-} 的吸收峰。而 Figure 3-1 (a) 與 Figure 3-1 (b) 中其他含 nHA 試樣的 FTIR 光譜則清楚顯示出該些特徵峰，證實了 nHA 成分已成功摻入聚合物複合材料之中。

3-3 PLA/PBS/PBAT/nHA 複合材料之 XRD 量測結果

為進一步確認 PLA/PBS/PBAT/nHA 複合材料中是否成功摻入 nHA，並鑑別聚合物複合材料中的結晶物種，本研究進行了 X 射線繞射分析（XRD）。樣品系列 A 與 B 的 XRD 結果分別如 Figure 3-2 (a) 與 Figure 3-2 (b) 所示，顯示不同添加量的 nHA 對繞射圖譜的影響。

在 2θ 為 15° 至 20° 區間可觀察到 PLA 的特徵繞射峰，PBS 則於 2θ = 22.5° 處出現其特徵繞射峰。nHA 的特徵繞射峰則出現在 25.9°、28° 及 32–35° 等位置[48][71][72]。

doi:10.6342/NTU202502722

在未添加 nHA 的樣品 A0 與 B0 中，並未觀察到任何 nHA 的繞射峰。相對地，從樣品 A3 至 A7 與 B3 至 B7 的 XRD 圖譜中可以清楚看出，隨著 nHA 含量的增加，其對應的繞射峰強度也隨之提升，顯示 nHA 成分已成功摻入並在聚合物基材中以結晶形式存在。

3-4 PLA/PBS/PBAT/nHA 複合材料之 DSC 與結晶分析結果

本研究利用示差掃描量熱分析（DSC）以評估半結晶聚合物的熱歷程與結晶行為。樣品系列 A 與 B 添加不同含量 nHA 的第二次加熱曲線分別如 Figure 3-3 (a) 與 Figure 3-3 (b) 所示。從 DSC 熱圖譜中可獲得 PLA 的玻璃轉移溫度（$T_{g,PLA}$）、冷結晶溫度（T_{cc}）、PLA 的熔融溫度（$T_{m,PLA}$）、冷結晶焓變（ΔH_{cc}），以及複合材料之熔融焓變（ΔH_m），其數據列於 Table 3-2。

nHA 的添加顯著影響 PLA/PBS/PBAT 複合材料的結晶行為，進而影響其物理性質。本研究計算不同配方複合材料的相對結晶度（X_c），公式如下[48,73]：

$$X_c = \frac{\Delta H_m - \Delta H_{cc}}{\omega_{PLA}\Delta H_{o,PLA} + \omega_{PBS}\Delta H_{0,\,PBS} + \omega_{PBAT}\Delta H_{0,PBAT}} \times 100\% \qquad (1)$$

其中，ω_{PLA}、ω_{PBS} 及 ω_{PBAT} 分別為複合材料中 PLA、PBS 與 PBAT 的重量分率；$\Delta H_{o,PLA}$、$\Delta H_{o,PBS}$ 和 $\Delta H_{o,PBAT}$ 分別為 100% 結晶態的熔融焓變。文獻中報導的理論熔融焓變值分別為 PLA 為 93.1 J g^{-1}，PBS 為 200 J g^{-1}，PBAT 為 114 J g^{-1}[48,73-76]。

如文獻所述，PLA 與 PBS 或 PLA 與 PBAT 之間的熱力學相容性較差[33,73,77-79]。為了促進結晶過程中的晶核成長，常使用奈米粒子作為成核劑[77-80]。根據 Table 3-2 所示，PLA/PBS/PBAT 複合材料（樣品 A0）之相對結晶度 X_c 為

doi:10.6342/NTU202502722

20.1%。當加入不同含量的奈米羥基磷灰石（nHA）後（樣品 A3、A5 和 A7），其相對結晶度 X_c 分別上升至 24.8% 至 27.0%。聚合物複合材料結晶度的提升有助於其機械性質的改善。

由 Table 3-2 亦可觀察到，樣品系列 B（樣品 B0、B3、B5 與 B7）在加入 nHA 後，其相對結晶度 Xc 亦呈現出隨添加量增加而略為上升的趨勢。

3-5 PLA/PBS/PBAT/nHA 複合材料之非等溫結晶行為

根據先前文獻，已探討使用 DSC 表徵非等溫結晶聚合物奈米複合材料中異質成核的影響[81,82]。本研究所製備樣品在由 200 °C 冷卻至 50 °C 的過程中，於不同冷卻速率（2.5、5、7.5 與 10 °C/min）下之熱流曲線如 Figure 3-4 所示。從冷卻曲線中可觀察到，樣品 A0 並無明顯結晶峰出現，顯示其熔融結晶能力較差。

當樣品中 nHA 含量由 0 增加至 3 wt% 時，在冷卻速率為 2.5 °C/min 下開始出現結晶行為，其放熱峰對應的焓變值 ΔH_{hc} 自 0 增加至 7.8 J/g。此現象可歸因於添加的 nHA 在材料中扮演成核劑角色，誘導異質成核行為。隨著 nHA 含量進一步上升，ΔH_{hc} 值略為增加。

相較之下，樣品 B0（未添加 nHA）即顯示出較高之熔融結晶能力，在 2.5 °C/min 冷卻速率下，其 ΔH_{hc} 值達 10.1 J/g。然在 B3、B5 與 B7 等樣品中，所觀察之 ΔH_{hc} 值變化不大，顯示於該組合物系統中，添加 nHA 對其結晶行為未造成明顯影響。

所有非等溫 DSC 的量測數據均列於 Table 3-3 中。樣品系列 A 與 B 呈現出不同的趨勢，可能源於其組成中 PLA 基礎結晶能力的差異。樣品 A0 中 PLA 含量較低，導致其在冷卻過程中熔融結晶能力有限。當添加 nHA 時，產生成核效應，

doi:10.6342/NTU202502722

使晶體形成變得相對容易。因此，隨著 nHA 含量的增加，其 ΔH_{hc} 值顯著上升。

相對地，樣品 B0 中 PLA 含量較高，本身即具備較佳的結晶優勢。在此情況下，即使添加 nHA，其對於結晶行為的促進效果不如系列 A 顯著，與未添加 nHA 的 B0 樣品相比，其結晶程度改善幅度有限。

3-6 PLA/PBS/PBAT/nHA 複合材料之拉伸與衝擊強度測試結果

本研究進行了拉伸與衝擊強度測試，以探討各種聚合物複合材料的機械性質。樣品系列 A 與 B 添加不同含量 nHA 的典型拉伸應力測試結果以圖形方式呈現在 Figure 3-5 中。重複測試所獲得的最大拉伸應力（拉伸強度）、最大拉伸應變、拉伸模數以及衝擊強度等數據列於 Table 3-4。

觀察發現，PLA 含量為 80 wt% 的樣品系列 B 其拉伸強度可達 57.9 ± 1.0 MPa，而 PLA 含量為 70 wt% 的樣品系列 A，其拉伸強度約為 47 至 50 MPa。樣品系列 A 與 B 的最大拉伸應變皆介於 7 至 8% 之間，優於純 PLA（6%，如 Table 2-1 所示）與人體骨骼（皮質骨 1–3%、鬆質骨 3–7%）[11]。樣品系列 A 含不同 nHA 含量的拉伸模數介於 642 至 905 MPa，而系列 B 則可達 1.0 GPa。

隨著 nHA 添加量增加，拉伸強度與拉伸模數也隨之提升，於添加 5 wt% nHA（樣品 A5 與 B5）時達到最高值。然而，當 nHA 含量提高至 7 wt%（樣品 A7 與 B7）時，拉伸強度略有下降，顯示存在最佳 nHA 添加量之可能。

衝擊強度測試則顯示聚合物複合材料的韌性。純 PLA 的衝擊強度約為 2.5 kJ m^{-2} [30]。將 PLA 與具延展性的 PBS 與 PBAT 複合後，所有樣品的韌性皆有所提升。由 Table 3-4 可見，在同一系列樣品中，添加不同量 nHA 對衝擊強度的影響並不顯著。

doi:10.6342/NTU202502722

Figure 3-5 (a)及(b) 分別比較了樣品系列 A 與 B 在不同 nHA 含量下的最大拉伸強度、最大拉伸應變與衝擊強度。由這些比較結果可推論，樣品 B3 或 B5 為具有良好機械強度的潛力骨移植材料配方。本研究的機械性質測試結果推論，nHA 奈米粒子在聚合物複合材料的結晶過程中扮演成核劑的角色，有助於提升材料的結晶度與拉伸強度。

3-7 PLA/PBS/PBAT/nHA 複合材料之 SEM 分析結果

斷面掃描式電子顯微鏡（SEM）分析已廣泛應用於探討聚合物複合材料的形貌與添加劑在聚合物基材中的分佈情形[83-85]。聚合物複合材料由延展性向脆性轉變的過程，以及形貌與機械性質之間的關聯，皆可透過 SEM 觀察進行分析。本研究中樣品系列 A 與 B 的衝擊斷面 SEM 影像如 Figure 3-6 與 Figure 3-7 所示。

Figure 3-6 (a) 為含有 70 wt% PLA、未添加 nHA 的 PLA/PBS/PBAT 複合材料之 SEM 影像。Figure 3-6 (b) 至 Figure 3-6 (d) 則為添加 3 至 7 wt% nHA、仍含 70 wt% PLA 之聚合物複合材料的 SEM 影像。由 Figure 3-6 (a) 可見，未添加 nHA 的 PLA/PBS/PBAT 複合材料呈現相對粗糙且具延展性的斷裂面。

當添加 3 wt% nHA（樣品 A3）時，如 Figure 3-6 (b) 所示，可觀察到分散良好的 nHA 顆粒，呈現為斷面上的細小白點。隨著 nHA 含量的增加，SEM 影像中可見更多 nHA 顆粒分佈，如 Figure 3-6 (b) 至 Figure 3-6 (d) 所示。由於 nHA 添加量較高，Figure 3-6 (c) 與 Figure 3-6 (d) 顯示斷面上出現裂紋，並呈現出較脆的斷裂形貌。

觀察結果顯示，斷裂面形貌由相對粗糙且具延展性，逐漸轉變為較硬且脆性的結構。此一形貌變化趨勢亦與下一節 TEM 結果一致，證實奈米顆粒於基材中分佈均勻。此外，nHA 添加對拉伸與衝擊強度之影響亦與 SEM 結果相符，顯示隨

doi:10.6342/NTU202502722

著 nHA 添加量增加，聚合物複合材料變得更堅硬且具脆性，同時拉伸強度亦呈現上升趨勢。

Figure 3-7 顯示了含有 80 wt% PLA 的 PLA/PBS/PBAT/nHA 複合材料的類似 SEM 影像。其衝擊斷裂面形貌與 Figure 3-6 一致。Figure 3-7 (a) 中未檢測到 nHA 顆粒，斷面呈現相對粗糙的表面。當向聚合物複合體中添加 nHA 顆粒時，如 Figure 3-7 (b) 至 Figure 3-7 (d) 所示，斷面呈現尖銳的斷裂形貌。隨著 nHA 添加量的增加，Figure 3-7 中的 nHA 影像變得更加明顯。nHA 顆粒在聚合物基體中分散均勻，但在較高添加量時會出現聚集現象。隨著 nHA 添加量增加，斷裂形貌再次呈現出堅硬且脆性的特徵。

為確認 SEM 影像中奈米顆粒的化學成分，Figure 3-8 顯示了典型複合樣品 B7 的能量散射 X 射線（EDX）譜圖。圖中 Ca 與 P 元素的特徵峰明確證實了樣品中存在 nHA 顆粒。

3-8 PLA/PBS/PBAT/nHA 複合材料的 TEM 測量結果

Figure 3-9 顯示了樣品系列 A 在 20,000 倍放大倍率下的 TEM 影像。對於未添加 nHA 的樣品 A0，未檢測到任何 nHA 顆粒影像。此外，Figure 3-9 (a) 中觀察到複合體的相分離形貌，連續相（或較亮的區域）為主要成分 PLA 基體，而較暗的區域為分散相 PBS/PBAT。添加 3 wt% nHA 後，Figure 3-9 (b) 顯示出小黑點狀的 nHA 顆粒，粒徑約在 70 至 100 nm 範圍內；同時，PBS/PBAT 分散相尺寸變小，顯示 nHA 顆粒的添加有助於在雙螺桿混合過程中促進聚合物相的分散。隨著 nHA 添加量由 5 wt% 增加至 7 wt%，聚合物相的均勻分散程度進一步提高，PBS/PBAT 分散相變得更小，分別見 Figure 3-9 (c) 與 Figure 3-9 (d)。不過需注意的是，當 nHA 添加量較高時，nHA 顆粒會因聚集而變大，7 wt% 添加量時，在

doi:10.6342/NTU202502722

Figure 3-9 (d) 中可見接近微米尺寸的 nHA 顆粒。樣品系列 B 的 TEM 結果類似，見 Figure 3-10。樣品 B0（無添加 nHA）中未見 nHA 顆粒影像（Figure 1-13 (a) ）。當 nHA 添加量從 3 wt% 增至 7 wt% 時（Figure 3-10 (b) 至 Figure 3-10 (d) ），黑色細點狀 nHA 顆粒數量增加。TEM 影像也顯示出 nHA 對形貌的細化作用，表明 nHA 有助於聚合物域的分散。

3-9 PLA/PBS/PBAT/nHA 複合材料的熱重分析 (TGA)

本研究利用熱重分析（TGA）檢測不同配方聚合物複合材料的熱穩定性。樣品系列 A 與 B 的 TGA 與微分熱重分析（DTGA）熱譜分別如 Figure 3-11 和 Figure 3-12 所示。Table 3-5 列出所有樣品的 5% 與 50% 重量損失溫度（$T_{5\%}$ 與 $T_{50\%}$）、最大分解速率溫度（T_{max}），以及 600°C 時的殘留重量百分比（WR）。

對於樣品系列 A，Figure 3-11 (a) 中的 TGA 熱譜顯示各樣品（A0 至 A7）主要分解溫度介於 300 至 400°C 之間。Figure 3-11 (b) 的 DTGA 熱譜呈現出兩階段分解過程，其中第一個峰值對應於 PLA 的最大分解速率[67]。如 Figure 3-11 與 Table 3-5 所示，添加 nHA 對聚合物複合體的 T_{max} 影響不大。隨著熱穩定無機物 nHA 含量的增加，500 至 600°C 範圍內的殘留重量百分比亦明顯提高，如 Figure 3-11 (a) 與 Table 3-5 所示。樣品系列 B 的 TGA 與 DTGA 熱譜如 Figure 3-12 所示，主要分解溫度範圍亦為 300 至 400°C。樣品系列 B 的四個樣品殘留重量百分比的增加同樣與 nHA 添加量的增加一致。綜合 TGA 結果，本研究所製備的聚合物複合材料均展現出良好的熱穩定性，適合作為骨移植材料應用。

3-10 PLA/PBS/PBAT/nHA 複合材料的水吸收測試結果

水吸收百分比（WA）透過下式計算：

doi:10.6342/NTU202502722

$$WA(\%) = \frac{W_t - W_d}{W_d} \times 100\% \quad (2)$$

式中，W_d 為樣品乾燥後的重量（在 50°C 下乾燥 2 天，於水吸收測試前），W_t 為樣品浸泡於蒸餾水中 t 天後的重量。

Figure 3-13 顯示所有樣品浸泡於蒸餾水 24 小時後的水吸收結果。對於樣品系列 A，由於 nHA 具有親水性，隨著 nHA 添加量增加，水吸收率呈現上升趨勢。樣品系列 B 亦表現出類似的水吸收趨勢。與系列 A 相比，因為系列 B 含有較高比例的 PLA，其水吸收率較低。在 24 小時測試中，樣品 B5 與 B7 的水吸收率比 B0 約提升了 15%。Figure 3-14 顯示所有樣品在較長時間浸泡後的水吸收結果。結果顯示，浸泡 5 天後，各樣品的水吸收程度比第一天增加約 40% 至 50%；浸泡 8 天後，水吸收程度比一天時約提升 70% 至 80%。此水吸收率的提升與文獻中 PLA 複合材料的相關報告一致[86,87]。水吸收結果表明，親水性 nHA 的加入提高了水吸收速率，有利於該聚合物複合材料在骨組織工程中的應用。

3-11 使用 (1T-1P)、(2T-1P) 及 (2T-2P) 操作策略之發泡結果

在發泡製備過程中，選擇適當的操作條件對於 PLA 基可生物降解聚合物混合物的發泡形成具有重要影響。過去大量文獻探討了含 PLA 聚合物系統的發泡溫度與壓力範圍，並提出了所謂的「發泡操作窗口」(foaming window)[52-54]。Sarver 和 Kiran 等研究者在近期的綜述中對此發泡窗口做了詳細說明[27]，指出操作溫度範圍約為 100 至 160°C，操作壓力範圍為 100 至 200 bar。本研究所稱之「單步發泡策略」(1T-1P)，係指在飽和溫度 T_s 與飽和壓力 P_s 下，利用超臨界二氧化碳（SC-CO_2）對聚合物混合物進行飽和吸附，然後快速減壓至環境條件完成發泡形成的過程。

doi:10.6342/NTU202502722

在組織工程材料研究中，有關發泡孔徑呈雙峰分佈（同時具有大孔與小孔）之討論在近期研究已被提出[88,89]，且針對不同聚合物系統的研究仍在進行中。文獻指出，要獲得雙峰發泡結構，必須採用兩階段操作，透過改變溫度或壓力實現[36,55,59,60,90,91]。其中，兩階段溫度操作最為普遍，因為溫度會顯著影響聚合物結晶及熔體強度。具體作法為：先將聚合物加熱至較高的飽和溫度 T_s 和壓力 P_s，並保持飽和一定時間 t_s，讓 SC-CO_2 吸附於聚合物中；接著降低至中間或發泡形成溫度 T_f 並保持一定時間 t_f，再迅速減壓至環境壓力完成發泡。此種操作策略在本研究中稱為 (2T-1P)。若在發泡形成時間 t_f 內，壓力先由飽和壓力 P_s 快速降至中間壓力 P_f（發泡壓力），再迅速降至環境壓力，此操作策略則稱為 (2T-2P)。

參考文獻中以 PLA/PBS (80/20 wt%) 為例[36]，飽和溫度 T_s 設定為 150°C。值得注意的是，當飽和溫度高於 160°C 時，PLA 熔體強度不足以抵抗吸附過程中之內部壓力[54]，故本研究選擇 150°C 作為 T_s。根據過去文獻測得的 SC-CO_2 在生物降解聚合物中的溶解度資料[65,92,93]，飽和時間 t_s 設為 90 分鐘，以確保 CO_2 吸附接近平衡，此時間與先前研究中採用之數值相符[40,53,54,64,94]。本研究首先採用 (1T-1P) 單步發泡策略，在 150°C 飽和溫度下，分別以 130、150 和 170 bar 進行發泡。結果顯示在 150 bar 飽和壓力下獲得最高膨脹倍率，因此本研究以此壓力為主。

Figure 3-15 展示三種發泡策略的操作條件與對應的 SEM 影像：（A）單步 (1T-1P)；（B）兩溫度層級 (2T-1P)，中間冷卻至 110°C，保持時間 10 分鐘；（C）兩溫度及兩壓力層級 (2T-2P)，中間溫度同為 110°C，且中途快速降壓由 150 bar 至 100 bar。中間壓力 100 bar 依據文獻發泡窗口選擇[27]，中間溫度 110°C 約為發泡窗口中間溫度[53,54]，發泡保持時間 t_f 設為 10 分鐘，於 (2T-1P) 與 (2T-2P) 策略中均適用。

doi:10.6342/NTU202502722

從 (1T-1P) 發泡策略 A 的 SEM 觀察可見，發泡產品中分布著稀疏的小孔，而樣品仍有很大部分未發泡。此結果表示，在 (1T-1P) 發泡過程中，僅有少量吸附的 CO_2 在快速減壓時產生了成核，形成小氣泡，大部分區域未形成發泡結構。(1T-1P) 策略的特點是等溫操作，即聚合物混合物在單一高溫下吸附 CO_2，隨後透過突然降壓至環境壓力啟動發泡。然而，因缺乏第二個溫度區域調節熔體強度及發泡能力，PLA/PBS/PBAT/nHA 混合物無法形成大型或雙峰泡孔結構。此限制對於聚合物混合物尤為重要，因為實現良好孔隙結構需仔細控制溫度與壓力條件。缺乏第二階段溫度調控導致熔體強度不足以支撐穩定氣泡成長，使得發泡結構僅形成平均尺寸約 27.6 μm 的小孔。

(2T-1P) 發泡策略 B 如 Figure 3-15 所示，增加了由 150°C 降至 110°C 的冷卻，並在 110°C 保持 10 分鐘。在冷卻及保持階段，氣泡開始成核並形成單峰泡孔結構。透過策略 B 的 SEM 影像未見大型泡孔，可能是因為成核能障礙在保持時間內尚未克服，僅在最後快速降壓階段發生短暫成核及小孔形成[95,96]。策略 B 產生的平均孔徑約為 34.2 μm。為了獲得適用於組織工程的小孔與大孔雙峰結構，進一步考慮兩階段壓力操作。

(2T-2P) 發泡策略 C 如 Figure 3-15 所示，在由 150°C 降至 110°C 且保持 10 分鐘的同時，壓力由 150 bar 快速降至 100 bar，並保持中間壓力 10 分鐘後，再迅速降至環境壓力。此策略主要產生平均尺寸達 408.7 μm 的大孔，且泡孔密度較低。策略 C 所產生的孔徑及結構與策略 B 完全不同，主要差異在於中間快速降壓（由 150 至 100 bar）。根據經典成核理論[61,97]，成核自由能障礙與壓力過飽和的平方成反比，壓力過飽和定義為臨界氣泡壓力與操作壓力之差。當操作壓力迅速下降 50 bar 時，可能在中間快速減壓階段誘發過多成核，並於保持階段促成氣泡高度成長，導致最終快速降壓時幾乎無小孔形成。SEM 影像顯示大孔結構，暗示氣泡過度膨脹且可能合併。此結果表明，透過兩階段降壓操作可獲得較大孔徑的泡

doi:10.6342/NTU202502722

孔，但中間降壓幅度及保持時間須調整，以實現理想雙峰泡孔結構。

Figure 3-16 繪製三種發泡策略 A、B、C 的孔徑分布相對頻率，顯示三者均呈現單峰泡孔結構。本研究觀察到 (1T-1P) 策略 A 膨脹倍率較低 (1.36)，孔徑亦較小；(2T-1P) 策略 B 膨脹倍率提升至 2.72，孔徑仍屬小型；(2T-2P) 策略 C 透過中間階段溫度及壓力變化，產生幾乎全為大型泡孔，膨脹倍率達 5.41。中間壓力變化有助於產生較大孔徑，但為獲得理想雙峰孔結構，可能需要採用漸進式壓力變化。

3-12 使用 (2T-2P，階梯式 ΔP) 操作條件之發泡結果：壓力效應

基於上述三種發泡策略，進一步探討了伴隨階梯式壓力下降的溫度變化過程（2T-2P，階梯式 ΔP）。Figure 3-17 顯示了 (2T-2P，階梯式 ΔP) 發泡策略的示意圖。飽和壓力與溫度分別維持在 150 bar 與 150 °C，飽和時間為 90 分鐘，以確保 CO_2 充分吸附於聚合物混合物中。飽和階段結束後，操作溫度下降至中間值（T_f，或稱發泡溫度），並保持該溫度達保持時間（t_f）。在此保持時間內，操作壓力由 150 bar 逐步降低至中間壓力值（P_f，或稱發泡壓力），每一步降壓速率為 10 bar/min。透過此漸進式壓力變化，有望獲得雙峰泡孔結構的多孔產品，其中大孔在中間保持階段形成，小孔則在最終快速降壓階段產生[36,59-61]。

首先，我們研究了發泡壓力（P_f）的影響，發泡溫度（T_f）維持在 110 °C。針對不同中間壓力效應，探討了三種（2T-2P，階梯式 ΔP）發泡策略：

(D) 階梯式壓力降至 120 bar，保持時間（t_f）3 分鐘，

(E) 階梯式壓力降至 100 bar，保持時間 5 分鐘，

(F) 階梯式壓力降至 80 bar，保持時間 7 分鐘。

doi:10.6342/NTU202502722

Figure 3-18 展示了三種發泡策略 D、E、F 所得到的 SEM 影像及細胞尺寸分布的相對頻率。可以觀察到，使用（2T-2P，階梯式 ΔP）發泡策略後，可獲得雙峰孔洞結構。整體而言，小孔的平均尺寸在三種發泡策略 D、E 與 F 中約為 110 至 160 μm。然而，大孔的平均尺寸則取決於壓力變化的程度。發泡溫度與壓力對孔洞尺寸與結構有重要影響。對於策略 D、E、F，其中間發泡溫度（T_f）固定為 110 °C，因此以下主要探討壓力變化幅度與發泡時間（t_f）的影響。

在相同中間溫度條件下，當發泡階段的中間壓力逐步降低時，SC-CO_2 在高分子材料中的溶解度降低，導致氣體逐漸從聚合物基體中釋放。當 CO_2 逸出時，形成過飽和狀態並誘發氣泡生成。壓力下降的幅度會影響氣泡的數量與尺寸。策略 D 的壓力下降幅度最小，產生的大孔平均尺寸也最小，約為 562 μm。此結果與經典成核理論一致：新相形成所需的自由能障礙與壓力過飽和度的平方成反比。氣泡核的生成與成長主要在逐步降壓過程中進行。發泡策略 D 中壓力從 150 bar 降至 120 bar（30 bar 的壓降）歷時僅 3 分鐘，對於氣泡成長的時間不足，導致所得大孔尺寸較策略 E 與 F 小。若需更大的孔洞尺寸，則應加大壓力降幅。

發泡策略 E 的結果顯示，當中間壓力降至 100 bar，並將發泡時間延長至 5 分鐘時，可產生更大的泡孔，平均大孔尺寸約為 602 μm。策略 F 則以 7 分鐘時間將壓力逐步降至 80 bar，所形成的大孔平均尺寸達到 775 μm。在策略 F 中，70 bar 的壓降可能使成核障礙顯著降低，促進了大孔的生成與成長。

從 Figure 3-18 所示之壓力效應可知，中間階梯式降壓策略有助於調控期望的孔洞尺寸與雙峰結構。根據組織工程不同應用的需求，可能需要不同的孔洞尺寸。例如，在骨組織工程支架中，雙峰泡孔結構具明顯優勢，而大至 800 μm 的孔洞亦可促進骨生成[98]。Figure 3-19 繪製了發泡策略 D、E、F 所得到的大孔平均尺寸，為選擇適當操作壓力條件以獲得理想雙峰孔結構提供參考依據。

doi:10.6342/NTU202502722

3-13 使用（2T-2P，階梯式 ΔP）操作條件之發泡結果：溫度效應

發泡溫度（T_f）之影響進一步也被加以探討，條件為將發泡壓力（P_f）由 150 bar 逐步降至 100 bar，如前節中所述之發泡策略 E。針對不同的中間或發泡溫度（T_f），設計了三組（2T-2P，階梯式 ΔP）發泡策略：

(G) T_f 設為 100 °C

(E) T_f 為 110 °C

(H) T_f 為 120 °C。

三組策略的發泡時間（t_f）均固定為 5 分鐘。Figure 3-20 顯示策略 G、E 與 H 之 SEM 圖像與對應的孔洞尺寸分布頻率。在相同的發泡壓力條件下，發泡溫度顯示出對超臨界 CO_2 在聚合物共混物中的溶解度與擴散性具有關鍵影響，同時也影響分子鏈的移動性與熔體強度，進而決定最終的孔洞結構[91,99]。

觀察結果顯示，三組發泡策略皆可產生雙峰孔洞結構，其小孔平均尺寸範圍為 105 至 164 μm。然而，各組策略所形成的大孔尺寸則隨發泡溫度不同而有顯著差異。三種操作溫度皆位於文獻報導的 PLA 發泡窗口內[52-54]，因此適用於本研究所使用之 PLA 基共混物。根據策略 G、E、H 的結果可看出，隨著發泡溫度由 100 °C 升高至 120 °C，平均大孔洞尺寸呈現遞減趨勢。這一趨勢可歸因於 SC-CO_2 在 PLA 基共混物中的溶解度變化及熔體強度的影響。

操作於 100 °C 發泡溫度的策略 G 所產生之平均大孔洞平均尺寸為 889 μm，為三組中最大。首先，此結果可由氣體溶解度解釋。在策略 G 中，從高飽和溫度降至低發泡溫度所產生的溫差較大，使得 SC-CO_2 密度提高，進而增加其於聚合物中的溶解度。在階梯式降壓過程中，較高的 SC-CO_2 含量造成較大的過飽和狀

doi:10.6342/NTU202502722

態，促進氣泡成核的生成與成長。除了氣體溶解度外，聚合物共混物的熔體強度亦發揮關鍵作用。根據文獻，足夠的熔體黏度有助於穩定氣泡成長[91]。在 100 °C 條件下，聚合物共混物具有較高的熔體強度，有利於氣泡膨脹，進而形成較大的平均大孔洞。因此，在策略 G 中，熔體強度與階梯式降壓的結合提供了有利的氣泡成長環境，使最終形成雙峰孔洞結構。

策略 E 與 H 的發泡溫度分別為 110 °C 與 120 °C，與高飽和溫度之溫差較小，因此 SC-CO_2 的密度與策略 G 相比略低，溶解度亦隨之下降，造成平均大孔洞尺寸的降低。此外，較高的發泡溫度亦降低了聚合物的熔體強度。在最終快速降壓與冷卻過程中，聚合物的熔體強度會再次上升。根據文獻，此種熔體強度的突然上升可能導致聚合物鏈回縮，使氣泡收縮並進一步降低最終平均大孔洞尺寸[53,100]。如 Figure 3-20 所示，策略 E 與 H 所得之平均大孔洞尺寸分別為 602 μm 與 476 μm。Figure 3-21 顯示了三種策略 G、E、H 所對應之平均大孔洞尺寸的遞減趨勢，清楚反映出發泡溫度對結構形成的影響。

3-14 各操作策略發泡結果之比較分析

本研究中所有發泡策略的實驗結果已彙總於 Table 3-6 。觀察結果顯示，發泡策略 A 與 B 僅產生小孔洞，其膨脹倍率相對較低（小於 3），且孔洞密度較高。這兩組策略的開孔率偏低，主要原因在於操作壓力下降速度過快，導致部分區域未充分發泡，並產生較多封閉型孔洞。

相較之下，應用發泡策略 C，亦即進行一次快速的中間壓力降低（50 bar），則可形成僅具大孔洞之結構，膨脹倍率顯著提升至 5.41。該策略下的開孔率亦提高至 67.8%，推測可能與氣泡成長過程中之氣泡融合現象有關。當氣泡尺寸變大時，彼此接觸或破裂形成通孔，進一步提升開孔率。

doi:10.6342/NTU202502722

其餘五種發泡策略皆成功製備出具雙峰孔洞分布（bimodal cell distribution）之結構，此特性對於組織工程與再生醫學應用具有顯著優勢。比較發泡策略 D、E 與 F 可發現，隨著中間壓力下降幅度增加，膨脹倍率由 4.3 提升至 14.0，平均大孔洞尺寸亦自 562 ± 29.4 μm 增加至 775 ± 13.0 μm，且開孔率由 60.2 ± 1.2% 提升至 77.8 ± 0.6%。孔洞尺寸的增大可能與發泡過程中氣泡膨脹與融合現象有關，導致形成相互連通之孔洞結構，進而提升整體開孔率。

另一方面，發泡策略 G 與 H 顯示平均大孔洞尺寸亦受中間發泡溫度影響。在本研究中，操作於 100 °C 之發泡策略 G 所獲得的最大平均大孔洞尺寸為 889.8 ± 66.2 μm，且達到最高開孔率 84.3 ± 0.4%。相較之下，策略 H 的操作溫度為 120 °C，其所得平均大孔洞尺寸僅為 476.4 ± 23.6 μm，開孔率亦較低，為 57.8 ± 1.2%。此結果顯示，較低的發泡溫度可提升溶解的超臨界 CO_2 含量與熔體強度，進而促進較大氣泡的穩定成長與連通孔結構的形成。

本研究各發泡策略所得之泡孔特徵，包括大、小孔洞尺寸、孔洞密度、膨脹倍率、孔隙率與開孔率，分別呈現在 Figure 3-22 (a) – (d) 中。研究結果證實，在發泡過程的中間階段施以階梯式壓力下降操作，可有效製備具有雙峰孔洞結構的高孔隙材料，其孔隙率範圍為 76.7% 至 94.4%，開孔率範圍為 57.8% 至 84.3%。此一結果顯示，本研究所製備之發泡高分子材料具備良好的結構特性，具潛力應用於組織工程支架（bioscaffold）領域[77,98,101]。

3-15 各操作策略發泡結果之親水性分析

水接觸角量測結果顯示，經不同發泡策略處理後所得之高分子發泡材料具有不同程度的親水性。如 Figure 3-23 所示，採用發泡策略 E 製備之樣品的代表性水接觸角結果中，初始接觸角為 68.5 ± 0.2°，經 30 分鐘後降至 50.7 ± 0.1°。相比之

doi:10.6342/NTU202502722

下，未發泡的 PLA/PBS/PBAT/nHA 共混材料其水接觸角為 87.5 ± 1.0°，接近疏水性。此結果顯示，透過策略 E 所獲得的雙峰孔洞結構顯著提升了材料的親水性。其他具有雙峰孔洞結構之發泡樣品亦表現出類似趨勢，歸因於大尺寸開孔結構的形成，有助於水分進入與擴散。Figure 3-23 採用發泡策略 E 製備之高分子發泡材料的水接觸角變化趨勢。

以下進一步探討本研究第 3-12 與第 3-13 節所述 (2T-2P, 階梯式 ΔP) 發泡策略製備之雙峰結構樣品在水接觸角隨時間變化的行為。所有這些樣品皆具雙峰孔洞結構，結果顯示，平均大孔尺寸較大的樣品展現出更低的水接觸角，亦即親水性更佳。如 Figure 3-24 (a) 所示，發泡策略 D、E、F 製備樣品之初始水接觸角分別為 76.0°、68.5° 與 54.4°。這是因為策略 F 所製得樣品具有較大的平均大孔尺寸與開孔率，進一步促進了水分的滲透與擴散。在 30 分鐘後，策略 F 所製樣品之水接觸角降至 27.4°，明顯低於策略 D 與 E 所製樣品（分別為 61.4° 與 50.7°）。

Figure 3-24 (b) 顯示策略 G、E 與 H 所製樣品的水接觸角變化亦呈現相似趨勢。這些趨勢進一步驗證，雙峰發泡結構中所形成的互連平均大宏孔（interconnected macrocells）有助於提升整體材料的親水性。

3-16 各操作策略發泡結果之動態機械分析（DMA）分析

Figure 3-25 顯示了採用第 3-12 與第 3-13 節所述之 (2T-2P, 階梯式 ΔP) 發泡策略製備之發泡樣品的動態機械分析（DMA）結果。所有測試樣品皆具有雙峰孔洞結構。Figure 3-25 (a) 為使用發泡策略 D、E 與 F 所製得樣品之壓縮應力–應變曲線。壓縮測試係透過動態機械分析儀（DMA 7e, Perkin Elmer, Waltham, MA, USA）進行，載荷以每分鐘 10 kPa 的速率逐漸施加，範圍由初始 7 kPa 增加至最大 1.13 MPa。

doi:10.6342/NTU202502722

結果顯示，相較於策略 D 與 E，策略 F 所製得之樣品在相同應力條件下具有更高的應變值，顯示其具備更佳的延展性。此趨勢與平均大孔尺寸的增加一致：策略 D 所製樣品在 5% 應變時的壓縮應力為 0.76 MPa，而策略 E 與 F 分別為 0.45 MPa 與 0.12 MPa。由此可知，平均大孔較小的樣品（策略 D）具有較高的剛性（stiffness），而平均大孔尺寸隨策略 E 至 F 增加後，樣品的韌性（toughness）亦隨之提升。

Figure 3-25 (b) 呈現策略 G、E 與 H 所製樣品的壓縮應力–應變行為，亦展現相似趨勢。策略 H 所製樣品，其平均大孔尺寸較小（476.4 ± 23.6 μm），表現出較高的剛性；而策略 G 所製樣品，其平均大孔尺寸最大（889.8 ± 66.2 μm），展現出明顯增強的韌性。這些結果說明，透過控制階梯式壓力下降與中間發泡溫度，可有效調控發泡材料的孔洞結構，進而影響其機械性能，滿足不同組織工程應用對材料強度與彈性的需求。

doi:10.6342/NTU202502722

第四章 結論

本研究成功開發並系統性評估了新型可生物降解的生物基聚合物複合材料，組成包括聚乳酸（PLA）、聚丁二酸丁二醇酯（PBS）、聚己二酸/對苯二甲酸丁二醇酯（PBAT）以及奈米級羥基磷灰石（nHA），並以超臨界二氧化碳（SC-CO_2）作為環保物理發泡劑，探討其結構、物理與機械性質及其應用潛力，作為組織工程與骨移植支架材料。本研究的主要發現與結論如下：

1. **機械強度與韌性特性：**

   實驗結果顯示，PLA 含量在 70～80 wt%，且摻入 3～5 wt% nHA 的聚合物複合系統具備良好的拉伸強度，範圍介於 47 至 57 MPa，符合骨移植替代材料的最低機械強度要求（一般建議為超過 40 MPa）。在兼顧剛性與延展性的設計目標下，本研究配方展現出良好的延伸率與衝擊強度，證明此材料系統具有潛力用於承受生理載荷的應用場合。此外，由於 PBAT 的引入，本系統克服了純 PLA 脆性高、斷裂伸長率低的缺點，進一步提高了材料整體的韌性與加工穩定性。

2. **熱性質穩定表現：**

   熱重分析（TGA）結果顯示，本研究各種複合配方的材料熱分解溫度大致落在 300～400°C 之間，表明其具備優異的熱穩定性，可滿足醫療材料在滅菌處理（如高壓蒸氣）或高溫加工過程中的需求。nHA 的存在並未顯著影響材料的熱穩定性，顯示其與聚合物基體具備良好相容性，適合進一步開發為可降解醫療植入物材料。

3. **親水性與吸水行為：**

   實驗顯示，隨著 nHA 含量增加，聚合物複合材料的水吸收能力明顯提升。在 24 小時浸水測試中，5 wt% nHA 添加組別的吸水率比無添加組增加約

doi:10.6342/NTU202502722

15%。這一現象與 nHA 表面羥基所帶來的高親水性密切相關，有助於細胞貼附、水分傳輸與養分交換。對於應用於骨組織工程的材料而言，適當的吸水性可以促進支架與宿主組織之間的整合，並可能提高新生骨組織的生成效率。

4. **發泡行為與微結構控制：**

利用 SC-CO_2 作為無毒且可再利用的物理發泡劑，本研究針對 PLA/PBS/PBAT/nHA 聚合物系統進行八種不同操作策略的發泡實驗，探討壓力、溫度與保壓時間對發泡結構之影響。研究發現，中間降壓與溫度控制是影響發泡品質與結構均勻度的關鍵因素。透過引入「階梯式壓力下降（stepwise ΔP）」的操作策略，在最終快速減壓前，進行中間壓力調整可有效控制氣泡成核與成長速率，進而獲得具有雙峰孔洞（bimodal cell structure）之結構特性。由本研究所獲得發泡材料的微結構顯示，小孔徑範圍介於 105～160 μm，大孔徑範圍則為 476～889 μm。在中間壓差增加的情況下，因氣體成核能障降低，氣泡數量與尺寸均增加，導致大孔徑明顯放大。而中間發泡溫度提升則造成 CO_2 溶解度下降，減少氣體儲存量，同時聚合物於最終減壓階段產生鏈段回縮效應，使得泡孔尺寸減小。因此，本研究驗證溫度與壓力雙參數調控策略在製備雙峰發泡結構方面的可行性。

5. **開孔率與孔隙率表現：**

所有採用階梯式發泡策略製備之材料皆形成具有互連結構的雙峰孔洞，總孔隙率範圍為 76.7%～94.4%，開孔率則為 60%～84%。此類高開孔結構有利於細胞的遷移、生長與營養滲透，是骨組織工程支架設計的理想條件。圖像分析與 SEM 觀察亦進一步證實了泡孔的連通性與空間穩定性。

6. **水接觸角與表面濕潤性：**

doi:10.6342/NTU202502722

水接觸角實驗顯示，所有發泡樣品皆展現明顯的親水行為，且接觸角隨時間逐漸下降。初始接觸角與最終接觸角的差值與宏孔尺寸呈反比關係，亦即大孔徑的發泡材料濕潤性較佳。以策略 F 所製備材料為例，其初始接觸角為 54.4°，經過 30 分鐘降至 27.4°，顯示材料表面具高度濕潤性。此結果進一步支持開孔率與平均大孔尺寸對材料親水性的正面貢獻，有助於體液進入與組織再生。

7. **動態壓縮力學性質：**

經 DMA 分析，平均大孔尺寸較小的發泡材料（如策略 D）展現較高剛性，其 5% 壓縮應變下的應力為 0.76 MPa，而平均大孔尺寸較大的樣品（如策略 F）於相同變形下僅為 0.12 MPa，呈現出良好的能量吸收與緩衝性能。這種剛性與韌性的變化趨勢對應於材料孔隙結構的差異，顯示可藉由發泡參數調控材料力學行為，達成特定應用需求。

綜合上述，本研究不僅成功設計出兼具力學強度、熱穩定性與親水特性的 PLA/PBS/PBAT/nHA 發泡材料，更透過精確的超臨界 CO_2 發泡策略，製備出具備雙峰泡孔結構、可調孔徑與高開孔率的支架材料。此類結構特性非常適合用於骨組織工程與再生醫學領域。未來研究建議可進一步針對細胞黏附、生物降解行為與體內生物相容性進行測試，以驗證其作為臨床骨移植支架材料的潛力與實用性。

doi:10.6342/NTU202502722

圖示

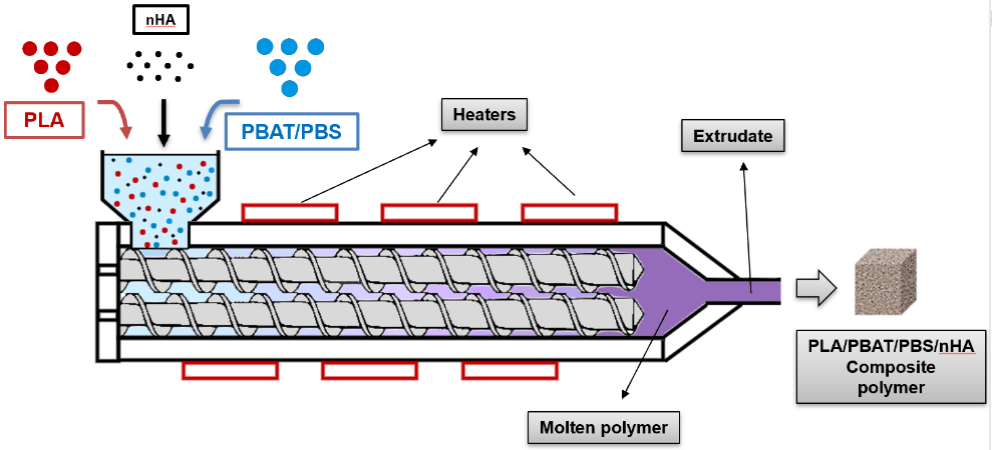

Figure 2-1. 本實驗所採用之雙螺桿擠出製程示意圖。

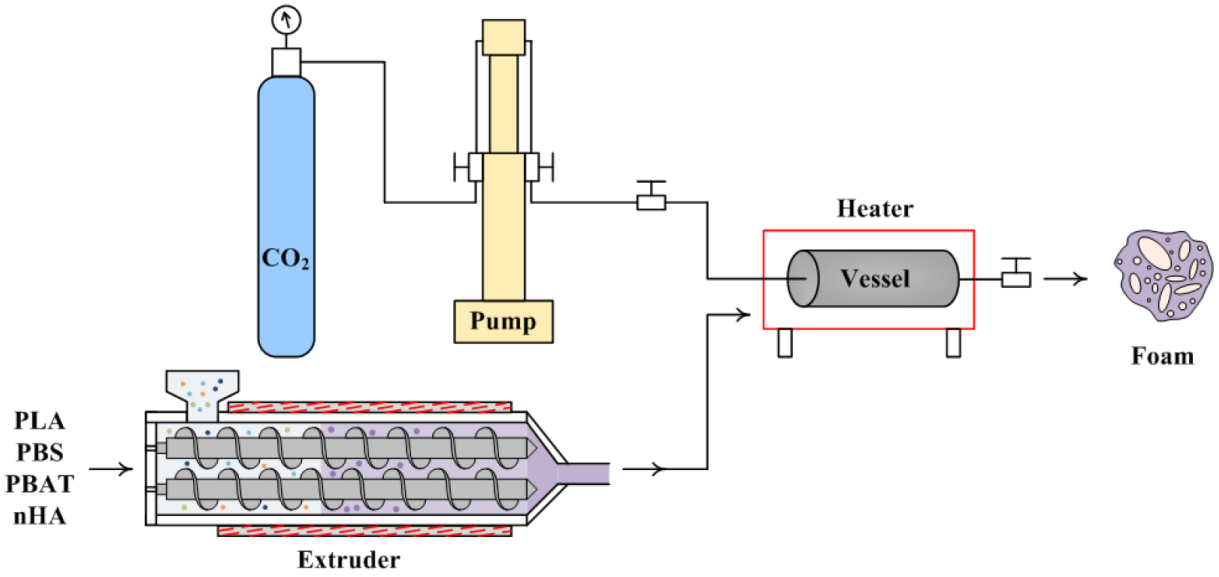

Figure 2-2. 本實驗所採用之超臨界二氧化碳發泡製程示意圖。

doi:10.6342/NTU202502722

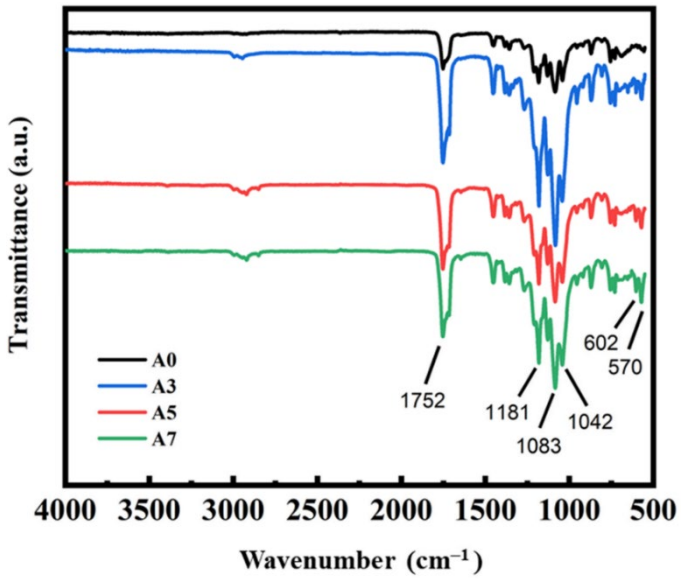

(a)

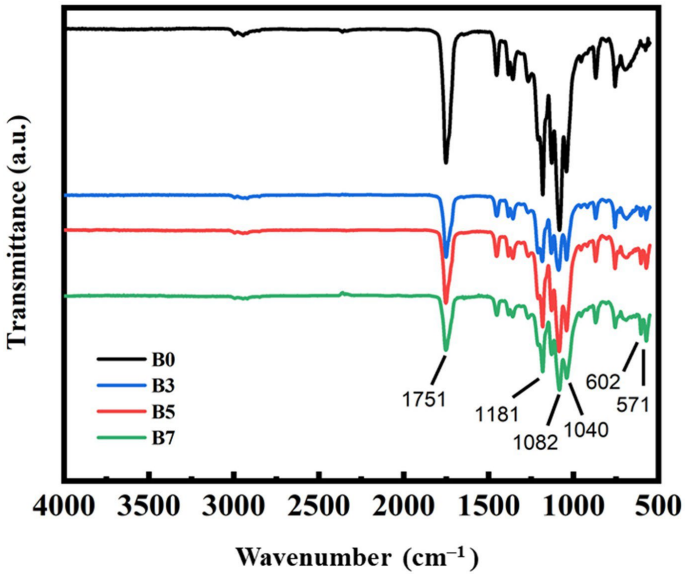

(b)

Figure 3-1. 高分子共混材料之 FTIR 測量結果： (a) 為樣本系列 A，(b) 為樣本系列 B，兩者皆添加不同含量之奈米羥基磷灰石（nHA）。

doi:10.6342/NTU202502722

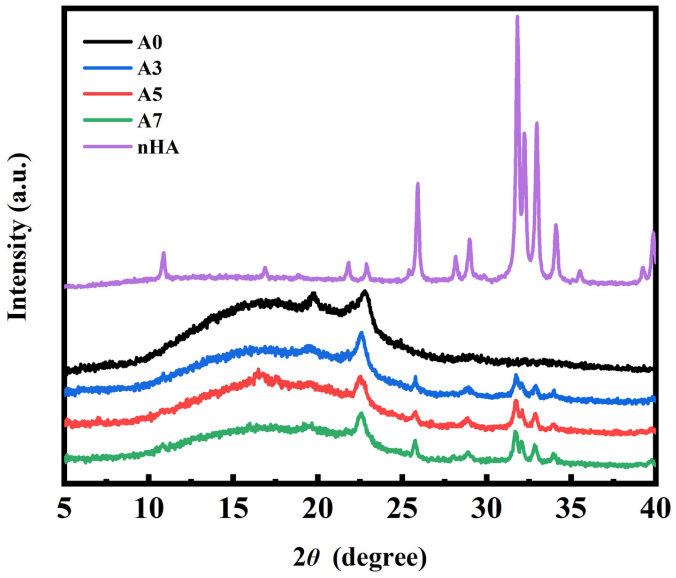

(a)

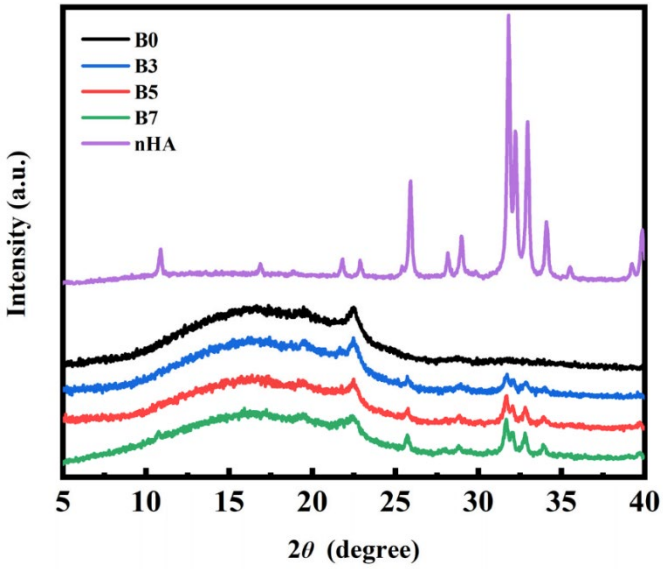

(b)

Figure 3-2. 高分子共混材料之 XRD 測量結果：(a) 樣本系列 A，與 (b) 樣本系列 B，兩者皆添加不同含量之奈米羥基磷灰石 (nHA)。

doi:10.6342/NTU202502722

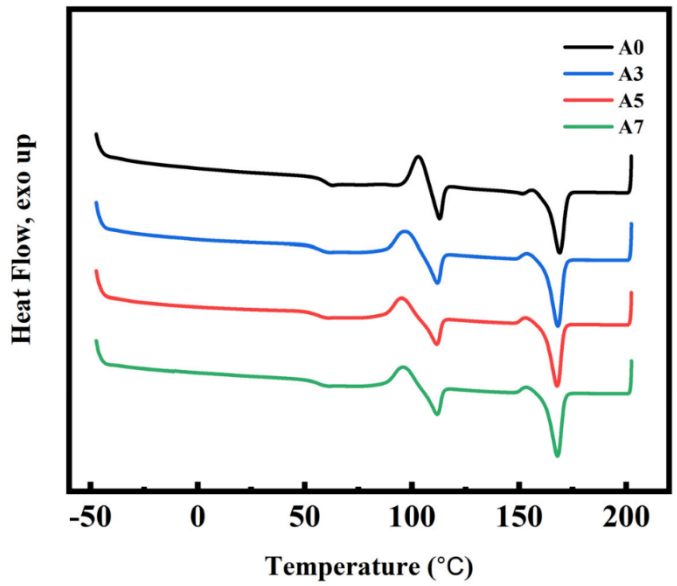

(a)

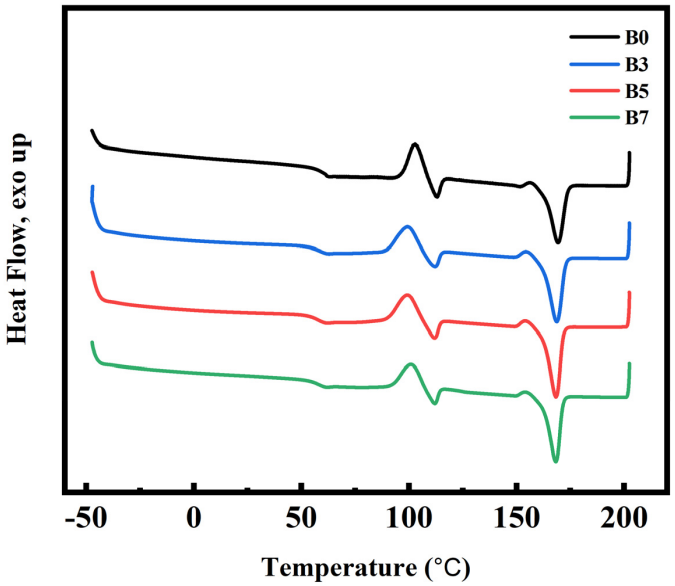

(b)

Figure 3-3. 高分子共混材料之 DSC 曲線（第二次加熱）：（a）樣本系列 A，與（b）樣本系列 B，兩者皆添加不同含量之奈米羥基磷灰石（nHA）。

doi:10.6342/NTU202502722

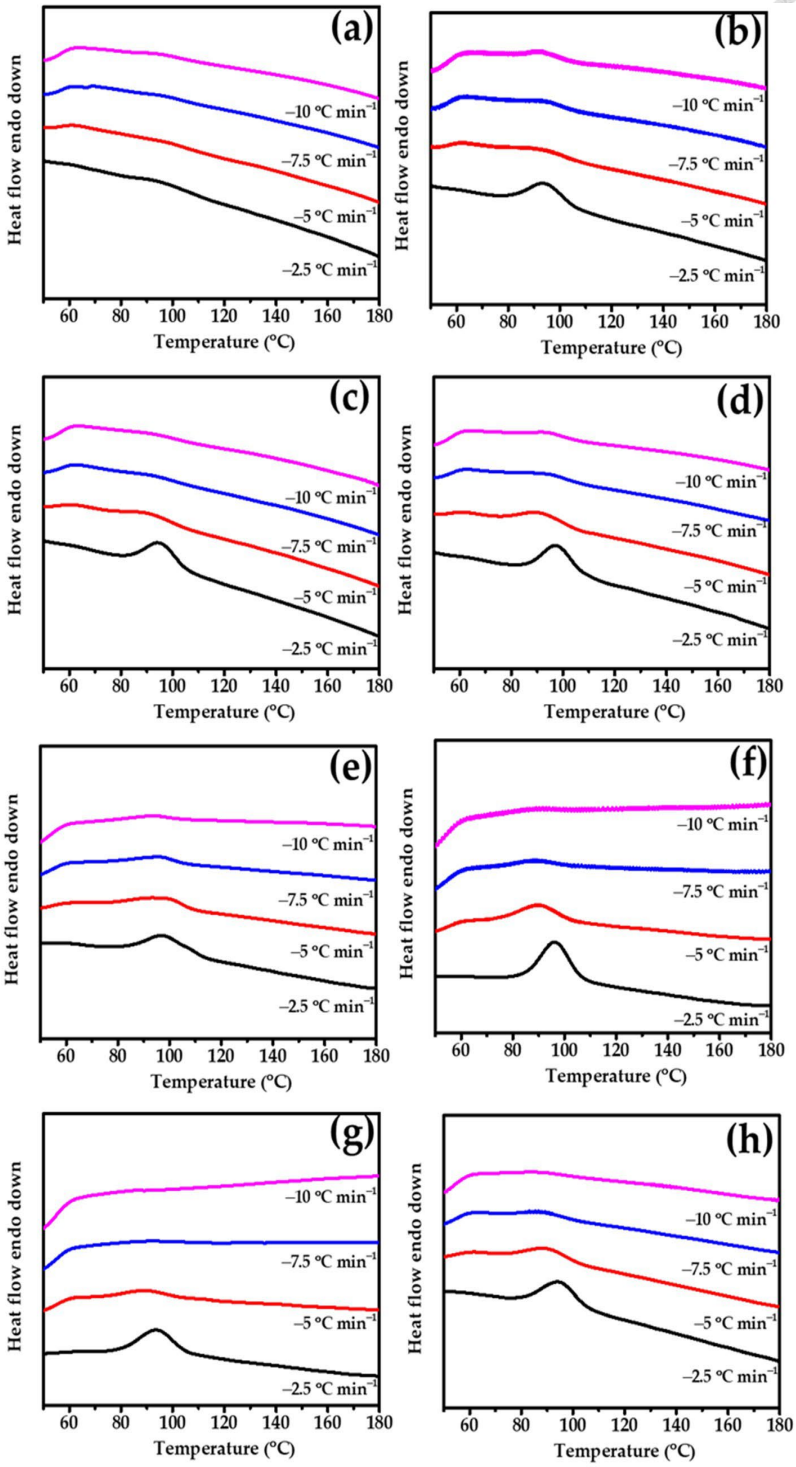

Figure 3-4. 樣本在冷卻過程中的 DSC 曲線，冷卻速率為 2.5、5、7.5 和 10°C min^{-1}。(a) A0，(b) A3，(c) A5，(d) A7，(e) B0，(f) B3，(g) B5，及 (h) B7。

doi:10.6342/NTU202502722

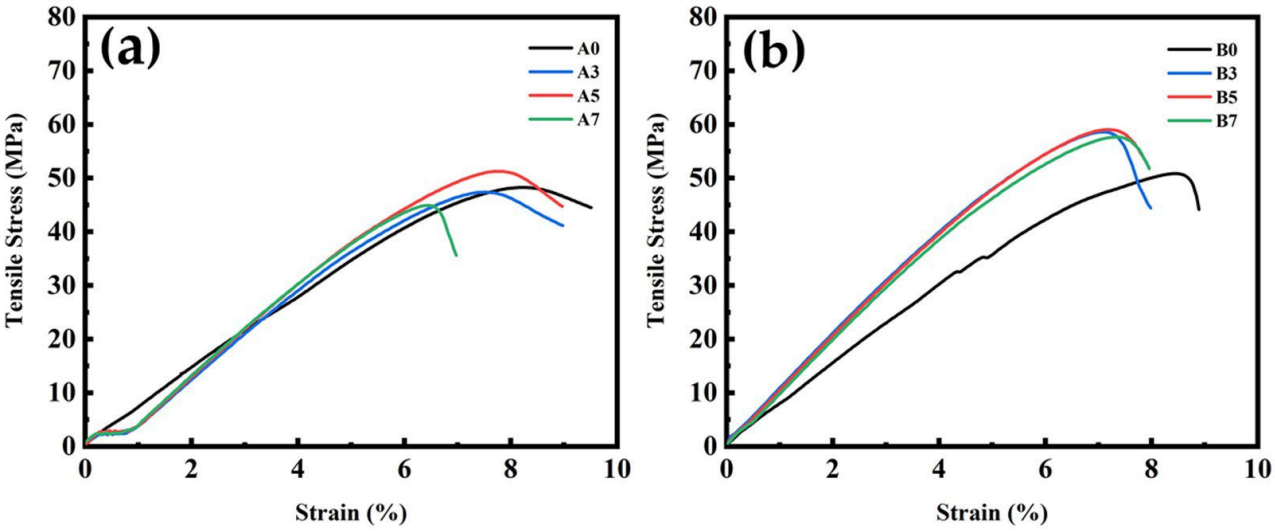

Figure 3-5. 高分子共混材料之拉伸應力測量結果：(a) 樣本系列 A；(b) 樣本系列 B，兩者皆添加不同含量之奈米羥基磷灰石（nHA）。

doi:10.6342/NTU202502722

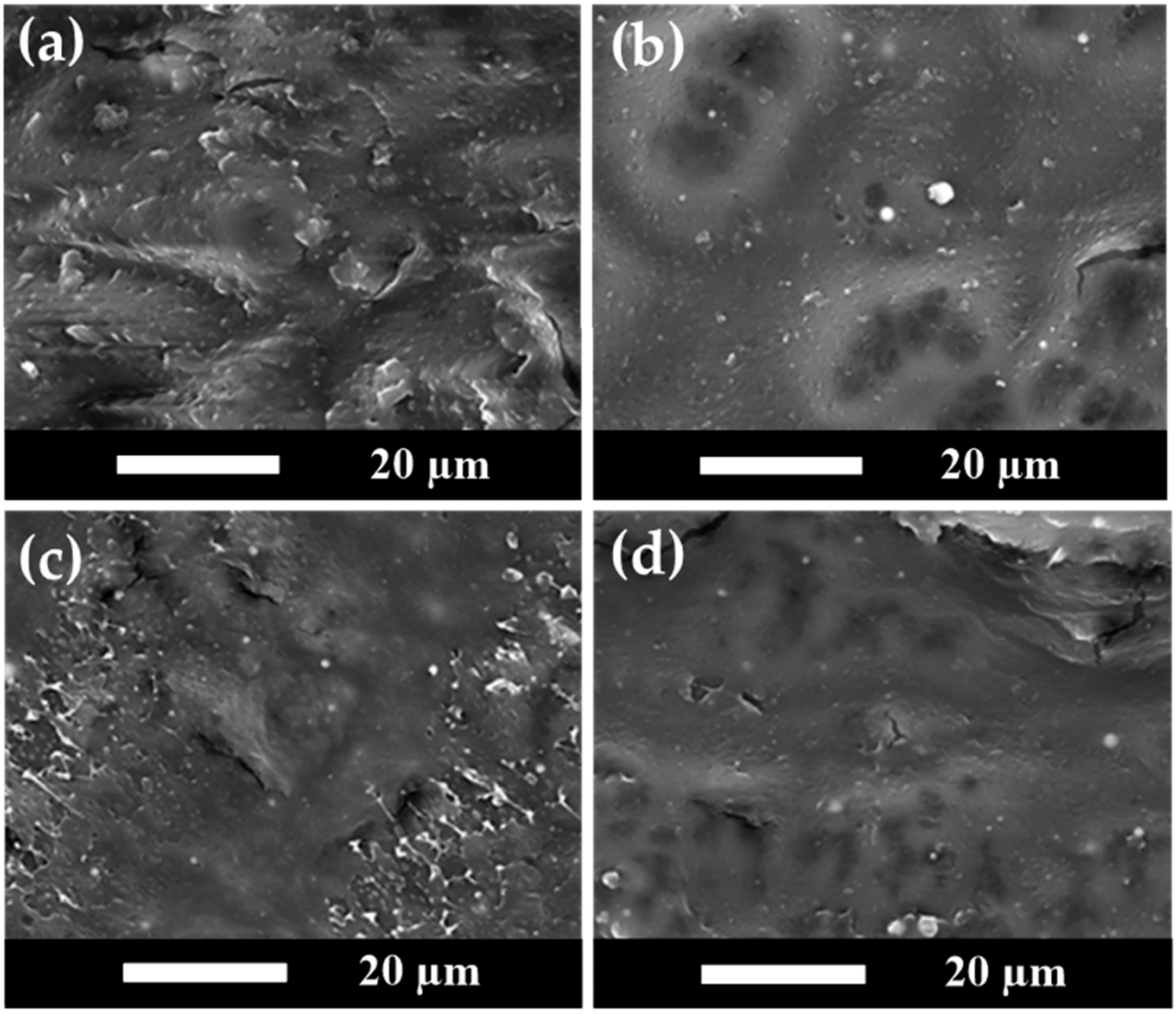

Figure 3-6. 高分子共混材料樣本系列 A 於添加不同含量奈米羥基磷灰石（nHA）下之 SEM 影像比較：(a) 樣本 A0；(b) 樣本 A3；(c) 樣本 A5；(d) 樣本 A7。

doi:10.6342/NTU202502722

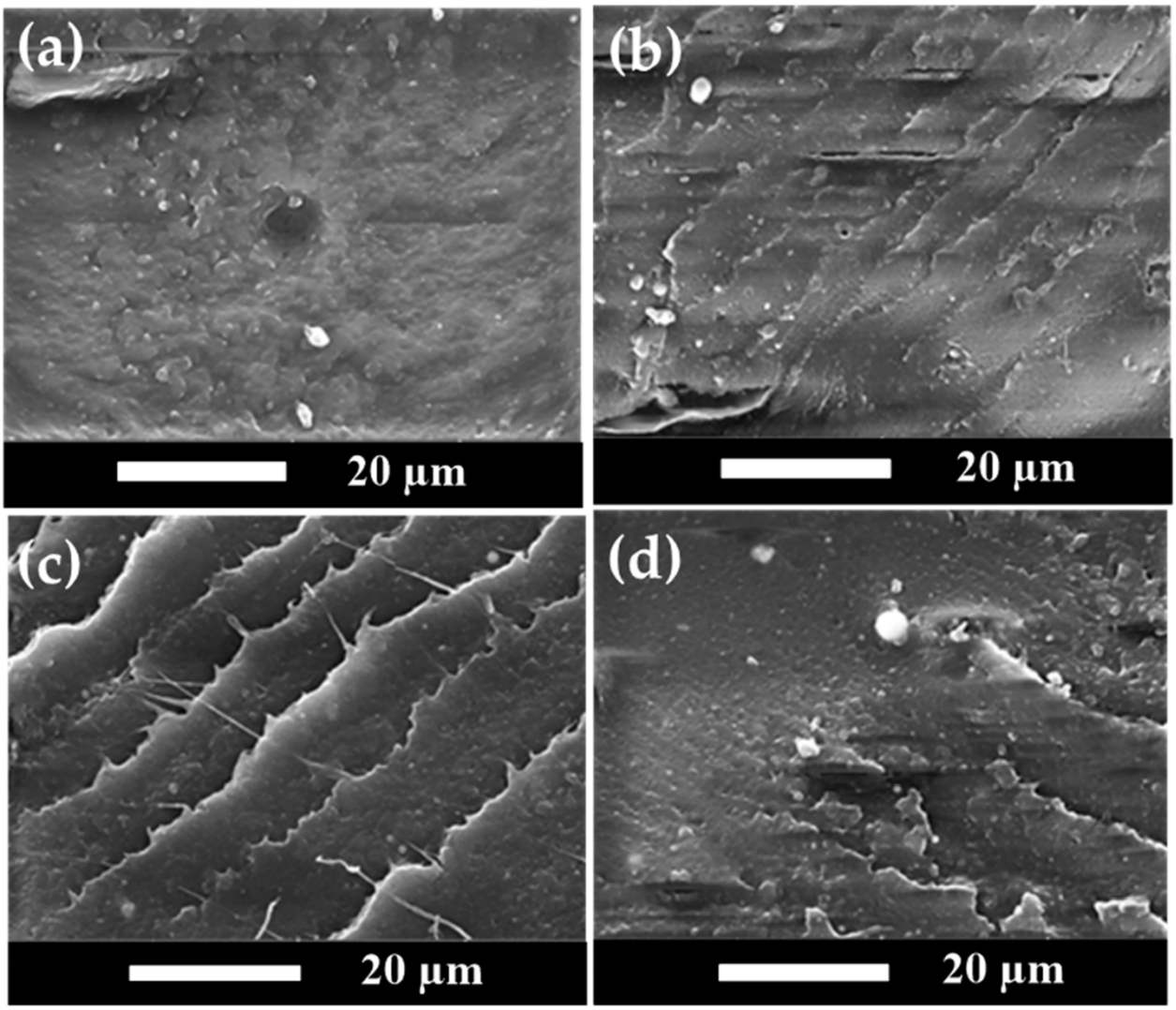

Figure 3-7. 高分子共混材料樣本系列 B 於添加不同含量奈米羥基磷灰石（nHA）下之 SEM 影像比較：(a) 樣本 B0；(b) 樣本 B3；(c) 樣本 B5；(d) 樣本 B7。

doi:10.6342/NTU202502722

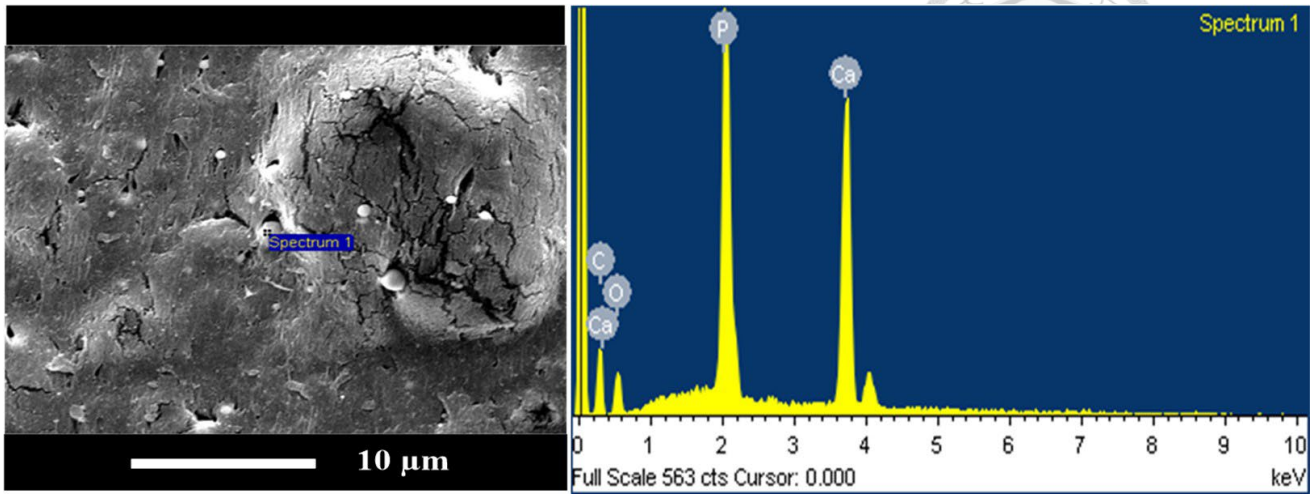

Figure 3-8. 高分子共混材料（樣本 B7，添加 7 wt% 奈米羥基磷灰石）之 EDX 能量散佈光譜測量結果。

doi:10.6342/NTU202502722

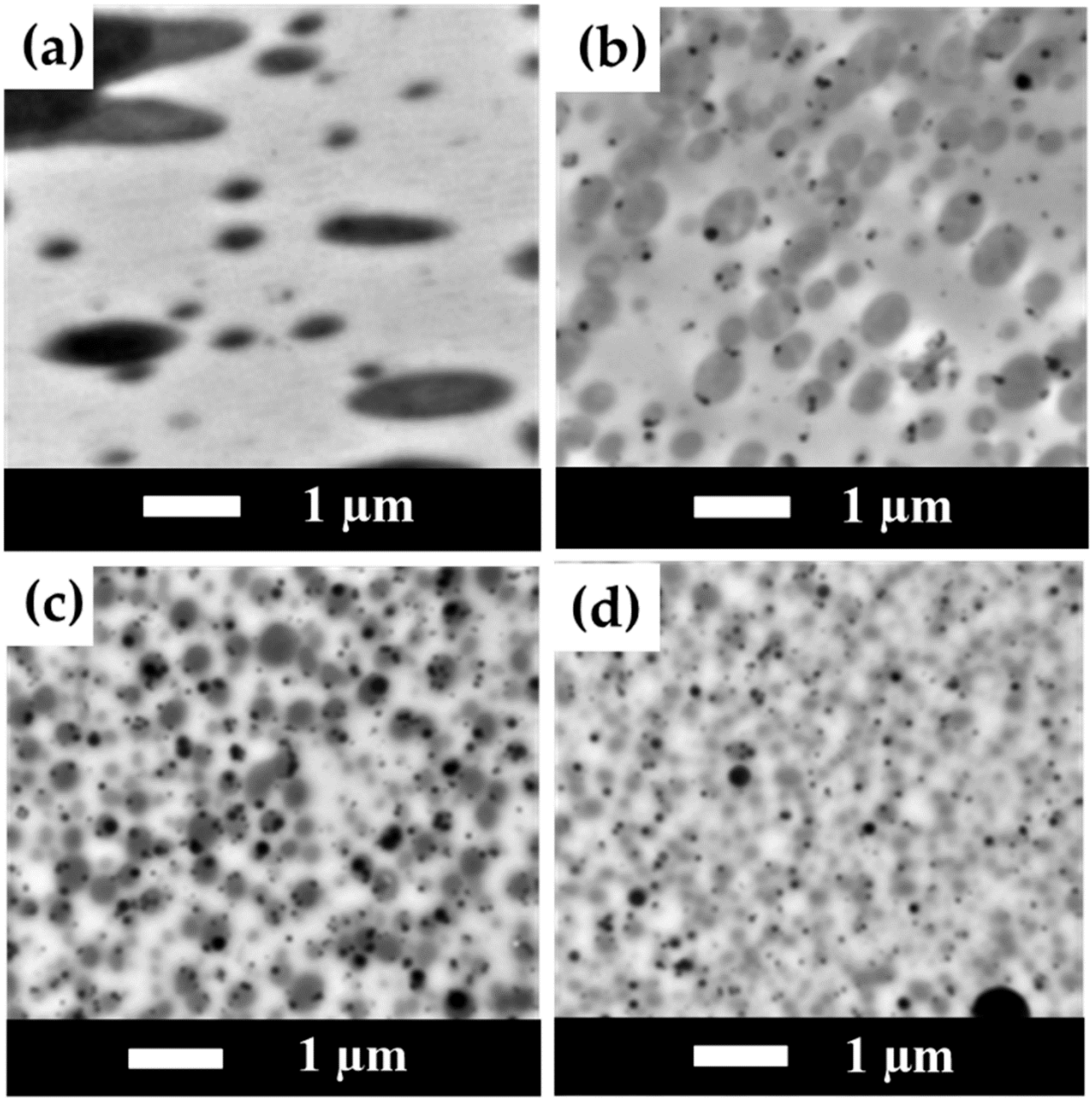

Figure 3-9. 樣本系列 A 高分子共混材料於添加不同含量奈米羥基磷灰石（nHA）下之 TEM 影像（放大倍率 20,000 倍）：（a）樣本 A0；（b）樣本 A3；（c）樣本 A5；（d）樣本 A7。

doi:10.6342/NTU202502722

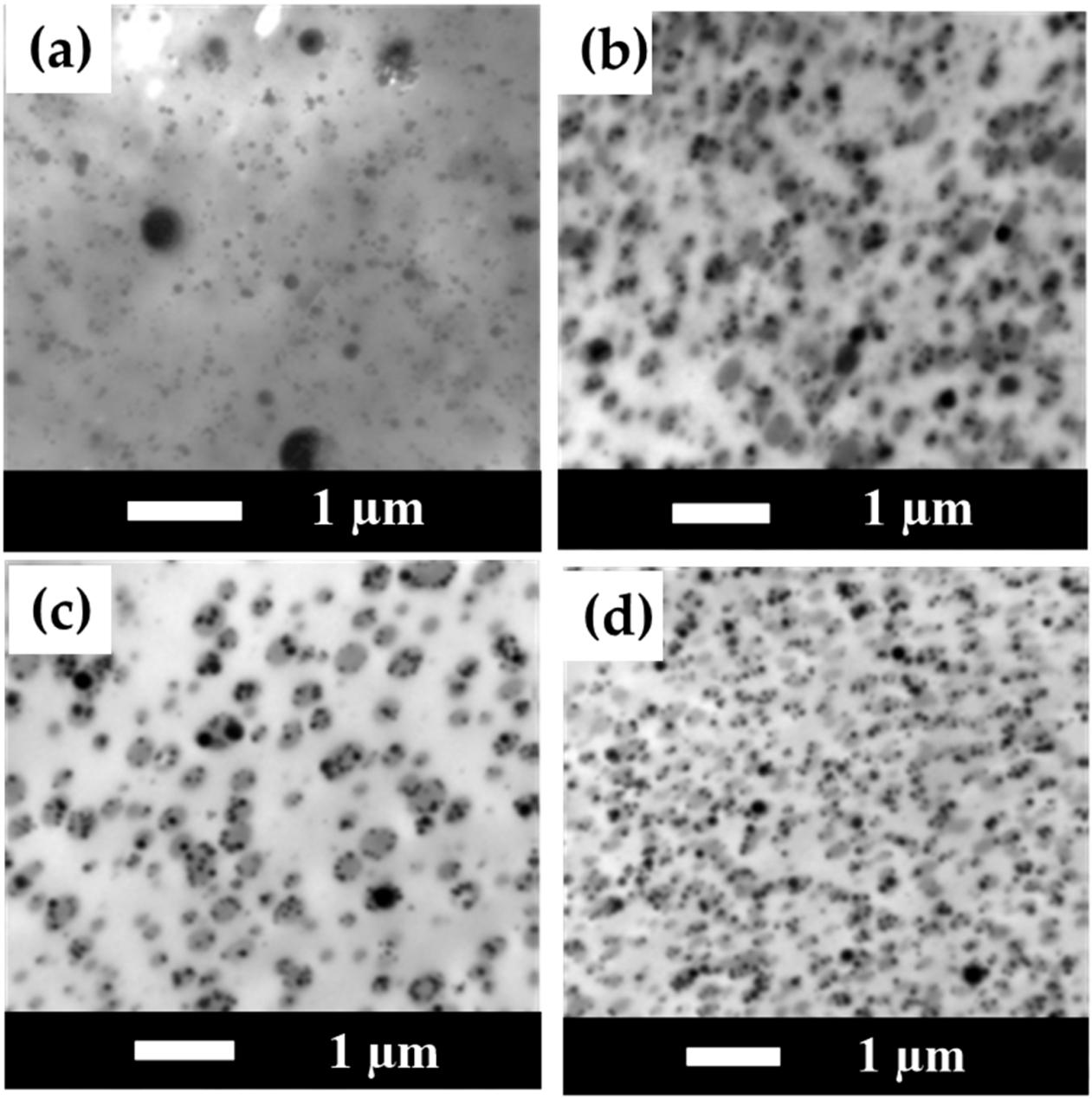

Figure 3-10. 樣本系列 B 高分子共混材料於添加不同含量奈米羥基磷灰石（nHA）下之 TEM 影像（放大倍率 20,000 倍）：（a）樣本 B0；（b）樣本 B3；（c）樣本 B5；（d）樣本 B7。

doi:10.6342/NTU202502722

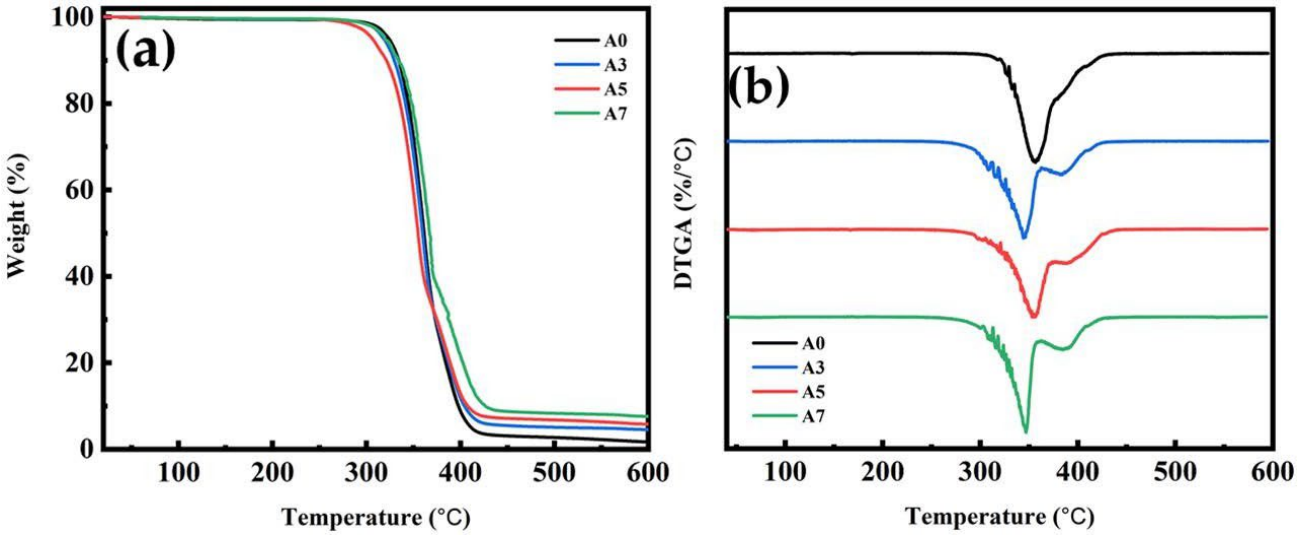

Figure 3-11. 樣本系列 A 於添加不同含量奈米羥基磷灰石（nHA）下之熱重分析結果：(a) 熱重曲線（TG）與 (b) 微分熱重曲線（DTG）。

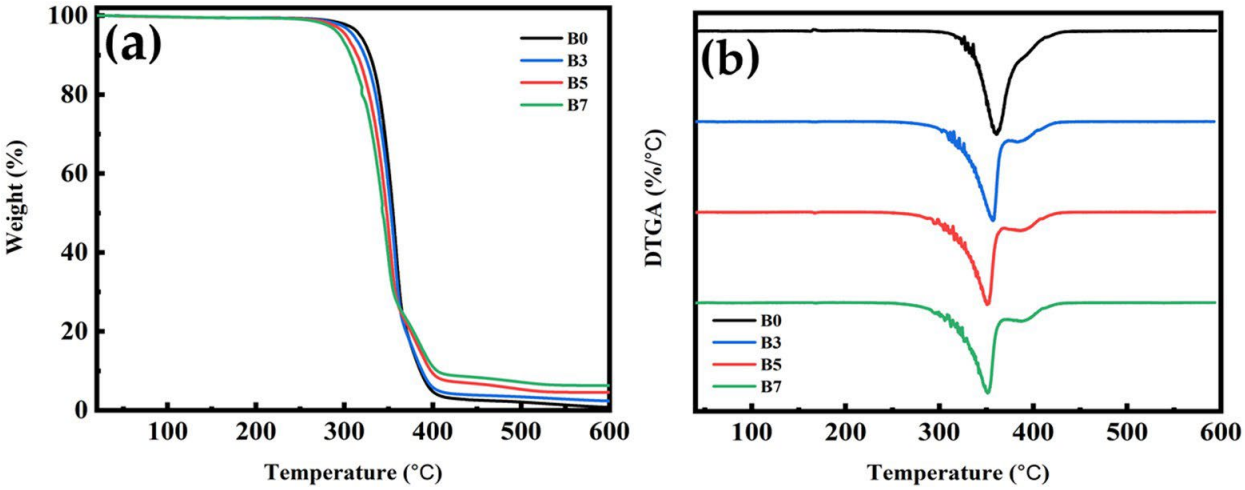

Figure 3-12. 樣本系列 B 於添加不同含量奈米羥基磷灰石（nHA）下之熱重分析結果：(a) 熱重曲線（TG）與 (b) 微分熱重曲線（DTG）。

doi:10.6342/NTU202502722

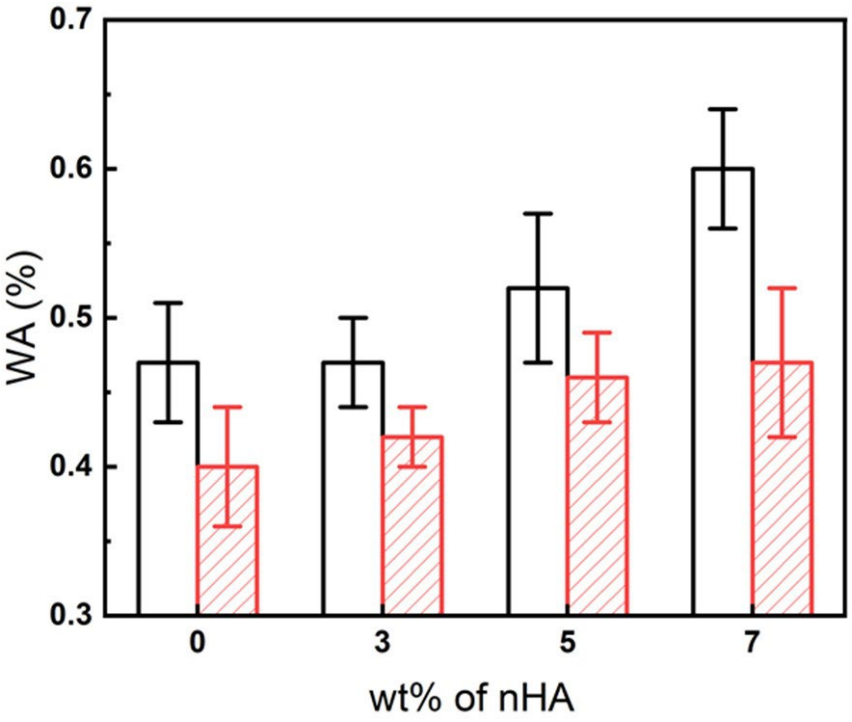

Figure 3-13. 不同奈米羥基磷灰石（nHA）含量下，所有樣本於 24 小時內吸水率（WA）百分比的比較。(▭：樣本系列 A；▨：樣本系列 B)。

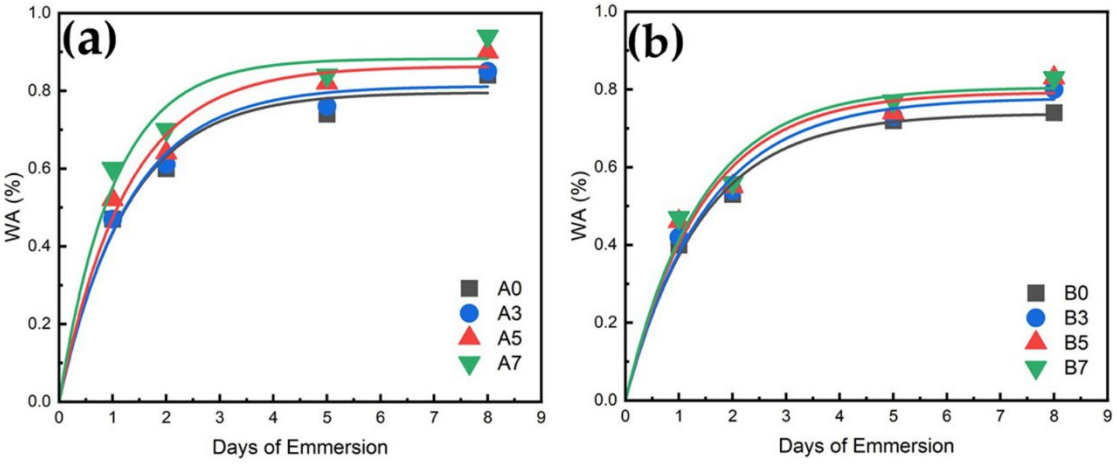

Figure 3-14. 吸水率曲線：(a) 樣本系列 A 及 (b) 樣本系列 B。

doi:10.6342/NTU202502722

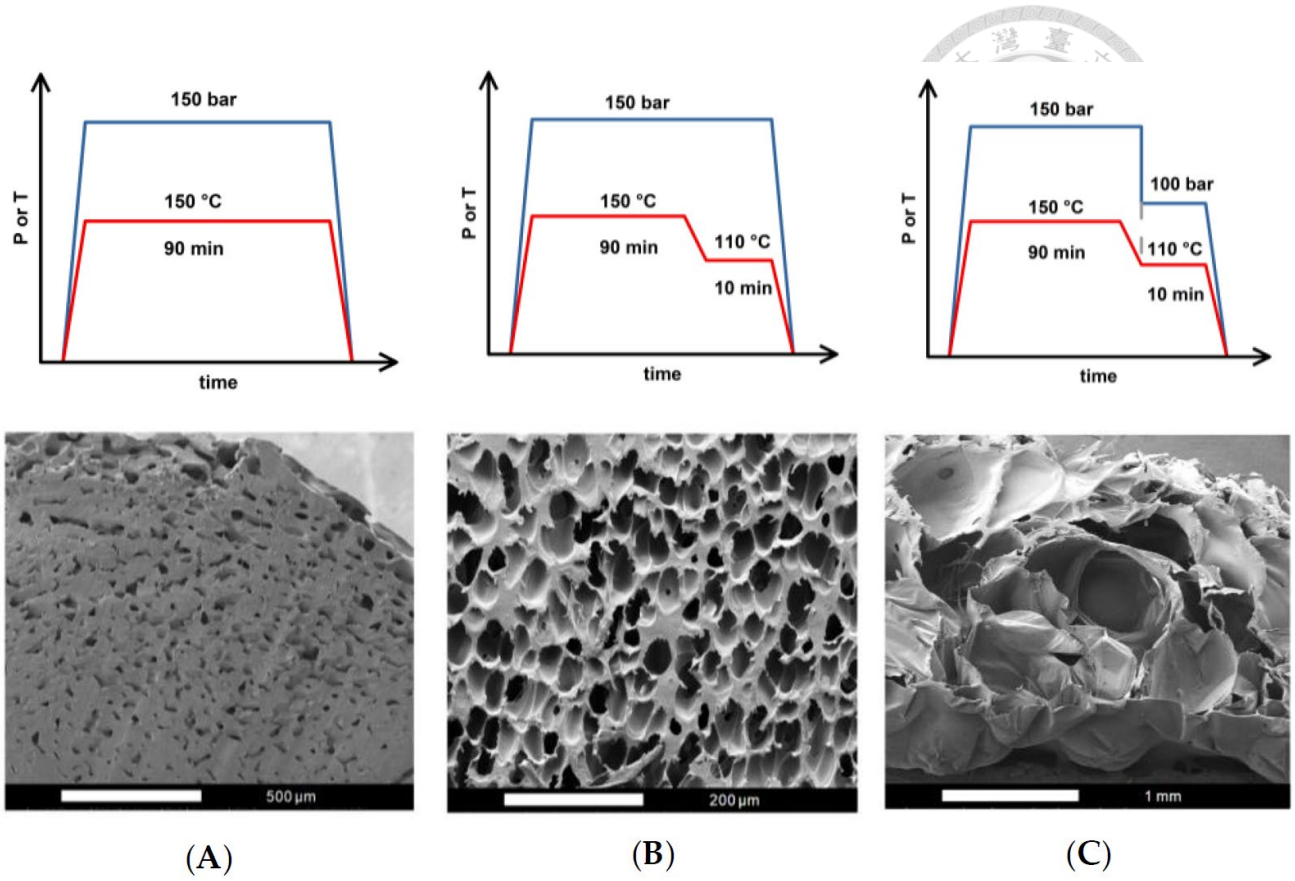

Figure 3-15. 發泡策略 A、B 及 C 之操作條件與 SEM 影像。

doi:10.6342/NTU202502722

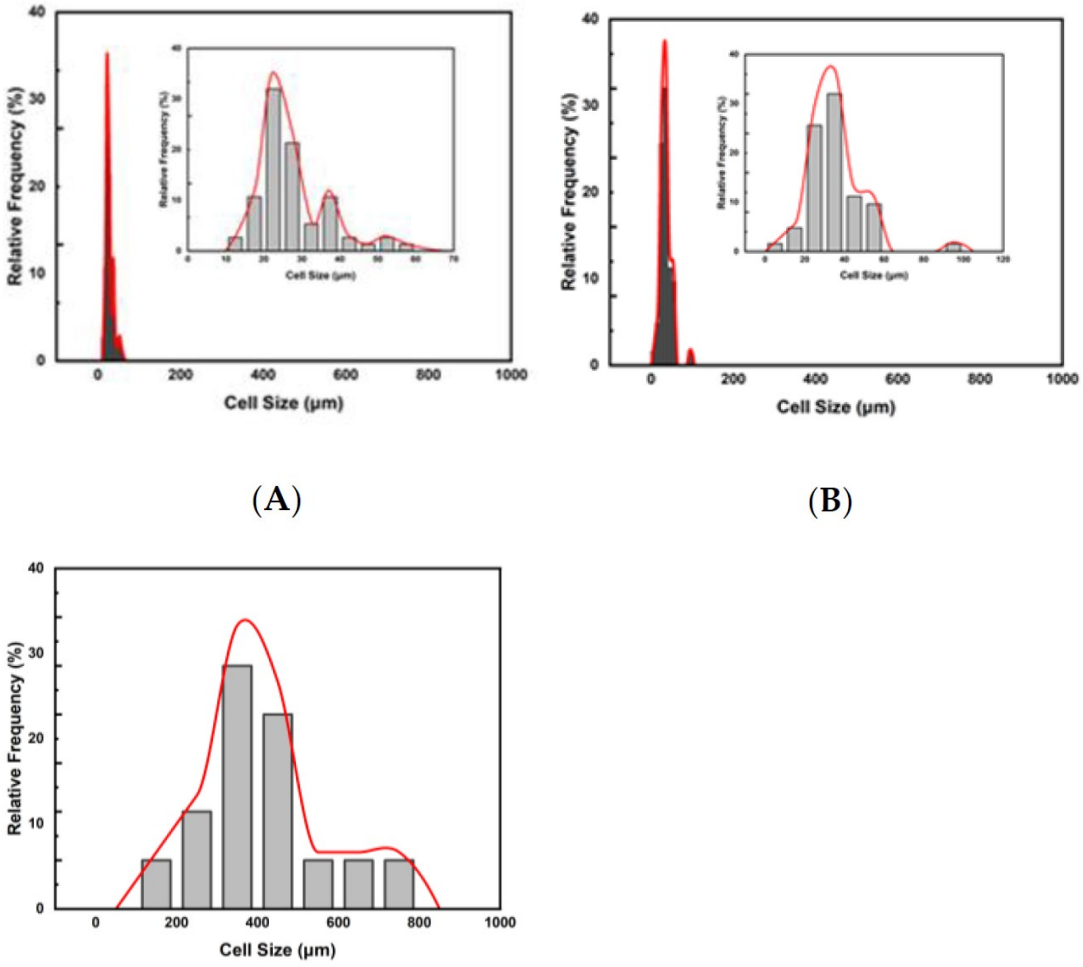

Figure 3-16. 發泡策略 A、B 及 C 之泡孔尺寸分布相對頻率圖。

doi:10.6342/NTU202502722

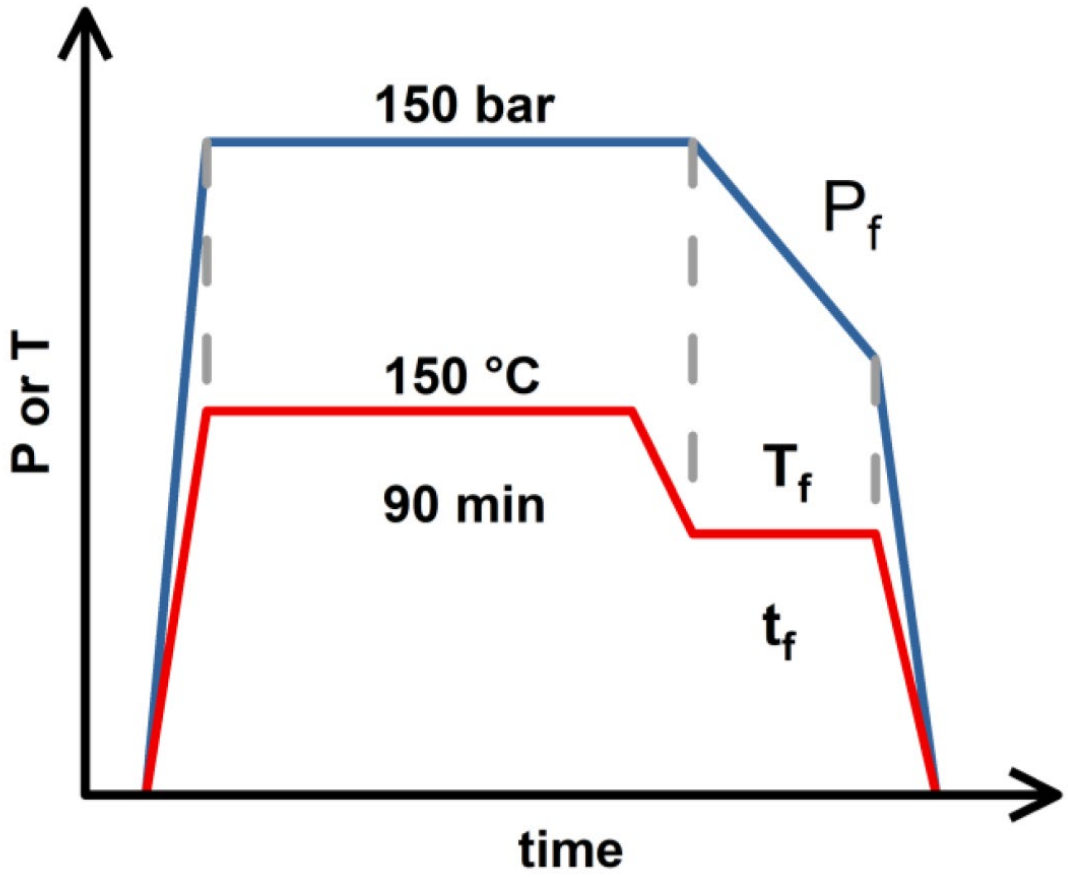

Figure 3-17. （2T-2P，階梯式壓力差 ΔP）發泡策略操作條件示意圖。

doi:10.6342/NTU202502722

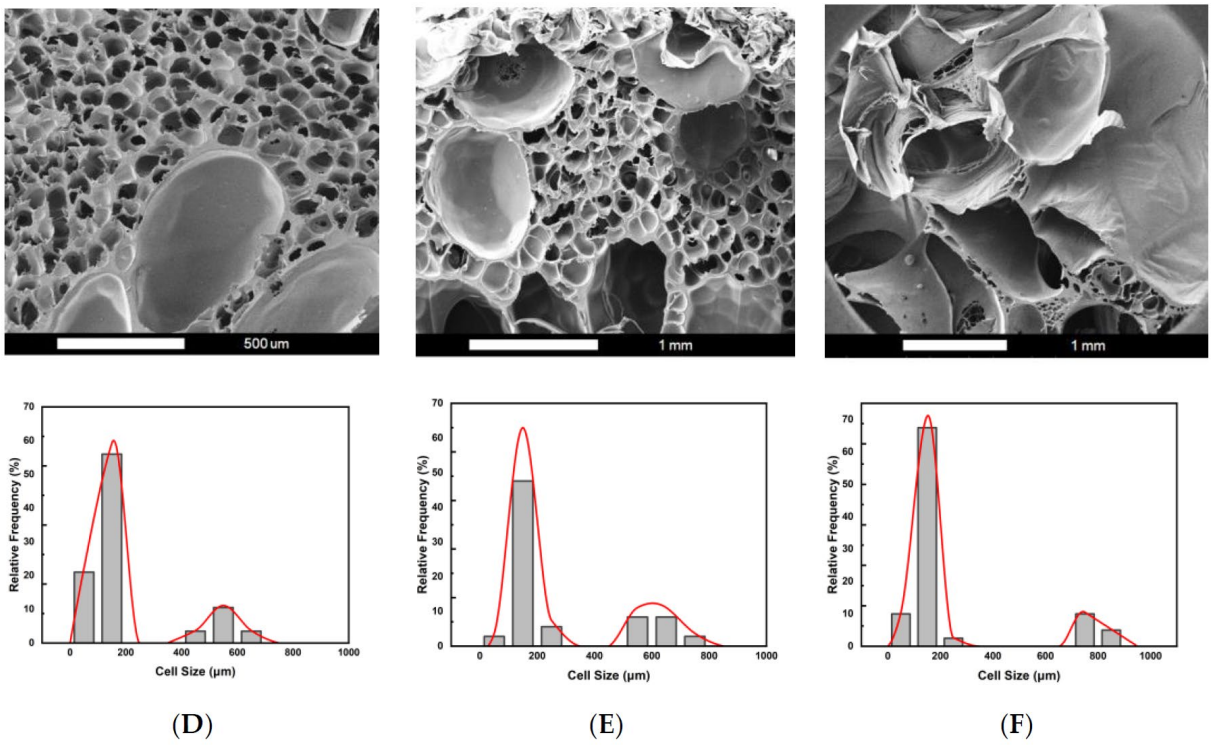

Figure 3-18. 發泡策略 D、E 及 F 之 SEM 影像及泡孔尺寸分布相對頻率結果。

doi:10.6342/NTU202502722

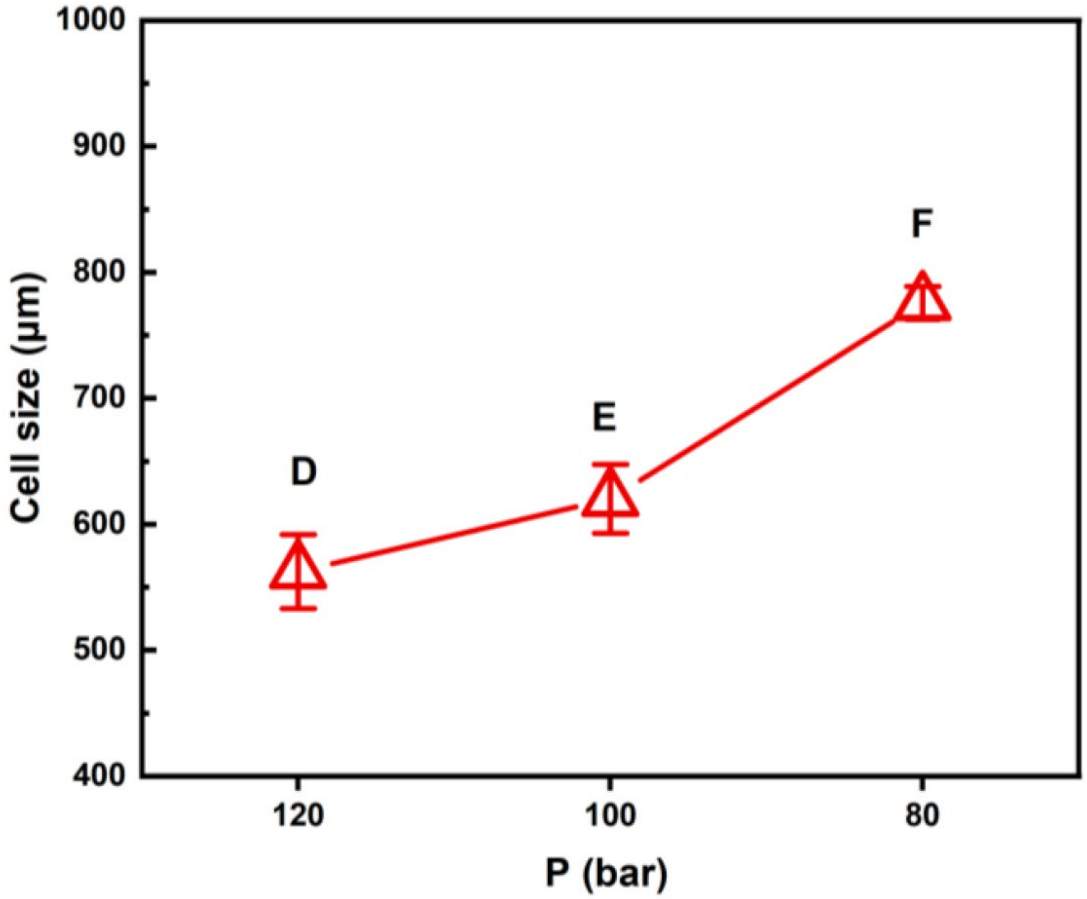

Figure 3-19. 發泡壓力對發泡策略 D、E 及 F 所產生大泡孔尺寸的影響。

doi:10.6342/NTU202502722

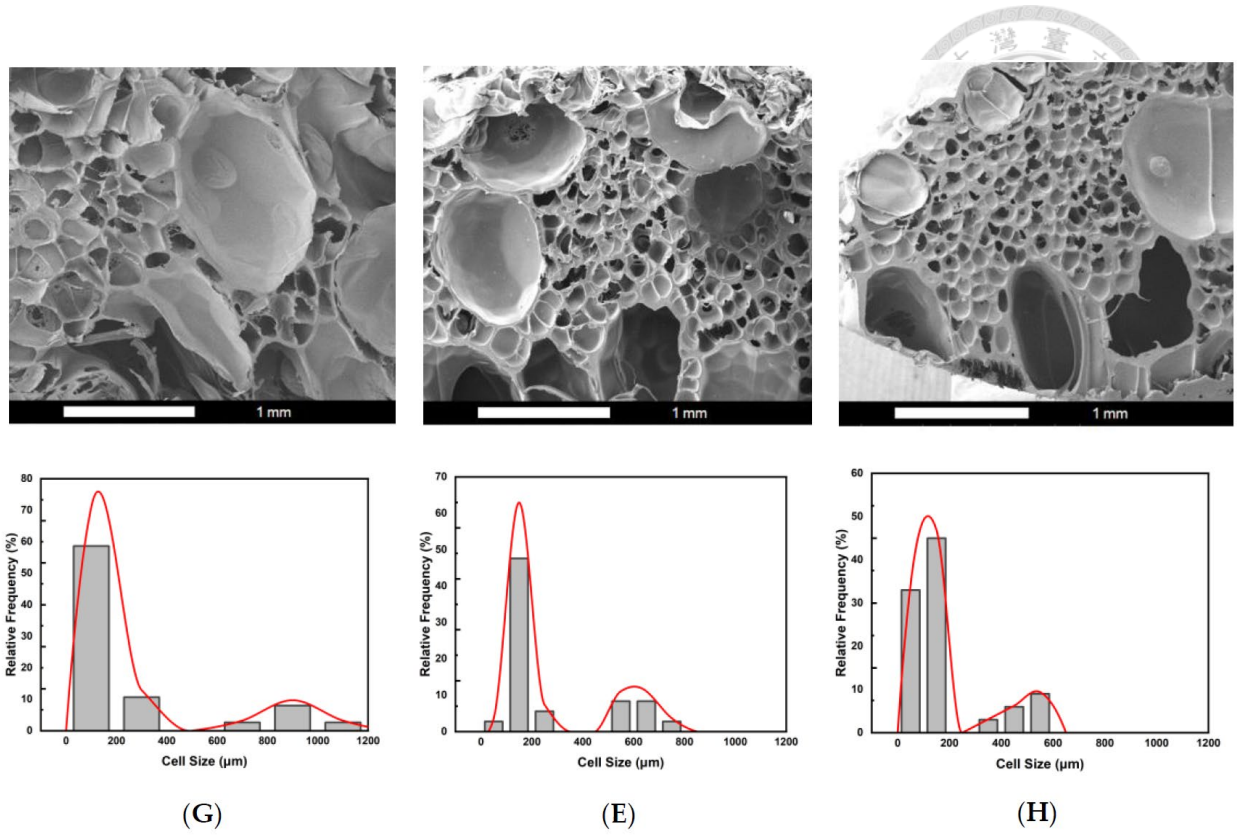

Figure 3-20. （2T-2P，階梯式壓力差 ΔP）發泡策略之 SEM 影像及泡孔尺寸分布相對頻率結果：（G）策略 G，中間溫度 100°C；（E）策略 E，中間溫度 110°C；（H）策略 H，中間溫度 120°C。

doi:10.6342/NTU202502722

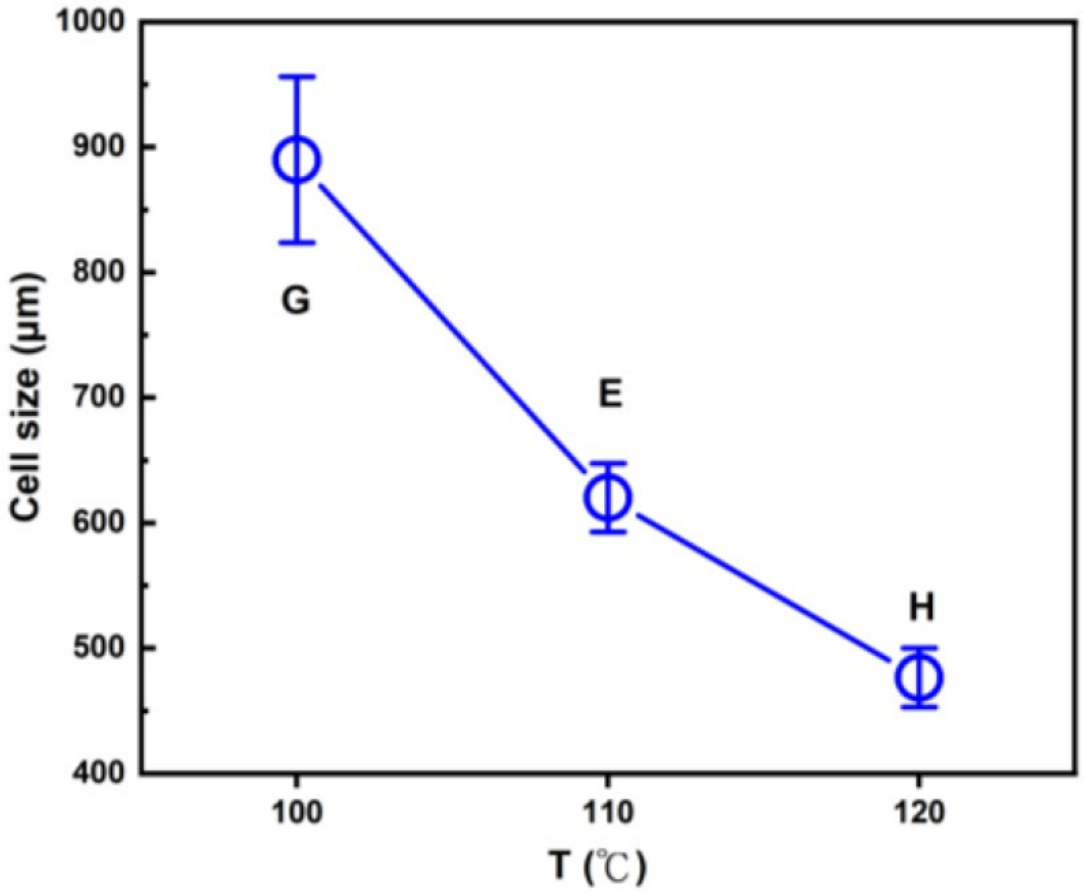

Figure 3-21. 發泡溫度對（2T-2P，階梯式壓力差 ΔP）發泡策略 G、E 及 H 所產生大泡孔尺寸的影響。

doi:10.6342/NTU202502722

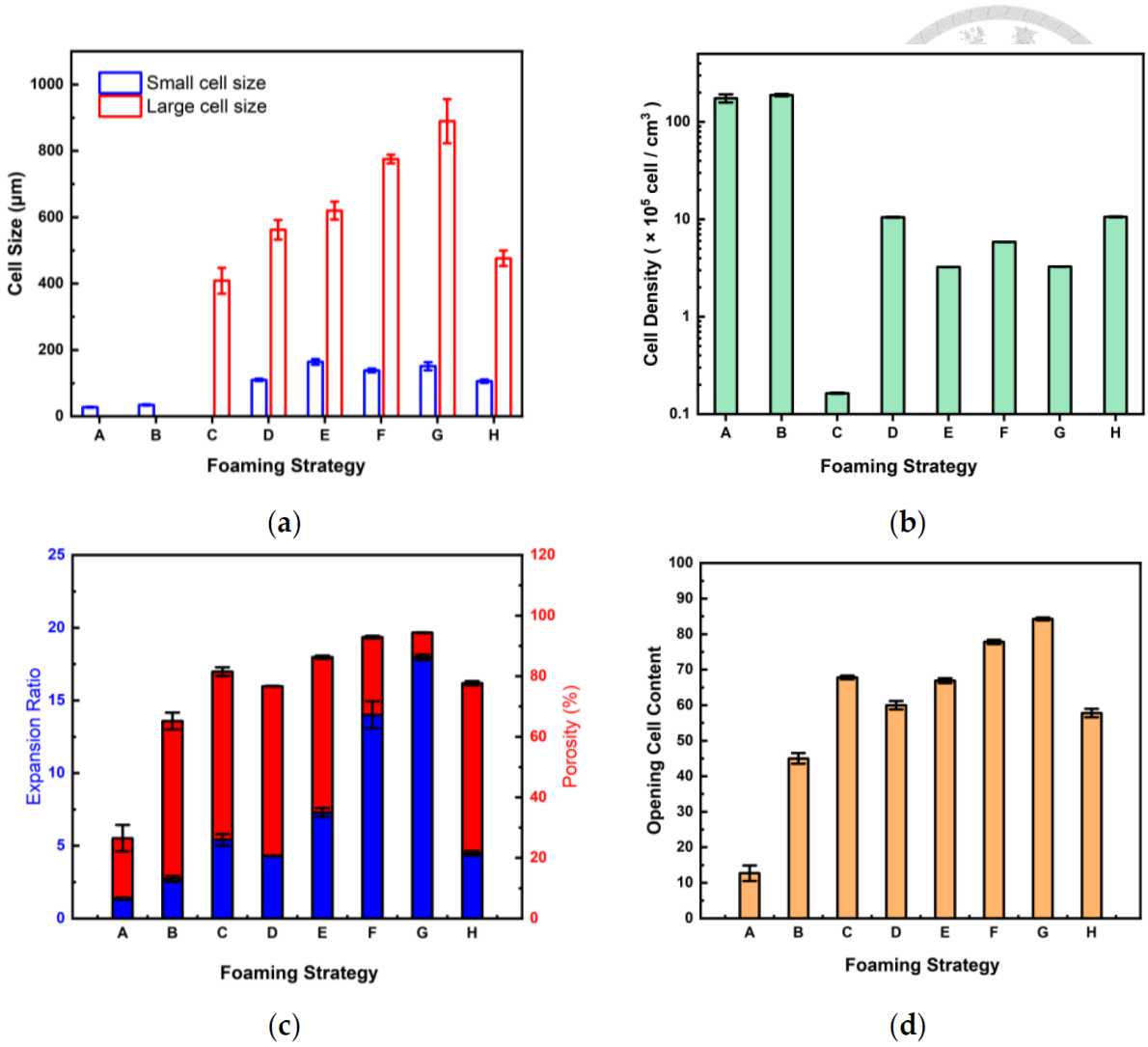

Figure 3-22. 本研究中採用發泡策略 A 至 H 所獲得之發泡高分子共混材料的實驗結果：(a) 泡孔徑大小，(b) 泡孔密度，(c) 膨脹倍率及孔隙率，(d) 泡孔開口率。

doi:10.6342/NTU202502722

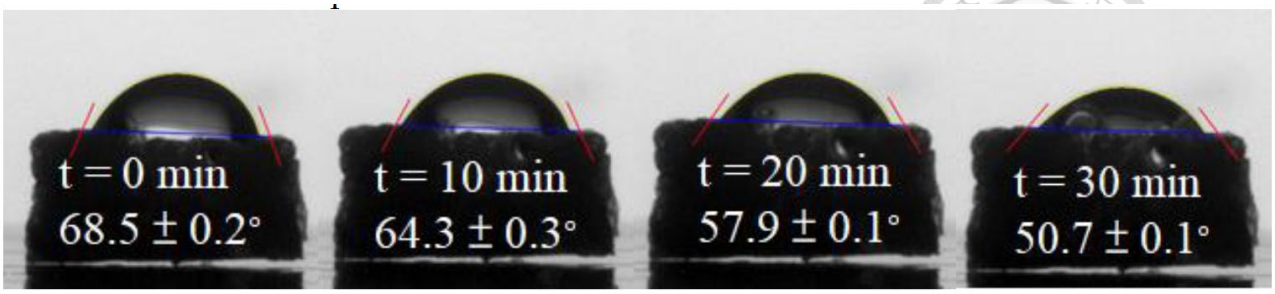

Figure 3-23. 採用發泡策略 E 製備之發泡高分子共混材料的水滴接觸角測量結果。

doi:10.6342/NTU202502722

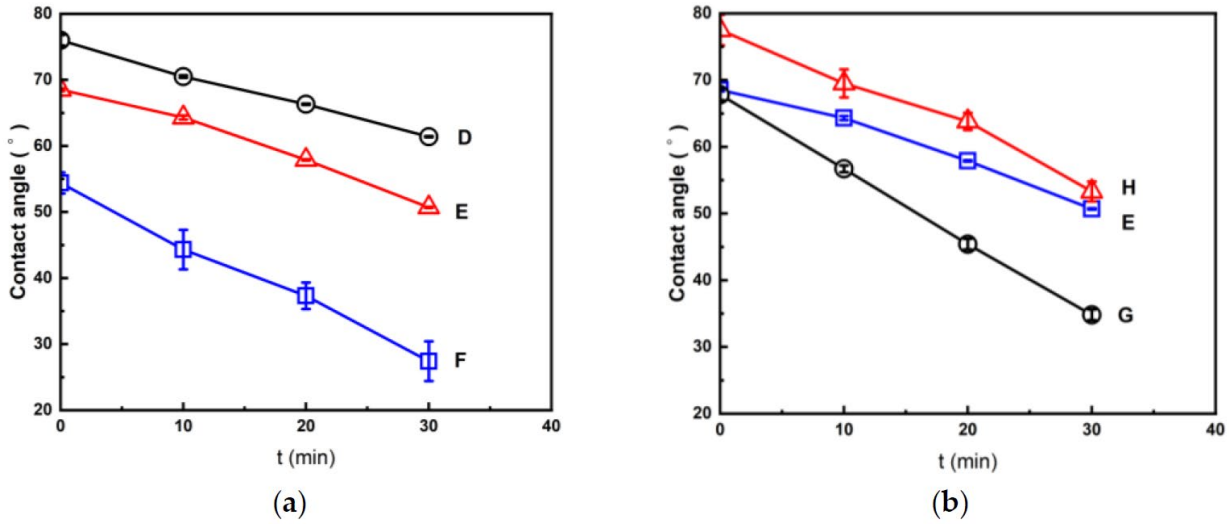

Figure 3-24. 發泡高分子共混材料水滴接觸角隨時間下降趨勢：(a) 發泡策略 D、E 與 F；(b) 發泡策略 G、E 與 H。

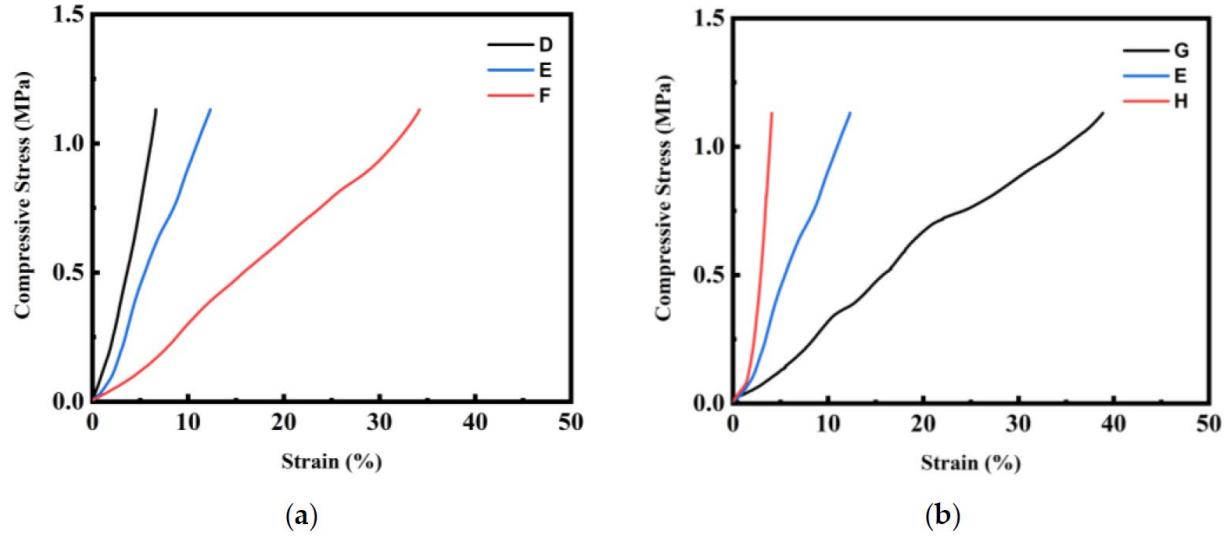

Figure 3-25. 發泡高分子共混材料之壓縮應力-應變曲線：(a) 發泡策略 D、E 與 F；(b) 發泡策略 G、E 與 H。

doi:10.6342/NTU202502722

表格

Table 2-1. 本研究所使用高分子材料之物理及機械性質[a]。

Physical Properties	PLA	PBS	PBAT
Density (g/cm^3)	1.24	1.26	1.25–1.27
Melt flow index (g/10 min, at 190 °C, 2.16 kg)	7	5	2.7–4.9
Melting temperature, T_m (°C)	155–170	115	110–120
Tensile yield strength (MPa)	60	39	36
Tensile modulus (GPa)	3.5	0.58	–
Tensile elongation (%)	6.0	350	560

[a]: according to the suppliers.

Table 2-2. 本研究中所使用之 PLA/PBS/PBAT/nHA 共混材料配方組成。

Specimen Code	PLA (wt%)	PBS (wt%)	PBAT (wt%)	nHA (wt%)
		Sample with 60 wt% PLA		
PLA60	60	25	15	0
		Sample series A		
A0	70	20	10	0
A3	70	20	10	3
A5	70	20	10	5
A7	70	20	10	7
		Sample series B		
B0	80	15	5	0
B3	80	15	5	3
B5	80	15	5	5
B7	80	15	5	7

doi:10.6342/NTU202502722

Table 3-1. PLA/PBS/PBAT 共混材料之拉伸測試結果。

Sample of PLA/PBS/PBAT Blends	Maximum Tensile Stress (MPa)	Elongation at Maximum Tensile Stress (%)	Tensile Modulus (MPa)
PLA60	37.6 ± 1.8	7.0 ± 0.5	584.8 ± 71.9
A0	47.1 ± 2.9	7.9 ± 0.4	642.0 ± 109.1
B0	49.6 ± 1.6	8.0 ± 0.6	686.1 ± 91.3

Table 3-2. 高分子共混材料之 DSC 測試結果及計算得出的結晶度。

Specimen Code	$T_{g,PLA}$ (°C)	T_{cc} (°C)	$T_{m,PLA}$ (°C)	ΔH_{cc} (J g^{-1})	ΔH_m (J g^{-1})	X_c (%)
A0	62	103	169	12.0	36.3	20.1
A3	63	100	169	13.0	41.9	24.8
A5	63	99	168	14.9	45.2	26.0
A7	61	99	168	13.5	45.0	27.0
B0	62	103	169	15.7	37.9	20.1
B3	63	101	169	18.6	41.3	20.6
B5	63	102	169	15.6	40.2	22.3
B7	63	102	169	14.8	38.5	21.5

doi:10.6342/NTU202502722

Table 3-3. 樣本系列 A 與 B 在不同冷卻速率下之結晶化焓值。

Specimen Code	Cooling Rate (°C min^{-1})			
	2.5	5	7.5	10
	ΔH_{hc} (J g^{-1})			
A0	0	0	0	0
A3	7.80	1.08	0.63	0.37
A5	9.88	1.70	0.45	0.41
A7	10.90	2.72	0.91	0.50
B0	10.12	3.46	0.74	0.55
B3	11.96	3.31	0.94	0.46
B5	10.09	2.56	0.84	0.36
B7	10.91	2.71	0.94	0.48

Table 3-4. 不同奈米羥基磷灰石（nHA）含量共混高分子材料之拉伸及衝擊測試結果。

Specimen Code	Maximum Tensile Stress (MPa)	Elongation at Maximum Tensile Stress (%)	Tensile Modulus (MPa)	Impact Strength (kJ m^{-2})
A0	47.1 ± 2.9	7.9 ± 0.4	642.0 ± 109.1	4.83 ± 0.19
A3	47.5 ± 0.7	7.5 ± 0.3	887.8 ± 57.2	4.32 ± 0.17
A5	50.2 ± 1.0	7.4 ± 0.4	905.5 ± 64.1	4.64 ± 0.21
A7	47.4 ± 0.3	6.7 ± 0.3	707.5 ± 15.0	4.20 ± 0.07
B0	49.6 ± 1.6	8.0 ± 0.6	686.1 ± 91.3	3.36 ± 0.20
B3	57.8 ± 0.7	7.1 ± 0.2	1039.4 ± 37.5	3.21 ± 0.16
B5	57.9 ± 1.0	7.3 ± 0.2	1062.2 ± 97.8	3.42 ± 0.17
B7	56.7 ± 1.0	7.3 ± 0.1	962.6 ± 17.4	3.19 ± 0.25

doi:10.6342/NTU202502722

Table 3-5. PLA/PBS/PBAT/nHA 共混材料之熱重分析結果。

Specimen Code	$T_{5\%}$ (°C)	$T_{50\%}$ (°C)	T_{max} (°C)	W_R (%) at 600 °C
A0	325	361	361	1.6
A3	318	360	360	4.5
A5	306	354	355	5.7
A7	319	367	366	7.6
B0	317	355	371	0.7
B3	310	353	369	2.3
B5	302	348	362	4.5
B7	295	343	352	6.3

Table 3-6. 本研究中所有操作策略之發泡結果彙整。

Operating Strategy	Expansion Ratio	Porosity (%)	Cell Density (cell/cm³)	Cell size (μm) (Small/Large)	Opening Cell Content (%)
A	1.36 ± 0.08	26.5 ± 4.4	(1.75 ± 0.17) × 10^7	27.6 ± 1.1/—	12.7 ± 2.2
B	2.72 ± 0.21	65.2 ± 2.8	(1.89 ± 0.05) × 10^7	34.2 ± 1.9/—	45.0 ± 1.5
C	5.41 ± 0.40	81.5 ± 1.4	(1.64 ± 0.02) × 10^4	—/408.7 ± 38.7	67.8 ± 0.5
D	4.30 ± 0.02	76.7 ± 0.1	(1.05 ± 0.01) × 10^6	109.9 ± 3.2/562.0 ± 29.4	60.0 ± 1.2
E	7.29 ± 0.30	86.3 ± 0.5	(3.24 ± 0.01) × 10^5	164.2 ± 8.4/602.1 ± 27.3	66.9 ± 0.7
F	14.01 ± 0.93	92.9 ± 0.4	(5.86 ± 0.02) × 10^5	138.2 ± 5.4/775.6 ± 13.0	77.8 ± 0.6
G	17.96 ± 0.20	94.4 ± 0.1	(3.27 ± 0.01) × 10^5	151.1 ± 12.1/889.8 ± 66.2	84.3 ± 0.4
H	4.48 ± 0.16	77.7 ± 0.7	(1.06 ± 0.01) × 10^6	105.9 ± 5.1/476.4 ± 23.6	57.8 ± 1.2

doi:10.6342/NTU202502722

參考文獻

[1] Liu, A.P.; Appel, E.A.; Ashby, P.D.; Baker, B.M.; Franco, E.; Gu, L.; Haynes, K.; Joshi, N.S.; Kloxin, A.M.; Kouwer, P.H.J.; et al. The living interface between synthetic biology and biomaterial design. Nat. Mater. 2022, 21, 390–397. (https://doi.org/10.1038/s41563-022-01231-3)

[2] Eldeeb, A.E.; Salah, S.; Elkasabgy, N.A. Biomaterials for tissue engineering applications and current updates in the field: A comprehensive review. AAPS PharmSciTech 2022, 23, 267. (https://doi.org/10.1208/s12249-022-02419-1)

[3] Esmaeili, Y.; Bidram, E.; Bigham, A.; Atari, M.; Azadani, R. N.; Tavakoli, M.; Salehi, S.; Mirhaj, M.; Basiri, A.; Mirzavandi, Z.; Boshtam, M.; Rafienia, M.; Kharazi, A. Z.; Karbasi, S.; Shariati, L.; Zarrabi, A. Exploring the evolution of tissue engineering strategies over the past decade: From cell-based strategies to gene-activated matrix, Alex. Eng. J., 2023, 81, 137-169. (https://doi.org/10.1016/j.aej.2023.08.080)

[4] Al-Shalawi, F. D.; Ariff, A. H. M.; Jung, D.-W.; Ariffin, M. K. A. M.; Kim, C. L. S.; Brabazon, D.; Al-Osaimi, M. O. Biomaterials as implants in the orthopedic field for regenerative medicine: metal versus synthetic polymers. Polymers 2023, 15, No. 2601. (https://doi.org/10.3390/polym15122601)

[5] Ajmal, S.; Hashmi, F. A.; Imran, I. Recent progress in development and applications of biomaterials. Mater. Today: Proc., 2022, 62, 385-391. (https://doi.org/10.1016/j.matpr.2022.04.233)

[6] Paternoster, J. L.; Vranckx, J. J. State of the art of clinical applications of tissue engineering in 2022, Tissue Eng. Part B Rev., 2022, 28, 592-612. (https://doi.org/10.1089/ten.teb.2021.0017)

[7] Jang, J.-W.; Min, K.-E.; Kim, C.; Shin, J.; Lee, J.; Yi, S. Review: scaffold

doi:10.6342/NTU202502722

characteristics, fabrication methods, and biomaterials for the bone tissue engineering, Int. J. Precis. Eng. Manuf., 2023, 24, 511-529. (https://doi.org/10.1007/s12541-022-00755-7)

[8] Pollock, J.R.; Moore, M.L.; Hogan, J.S.; Haglin, J.M.; Brinkman, J.C.; Doan, M.K.; Chhabra, A. Orthopaedic group practice size is increasing. Arthrosc. Sports Med. Rehabil. 2021, 3, e1937–e1944. (https://doi.org/10.1016/j.asmr.2021.09.015)

[9] Szpalski, C.; Wetterau, M.; Barr, J.; Warren, S.M. Bone tissue engineering: Current strategies and techniques—Part I: Scaffolds. Tissue Eng. Part B Rev. 2012, 18, 246–257. (https://doi.org/10.1089/ten.teb.2011.0427)

[10] Polo-Corrales, L.; Latorre-Esteves, M.; Ramirez-Vick, J.E. Scaffold design for bone regeneration. J. Nanosci. Nanotechnol. 2014, 14, 15–56. (https://doi.org/10.1166/jnn.2014.9127)

[11] Lee, S.S.; Du, X.; Kim, I.; Ferguson, S.J. Scaffolds for bone-tissue engineering. Matter 2022, 5, 2722–2759. (https://doi.org/10.1016/j.matt.2022.06.003)

[12] Haugen, H.J.; Lyngstadaas, S.P.; Rossi, F.; Perale, G. Bone grafts: Which is the ideal biomaterial? J. Clin. Periodontol. 2019, 46 (Suppl. S21), 92–102. (https://doi.org/10.1111/jcpe.13058)

[13] Qu, H.; Fu, H.; Han, Z.; Sun, Y. Biomaterials for bone tissue engineering scaffolds: A review. RSC Adv. 2019, 9, 26252–26262. (https://doi.org/10.1039/C9RA05214C)

[14] Koons, G.L.; Diba, M.; Mikos, A.G. Materials design for bone–tissue engineering. Nat. Rev. Mater. 2020, 5, 584–603. (https://doi.org/10.1038/s41578-020-0204-2)

[15] Ravoor, J.; Thangavel, M.; Elsen, R.S. Comprehensive review on design and manufacturing of bioscaffolds for bone reconstruction. ACS Appl. Bio Mater. 2021, 4, 8129–8158. (https://doi.org/10.1021/acsabm.1c00949)

doi:10.6342/NTU202502722

[16] Bahraminasab, M.; Janmohammadi, M.; Arab, S.; Talebi, A.; Nooshabadi, V.T.; Koohsarian, P.; Nourbakhsh, M.S. Bone scaffolds: An incorporation of biomaterials, cells, and biofactors. ACS Biomater. Sci. Eng. 2021, 7, 5397–5431. (https://doi.org/10.1021/acsbiomaterials.1c00920)

[17] Collins, M.N.; Ren, G.; Young, K.; Pina, S.; Reis, R.L.; Oliveira, J.M. Scaffold fabrication technologies and structure/function properties in bone tissue engineering. Adv. Funct. Mater. 2021, 31, 2010609. (https://doi.org/10.1002/adfm.202010609)

[18] Szczesny, G.; Kopec, M.; Politis, D.J.; Kowalewski, Z.L.; Łazarski, A.; Szolc, T. A review on biomaterials for orthopaedic surgery and traumatology: From past to present. Materials 2022, 15, 3622. (https://doi.org/10.3390/ma15103622)

[19] Sheikh, Z.; Najeeb, S.; Khurshid, Z.; Verma, V.; Rashid, H.; Glogauer, M. Biodegradable materials for bone repair and tissue engineering applications. Materials 2015, 8, 5744–5794. (https://doi.org/10.3390/ma8095273)

[20] Wei, S.; Ma, J.-X.; Xu, L.; Gu, X.-S.; Ma, X.-L. Biodegradable materials for bone defect repair. Mil. Med. Res. 2020, 7, 54. (https://doi.org/10.1186/s40779-020-00280-6)

[21] Modrák, M.; Trebunová, M.; Balogová, A.F.; Hudák, R.; Živčák, J. Biodegradable materials for tissue engineering: Development, classification and current applications. J. Funct. Biomater. 2023, 14, 159. (https://doi.org/10.3390/jfb14030159)

[22] Chen, H.; Song, G.; Xu, T.; Meng, C.; Zhang, Y.; Xin, T.; Yu, T.; Lin, Y.; Han, B. Biomaterial scaffolds for periodontal tissue engineering. Funct. Biomater., 2024, 15, No. 233. (https://doi.org/10.3390/jfb15080233)

[23] Williams, D. F.; Challenges with the development of biomaterials for sustainable

doi:10.6342/NTU202502722

tissue engineering. Front. Bioeng. Biotechnol., 2019, 7, No. 127. (https://doi.org/10.3389/fbioe.2019.00127)

[24] Donnaloja, F.; Jacchetti, E.; Soncini, M.; Raimondi, M. T. Natural and synthetic polymers for bone scaffolds optimization, Polymers, 2020, 12, No. 905. (https://doi.org/10.3390/polym12040905)

[25] Xu, C.; Liu, Z.; Chen, X.; Gao, Y.; Wang, W.; Zhuang, X.; Zhang, H.; Dong, X. Bone tissue engineering scaffold materials: Fundamentals, advances, and challenges. Chin. Chem. Lett., 2024, 35, No. 109197. (https://doi.org/10.1016/j.cclet.2023.109197)

[26] Di Maioa, E.; Kiran, E. Foaming of polymers with supercritical fluids and perspectives on the current knowledge gaps and challenges, J. Supercrit. Fluids, 2018, 134, 157–166. (https://doi.org/10.1016/j.supflu.2017.11.013)

[27] Sarver, J. A.; Kiran, E. Foaming of polymers with carbon dioxide - The year-in-review-2019, J. Supercrit. Fluids, 2021, 173, No.105166. (https://doi.org/10.1016/j.supflu.2021.105166)

[28] Yu, H.; Liu, H.; Shen, Y.; Ao, Q. Synthetic biodegradable polymer materials in the repair of tumor-associated bone defects. Front. Bioeng. Biotechnol. 2023, 11, 1096525. (https://doi.org/10.3389/fbioe.2023.1096525)

[29] Bernardo, M.P.; da Silva, B.C.R.; Hamouda, A.E.I.; de Toledo, M.A.S.; Schalla, C.; Rütten, S.; Goetzke, R.; Mattoso, L.H.C.; Zenke, M.; Sechi, A. PLA/hydroxyapatite scaffolds exhibit in vitro immunological inertness and promote robust osteogenic differentiation of human mesenchymal stem cells without osteogenic stimuli. Sci. Rep. 2022, 12, 2333. (https://doi.org/10.1038/s41598-022-05207-w)

[30] Zhao, X.; Hu, H.; Wang, X.; Yu, X.; Zhou, W.; Peng, S. Super tough poly(lactic acid) blends: A comprehensive review. RSC Adv. 2020, 10, 13316–13368.

doi:10.6342/NTU202502722

(https://doi.org/10.1039/D0RA01801E)

[31] Nofar, M.; Sacligil, D.; Carreau, P.J.; Kamal, M.R.; Heuzey, M.-C. Poly(lactic acid) blends: Processing, properties and applications. Int. J. Biol. Macromol. 2019, 125, 307–360. (https://doi.org/10.1016/j.ijbiomac.2018.12.115)

[32] Sun, Z.; Wang, L.; Zhou, J.; Fan, X.; Xie, H.; Zhang, H.; Zhang, G.; Shi, X. Influence of polylactide (PLA) stereocomplexation on the microstructure of PLA/PBS blends and the cell morphology of their microcellular foams. Polymers, 2020, 12, No. 2362. (https://doi.org/10.3390/polym12102362)

[33] Su, S.; Kopitzky, R.; Tolga, S.; Kabasci, S. Polylactide (PLA) and its blends with poly(butylene succinate) (PBS): a brief review. Polymers, 2019, 11, No. 1193. (https://doi.org/10.3390/polym11071193)

[34] Zhang, X.; Liu, Q.; Shi, J.; Ye, H.; Zhou, Q. Distinctive tensile properties of the blends of poly(l-lactic acid) (PLLA) and poly(butylene succinate) (PBS). J. Polym. Environ., 2018, 26, 1737-1744. (https://doi.org/10.1007/s10924-017-1064-8)

[35] Ou-Yang, Q.; Guo, B.; Xu, J. Preparation and characterization of poly(butylene succinate)/polylactide blends for fused deposition modeling 3D printing. ACS Omega, 2018, 3, 14309-14317. (http://pubs.acs.org/journal/acsodf)

[36] Yu, P.; Mi, H.-Y.; Huang, A.; Geng, L.-H.; Chen, B.-Y.; Kuang, T.-R.; Mou, W.-J.; Peng, X.-F. Effect of poly(butylenes succinate) on poly(lactic acid) foaming behavior: formation of open cell structure. Ind. Eng. Chem. Res., 2015, 54, 6199−6207. (https://doi.org/10.1021/acs.iecr.5b00477)

[37] Zhao, H.; Liu, H.; Liu, Y.; Yang, Y. Blends of poly(butylene adipate-co-terephthalate) (PBAT) and stereocomplex polylactide with improved rheological and mechanical properties. RSC Adv., 2020, 10, 10482-10490.

doi:10.6342/NTU202502722

(https://doi.org/10.1039/c9ra10827k)

[38] Kang, Y.; Chen, P.; Shi, X.; Zhang, G.; Wang, C. Preparation of open-porous stereocomplex PLA/PBAT scaffolds and correlation between their morphology, mechanical behavior, and cell compatibility. RSC Adv., 2018, 8, 12933-12943. (https://doi.org/10.1039/c8ra01305e)

[39] De Matos Costa, A.R.; Crocitti, A.; de Carvalho, L.H.; Carroccio, S.C.; Cerruti, P.; Santagata, G. Properties of biodegradable films based on poly(butylene succinate) (PBS) and poly(butylene adipate-co-terephthalate) (PBAT) blends. Polymers 2020, 12, 2317. (https://doi.org/10.3390/polym12102317)

[40] Hu, D.; Xue, K.; Liu, Z.; Xu, Z.; Zhao, L. The essential role of PBS on PBAT foaming under supercritical CO_2 toward green engineering. J. CO_2 Util. 2022, 60, 101965. (https://doi.org/10.1016/j.jcou.2022.101965)

[41] Kaliva, M.; Georgopoulou, A.; Dragatogiannis, D.A.; Charitidis, C.A.; Chatzinikolaidou, M.; Vamvakaki, M. Biodegradable chitosan-graft-poly(L-lactide) copolymers for bone tissue engineering. Polymers 2020, 12, 316. (https://doi.org/10.3390/polym12020316)

[42] Dos Santos Silva, A.; Rodrigues, B.V.M.; Oliveira, F.C.; Carvalho, J.O.; de Vasconcellos, L.M.R.; de Araújo, J.C.R.; Marciano, F.R.; Lobo, A.O. Characterization and in vitro and in vivo assessment of poly(butylene adipate-co-terephthalate)/nano-hydroxyapatite composites as scaffolds for bone tissue engineering. J. Polym. Res. 2019, 26, 53. (https://doi.org/10.1007/s10965-019-1726-4)

[43] Santana-Melo, G.F.; Rodrigues, B.V.M.; da Silva, E.; Ricci, R.; Marciano, F.R.; Webster, T.J.; Vasconcellos, L.M.R.; Lobo, A.O. Electrospun ultrathin PBAT/nHAp

doi:10.6342/NTU202502722

fibers influenced the in vitro and in vivo osteogenesis and improved the mechanical properties of neoformed bone. Colloids Surf. B 2017, 155, 544–552. (https://doi.org/10.1016/j.colsurfb.2017.04.030)

[44] Zhang, J.; Li, J.; Jia, G.; Jiang, Y.; Liu, Q.; Yang, X.; Pan, S. Improving osteogenesis of PLGA/HA porous scaffolds based on dual delivery of BMP-2 and IGF-1 via a polydopamine coating. RSC Adv. 2017, 7, 56732–56742. (https://doi.org/10.1039/C7RA12062A)

[45] Khan, M.A.; Hussain, Z.; Liaqat, U.; Liaqat, M.A.; Zahoor, M. Preparation of PBS/PLLA/HAP composites by the solution casting method: Mechanical properties and biocompatibility. Nanomaterials 2020, 10, 1778. (https://doi.org/10.3390/nano10091778)

[46] Gui, X.; Peng, W.; Xu, X.; Su, Z.; Liu, G.; Zhou, Z.; Liu, M.; Li, Z.; Song, G.; Zhou, C.; et al. Synthesis and application of nanometer hydroxyapatite in biomedicine. Nanotechnol. Rev. 2022, 11, 2154–2168. (https://doi.org/10.1515/ntrev-2022-0127)

[47] Wang, W.; Zhang, B.; Li, M.; Li, J.; Zhang, C.; Han, Y.; Wang, L.; Wang, K.; Zhou, C.; Liu, L.; et al. 3D printing of PLA/n-HA composite scaffolds with customized mechanical properties and biological functions for bone tissue engineering. Compos. B Eng. 2021, 224, 109192. (https://doi.org/10.1016/j.compositesb.2021.109192)

[48] Yan, D.; Wang, Z.; Guo, Z.; Ma, Y.; Wang, C.; Tan, H.; Zhang, Y. Study on the properties of PLA/PBAT composite modified by nanohydroxyapatite. J. Mater. Res. Technol. 2020, 9, 11895–11904. (https://doi.org/10.1016/j.jmrt.2020.08.051)

[49] Kiran, E. Supercritical fluids and polymers -The year in review - 2014, J. Supercrit. Fluids, 2016, 110, 126–153. (http://dx.doi.org/10.1016/j.supflu.2015.11.011)

[50] Zhou, Y.; Tian, Y.; Peng, X. Applications and challenges of supercritical foaming

doi:10.6342/NTU202502722

technology, Polymers 2023, 15, No. 402. (https://doi.org/10.3390/polym15020402)

[51] Peng, K.; Mubarak, S.; Diao, X.; Cai, Z.; Zhang, C.; Wang, J.; Wu, L. Progress in the preparation, properties, and applications of PLA and Its composite microporous materials by supercritical CO2: a review from 2020 to 2022, Polymers, 2022, 14, No. 4320. (https://doi.org/ 10.3390/polym14204320)

[52] Li, B.; Zhao, G.; Wang, G.; Zhang, L.; Gong, J.; Shi, Z. Super high-expansion poly(lactic acid) foams with excellent oil-adsorption and thermal-insulation properties fabricated by supercritical CO2 foaming, Adv. Sustainable Syst., 2021, No. 2000295. (https://doi.org/10.1002/adsu.202000295)

[53] Yang, Y.; Li, X.; Zhang, Q.; Xia, C.; Chen, C.; Chen, X.; Yu, P. Foaming of poly(lactic acid) with supercritical CO2: the combined effect of crystallinity and crystalline morphology on cellular structure. J. Supercrit. Fluids, 2019, 145, 122–132. (https://doi.org/10.1016/j.supflu.2018.12.006)

[54] Chen, J.; Yang, L.; Mai, Q.; Li, M.; Wu, L.; Kong, P. Foaming behavior of poly(lactic acid) with different D-isomer content based on supercritical CO2-induced crystallization, J. Cell. Plast., 2021, 57, 675–694. (https://doi.org/10.1177/0021955X20950242)

[55] Huang, J.-N.; Jing, X.; Geng, L.-H.; Chen, B.-Y.; Mi, H.-Y.; Peng, X.-F. A novel multiple soaking temperature (MST) method to prepare polylactic acid foams with bi-modal open-pore structure and their potential in tissue engineering applications. J. Supercrit. Fluids, 2015, 103, 28–37. (http://dx.doi.org/10.1016/j.supflu.2015.04.019)

[56] Li, B.; Zhao, G.; Wang, G.; Zhang, L.; Gong, J.; Shi, Z. Biodegradable PLA/PBS open-cell foam fabricated by supercritical CO2 foaming for selective oil-adsorption,

doi:10.6342/NTU202502722

Sep. Purif. Technol., 2021, 257, No. 117949. (https://doi.org/10.1016/j.seppur.2020.117949)

[57] Wang, S.; Yang, W.; Li, X.; Hu, Z.; Wang, B.; Li, M.; Dong, W. Preparation of high-expansion open-cell polylactic acid foam with superior oil-water separation performance, Int. J. Biol. Macromol., 2021, 193, 1059–1067. (https://doi.org/10.1016/j.ijbiomac.2021.11.033)

[58] Wang, Z.; Zhao, J.; Wang, G.; Xu, Z.; Zhang, A.; Dong, G.; Zhao, G. Lightweight, low-shrinkage and high elastic poly(butylene adipate-co-terephthalate) foams achieved by microcellular foaming using N2 & CO2 as co-blowing agents, J. CO2 Util., 2022, 64, No. 102149. (https://doi.org/10.1016/j.jcou.2022.102149)

[59] Salerno, A.; Di Maio, E.; Iannace, S.; Netti, P. A. Solid-state supercritical CO2 foaming of PCL and PCL-HA nano-composite: Effect of composition, thermal history and foaming process on foam pore structure, J. Supercrit. Fluids, 2011, 58, 158-167. (https://doi.org/10.1016/j.supflu.2011.05.009)

[60] Chen, C.-X.; Peng, H.-H.; Guan, Y.-X.; Yao, S.-J. Morphological study on the pore growth profile of poly(ε-caprolactone) bi-modal porous foams using a modified supercritical CO2 foaming process, J. Supercrit. Fluids, 2019, 143, 72-81. (https://doi.org/10.1016/j.supflu.2018.07.029)

[61] Ju, J.; Gu, Z.; Liu, X.; Zhang, S.; Peng, X.; Kuang, T. Fabrication of bimodal open-porous poly (butylene succinate)/cellulose nanocrystals composite scaffolds for tissue engineering application, Int. J. Biol. Macromol., 2020, 147, 1164-1173. (https://doi.org/10.1016/j.ijbiomac.2019.10.085)

[62] Park, J.-W.; Hwang, J.-U.; Back, J.-H.; Jang, S.-W.; Kim, H.-J.; Kim, P.-S.; Shin, S.; Kim, T. High strength PLGA/hydroxyapatite composites with tunable surface

doi:10.6342/NTU202502722

structure using PLGA direct grafting method for orthopedic implants. Compos. B Eng. 2019, 178, 107449. (https://doi.org/10.1016/j.compositesb.2019.107449)

[63] Lowe, B.; Hardy, J.G.; Walsh, L.J. Optimizing nanohydroxyapatite nanocomposites for bone tissue engineering. ACS Omega 2020, 5, 1–9. (https://doi.org/10.1021/acsomega.9b02917)

[64] Yin, D.; Mi, J.; Zhou, H.; Wang, X.; Fu, H. Microcellular foaming behaviors of chain extended poly (butylene succinate)/polyhedral oligomeric silsesquioxane composite induced by isothermal crystallization. Polym. Degrad. Stab., 2019, 167, No. 228e240. (https://doi.org/10.1016/j.polymdegradstab.2019.07.010)

[65] Sato, Y.; Takikawa, T.; Sorakubo, A.; Takishima, S.; Masuoka, H.; Imaizumi, M. Solubility and diffusion coefficient of carbon dioxide in biodegradable polymers. Ind. Eng. Chem. Res. 2000, 39, 4813-4819. (https://doi.org/ 10.1021/ie0001220)

[66] Goncalves, L. F. F. F.; Reis, R. L.; Fernandes, E. M. Forefront research of foaming strategies on biodegradable polymers and their composites by thermal or melt-based processing technologies: advances and perspectives. Polymers, 2024, 16, No. 1286. (https://doi.org/10.3390/polym16091286)

[67] Velasco, M.A.; Narváez-Tovar, C.A.; Garzón-Alvarado, D.A. Design, materials, and mechanobiology of biodegradable scaffolds for bone tissue engineering. Biomed Res. Int. 2015, 729076. (https://doi.org/10.1155/2015/729076)

[68] Shelton, T.J.; Delman, C.; McNary, S.; Taylor, J.R.; Marder, R.A. Aging decreases the ultimate tensile strength of bone–patellar tendon–bone allografts. Arthroscopy 2021, 37, 2173–2180. (https://doi.org/10.1016/j.arthro.2021.02.041)

[69] Rodrigues, S.C.S.; de Mesquita, F.A.S.; de Carvalho, L.H.; Alves, T.S.; Folkersma, R.; Araújo, R.S.d.R.M.; Oliveira, A.D.; Barbosa, R. Preparation and characterization

doi:10.6342/NTU202502722

of polymeric films based on PLA, PBAT and corn starch and babassu mesocarp starch by flat extrusion. Mater. Res. Express 2021, 8, 035305. (https://doi.org/10.1088/2053-1591/abeaca)

[70] Gheisari, H.; Karamian, E.; Abdellahi, M. A novel hydroxyapatite–Hardystonite nanocomposite ceramic. Ceram. Int. 2015, 41, 5967–5975. (https://doi.org/10.1016/j.ceramint.2014.12.125)

[71] Rasheed, M.; Jawaid, M.; Parveez, B.; Bhat, A.H.; Alamery, S. Morphology, structural, thermal, and tensile properties of bamboo microcrystalline cellulose/poly(lactic acid)/poly(butylene succinate) composites. Polymers 2021, 13, 465. (https://doi.org/10.3390/polym13030465)

[72] Solechan, S.; Suprihanto, A.; Widyanto, S.A.; Triyono, J.; Fitriyana, D.F.; Siregar, J.P.; Cionita, T. Characterization of PLA/PCL/Nano-Hydroxyapatite (nHA) Biocomposites Prepared via Cold Isostatic Pressing. Polymers 2023, 15, 559. (https://doi.org/10.3390/polym15030559)

[73] Qiu, T.Y.; Song, M.; Zhao, L.G. Testing, Characterization and Modelling of Mechanical Behaviour of Poly(Lactic-Acid) and Poly(Butylene Succinate) Blends. Mech. Adv. Mater. Mod. Process. 2016, 2, 7. (https://doi.org/10.1186/s40759-016-0014-9)

[74] Qahtani, M.; Wu, F.; Misra, M.; Gregori, S.; Mielewski, D.F.; Mohanty, A.K. Experimental Design of Sustainable 3D-Printed Poly(Lactic Acid)/Biobased Poly(Butylene Succinate) Blends via Fused Deposition Modeling. ACS Sustain. Chem. Eng. 2019, 7, 14460–14470. (https://doi.org/10.1021/acssuschemeng.9b01830)

[75] Righetti, M.C.; Di Lorenzo, M.L.; Cinelli, P.; Gazzano, M. Temperature Dependence

doi:10.6342/NTU202502722

of the Rigid Amorphous Fraction of Poly(Butylene Succinate). RSC Adv. 2021, 11, 25731–25737. (https://doi.org/10.1039/D1RA03775G)

[76] Bai, J.; Pei, H.; Zhou, X.; Xie, X. Reactive Compatibilization and Properties of Low-Cost and High-Performance PBAT/Thermoplastic Starch Blends. Eur. Polym. J. 2021, 143, 110198. (https://doi.org/10.1016/j.eurpolymj.2020.110198)

[77] Zhao, X.; Zhang, D.; Yu, S.; Zhou, H.; Peng, S. Recent Advances in Compatibility and Toughness of Poly(Lactic Acid)/Poly(Butylene Succinate) Blends. e-Polymers 2021, 21, 793–810. (https://doi.org/10.1515/epoly-2021-0079)

[78] Wang, B.; Jin, Y.; Kang, K.; Yang, N.; Weng, Y.; Huang, Z.; Men, S. Investigation on Compatibility of PLA/PBAT Blends Modified by Epoxy-Terminated Branched Polymers through Chemical Micro-Crosslinking. e-Polymers 2020, 20, 39–54. (https://doi.org/10.1515/epoly-2020-0005)

[79] Zhou, Y.; Qiu, S.; Waterhouse, G.I.N.; Zhang, K.; Xu, J. Enhancing the Properties of PBAT/PLA Composites with Novel Phosphorus-Based Ionic Liquid Compatibilizers. Mater. Today Commun. 2021, 27, 102407. (https://doi.org/10.1016/j.mtcomm.2021.102407)

[80] De Luna, M.S.; Filippone, G. Effects of Nanoparticles on the Morphology of Immiscible Polymer Blends—Challenges and Opportunities. Eur. Polym. J. 2016, 79, 198–218. (https://doi.org/10.1016/j.eurpolymj.2016.04.003)

[81] Zhao, Q.; Wang, B.; Qin, C.; Li, Q.; Liu, C.; Shen, C.; Wang, Y. Nonisothermal Melt and Cold Crystallization Behaviors of Biodegradable Poly(Lactic Acid)/$Ti_3C_2T_x$ MXene Nanocomposites. J. Therm. Anal. Calorim. 2022, 147, 2239–2251. (https://doi.org/10.1177/0021998313502064)

[82] Mata-Padilla, J.M.; Avila-Orta, C.A.; Almendarez-Camarillo, A.; Martinez-Colunga,

doi:10.6342/NTU202502722

J.G.; Hernandez-Hernandez, E.; Cruz-Delgado, V.J.; Gonzalez-Morones, P.; Solis-Rosales, S.G.; Gonzalez-Calderon, J.A. Non-Isothermal Crystallization Behavior of Isotactic Polypropylene/Copper Nanocomposites. J. Therm. Anal. Calorim. 2021, 143, 2919–2932. (https://doi.org/10.1007/s10973-020-09512-2)

[83] Gao, H.; Qiang, T. Fracture Surface Morphology and Impact Strength of Cellulose/PLA Composites. Materials 2017, 10, 624. (https://doi.org/10.3390/ma10060624)

[84] Pivsa-Art, W.; Pivsa-Art, S. Effect of Talc on Mechanical Characteristics and Fracture Toughness of Poly(Lactic Acid)/Poly(Butylene Succinate) Blend. J. Polym. Environ. 2019, 27, 1821–1827. (https://doi.org/10.1007/s10924-019-01478-z)

[85] Mao, H.-I.; Hsu, T.-S.; Chen, C.-W.; Huang, K.-W.; Rwei, S.-P. Synthesis and Characteristics of Poly(Ethylene Terephthalate) with EO-PO-EO Triblock Copolymers: A Thermal and Mechanical Property Study. J. Appl. Polym. Sci. 2022, 139, e51065. (https://doi.org/10.1002/app.51605)

[86] Ecker, J.V.; Haider, A.; Burzic, I.; Huber, A.; Eder, G.; Hild, S. Mechanical Properties and Water Absorption Behaviour of PLA and PLA/Wood Composites Prepared by 3D Printing and Injection Moulding. Rapid Prototyp. J. 2019, 25, 672–678. (https://doi.org/10.1108/RPJ-03-2018-0064)

[87] Avci, A.; Eker, A.A.; Bodur, M.S.; Candan, Z. Water Absorption Characterization of Boron Compounds-Reinforced PLA/Flax Fiber Sustainable Composite. Int. J. Biol. Macromol. 2023, 233, 123546. (https://doi.org/10.1016/j.ijbiomac.2023.123546)

[88] Tammaro, D.; Lombardi, L.; Maffettone, P. L. Bimodal cell distributions in foaming of olefin block copolymers using high-throughput experimentation. Chem. Eng. Sci., 2025, 304, No. 121067. (http://creativecommons.org/licenses/by/4.0/)

doi:10.6342/NTU202502722

[89] Xu, L. Q.; Huang, H.-X. Formation mechanism and tuning for bi-modal cell structure in polystyrene foams by synergistic effect of temperature rising and depressurization with supercritical CO2. J. Supercrit. Fluids, 2016, 109, 177-185. (https://dx.doi.org/10.1016/j.supflu.2015.07.020)

[90] Liao, X., Nawaby, A. V., Whitfield, P. S., Carbon dioxide-induced crystallization in poly(L-lactic acid) and its effect on foam morphology. Polm. Int., 2010, 59, 1709-1718. (https://doi.org/10.1002/pi.2901)

[91] Zhou, H.; Hu, D.; Zhu, M.; Xue, K.; Wei, X.; Park, C. B.; Wang, X.; Zhao, L., Review on poly (butylene succinate) foam: Modification, foaming behavior and applications. SM&T, 2023, 38, No. e00720. (https://doi.org/10.1016/j.susmat.2023.e00720)

[92] Li, G.; Li., H.; Turng, L. S.; Gong, S.; Zhang, C.; Measurement of gas solubility and diffusivity in polylactide. Fluid Phase Equilib., 2006, 246, 158-166. (https://doi.org/10.1016/j.fluid.2006.05.030)

[93] Lin, S.; Yang, J.; Yan, J.; Zhao, Y.; Yang, B. Sorption and diffusion of supercritical carbon dioxide in a biodegradable polymer. J. Macromol. Sci. Phys., 2010, 49, 286-300. (https://doi.org/10.1080/01495930903352308)

[94] Li, B.; Zhao, G.; Wang, G.; Zhang. L.; Gong, J. Fabrication of high-expansion PLA foams based on pre-isothermal cold crystallization and supercritical CO2 foaming. Polym. Degrad. Stab., 2018, 156, 75-88. (https://doi.org/10.1016/j.polymdegradstab.2018.08.009)

[95] Zhou, H.; Song, J.; Ding, X.; Qu, Z.; Wang, X.; Mi, J.; Wang, J. Cellular morphology evolution of chain extended poly(butylene succinate)/organic montmorillonite nanocomposite foam. J. Appl. Polym. Sci. 2019, No. 47107.

doi:10.6342/NTU202502722

(https://doi.org/10.1002/APP.47107)

[96] Jacobs, L. J. M.; Kemmere, M. F.; Keurentjes, J. T. F. Sustainable polymer foaming using high pressure carbon dioxide: a review on fundamentals, processes and applications. Green Chem., 2008, 10, 731–738. (https://doi.org/ 0.1039/b801895b)

[97] Yang, J.; Jiang, T.; Liu, B.; Zhang, C.; Zeng, X.; He, L.; Gong, W. Experimental and numerical analysis of bubble nucleation in foaming polymer. Mater. Des. 2021, 203, No. 109577. (https://doi.org/10.1016/j.matdes.2021.109577)

[98] Mukasheva, F.; Adilova, L.; Dyussenbinov, A.; Yernaimanova, B.; Abilev, M.; Akilbekova, D. Optimizing scaffold pore size for tissue engineering: insights across various tissue types. Front. Bioeng. Biotechnol. 2024, 12, No. 1444986. (https://doi.org/ 10.3389/fbioe.2024.1444986)

[99] Abbasi, N.; Stephen Hamlet, S.; Love, R. M.; Nguyen, N.-T. Porous scaffolds for bone regeneration. J. Sci.: Adv. Mater. Devices, 2020, 5, 1-9. (https://doi.org/10.1016/j.jsamd.2020.01.007)

[100] Huang, L.; Wang A.; · Xu R.; Lei C. PBS melt strength improving for supercritical CO2 Foaming molding by physical adsorption and crystallization. Polym. Bull. 2024, 81, 11629–11643. (https://doi.org/10.1007/s00289-024-05251-8)

[101] Hernandez, J. L.; Woodrow, K. A. Medical applications of porous biomaterials: features of porosity and tissue-specific implications for biocompatibility. Adv Healthc Mater., 2022, 11, No. e2102087. (https://doi.org/10.1002/adhm.202102087)

doi:10.6342/NTU202502722

附錄

1. **Bio-Based PLA/PBS/PBAT Ternary Blends with Added Nanohydroxyapatite: A Thermal, Physical, and Mechanical Study.** Polymers 2023, 15, 4585. (https://doi.org/10.3390/polym15234585)

2. **Foaming of Bio-Based PLA/PBS/PBAT Ternary Blends with Added Nanohydroxyapatite Using Supercritical CO2: Effect of Operating Strategies on Cell Structure.** Molecules 2025, 30, 2056. (https://doi.org/10.3390/molecules30092056)

doi:10.6342/NTU202502722

polymers

MDPI

Article

Bio-Based PLA/PBS/PBAT Ternary Blends with Added Nanohydroxyapatite: A Thermal, Physical, and Mechanical Study

Pei-Hua Chen [1,2], Chin-Wen Chen [3,*], Hsu-I Mao [3], Chi-An Dai [4], Chie-Shaan Su [5], Jung-Chin Tsai [6] and Feng-Huei Lin [1,*]

[1] Department of Biomedical Engineering, National Taiwan University, Taipei 106319, Taiwan; d10528004@ntu.edu.tw
[2] Department of Orthopedics, Shuang Ho Hospital, Taipei Medical University, New Taipei City 235041, Taiwan
[3] Department of Molecular Science and Engineering, Institute of Organic and Polymeric Materials, Research and Development Center of Smart Textile Technology, National Taipei University of Technology, Taipei 106344, Taiwan; eeric0212@hotmail.com
[4] Department of Chemical Engineering, Institute of Polymer Science and Engineering, National Taiwan University, Taipei 106319, Taiwan; polymer@ntu.edu.tw
[5] Department of Chemical Engineering and Biotechnology, National Taipei University of Technology, Taipei 106344, Taiwan; cssu@ntut.edu.tw
[6] Department of Chemical Engineering, Ming Chi University of Technology, New Taipei City 243303, Taiwan; jctsai@mail.mcut.edu.tw
* Correspondence: cwchen@ntut.edu.tw (C.-W.C.); double@ntu.edu.tw (F.-H.L.)

Abstract: The physical and mechanical properties of novel bio-based polymer blends of polylactic acid (PLA), poly(butylene succinate) (PBS), and poly (butylene adipate-co-terephthalate) (PBAT) with various added amounts of nanohydroxyapatite (nHA) were investigated in this study. The formulations of PLA/PBS/PBAT/nHA blends were divided into two series, A and B, containing 70 or 80 wt% PLA, respectively. Samples of four specimens per series were prepared using a twin-screw extruder, and different amounts of nHA were added to meet the regeneration needs of bone graft materials. FTIR and XRD analyses were employed to identify the presence of each polymer and nHA in the various blends. The crystallization behavior of these blends was examined using DSC. Tensile and impact strength tests were performed on all samples to screen feasible formulations of polymer blends for bone graft material applications. Surface morphology analyses were conducted using SEM, and the dispersion of nHA particles in the blends was further tested using TEM. The added nHA also served as a nucleating agent aimed at improving the crystallinity and mechanical properties of the blends. Through the above analyses, the physical and mechanical properties of the polymer blends are reported and the most promising bone graft material formulations are suggested. All blends were tested for thermal degradation analysis using TGA and thermal stability was confirmed. The water absorption experiments carried out in this study showed that the addition of nHA could improve the hydrophilicity of the blends.

Keywords: PLA; PBS; PBAT; nHA; polymer blends; mechanical strength; physical properties

check for updates

Citation: Chen, P.-H.; Chen, C.-W.; Mao, H.-I.; Dai, C.-A.; Su, C.-S.; Tsai, J.-C.; Lin, F.-H. Bio-Based PLA/PBS/PBAT Ternary Blends with Added Nanohydroxyapatite: A Thermal, Physical, and Mechanical Study. *Polymers* **2023**, *15*, 4585. https://doi.org/10.3390/polym15234585

Academic Editor: Roberto Pantani

Received: 22 September 2023
Revised: 22 November 2023
Accepted: 28 November 2023
Published: 30 November 2023

Copyright: © 2023 by the authors. Licensee MDPI, Basel, Switzerland. This article is an open access article distributed under the terms and conditions of the Creative Commons Attribution (CC BY) license (https://creativecommons.org/licenses/by/4.0/).

1. Introduction

In recent years, the research and development of biomaterials have developed rapidly to meet the needs of tissue engineering to improve human life. The interface between synthetic biology and biomaterial design creates promising challenges in health, biotechnology, and sustainability [1]. Proper design of biomaterials must cover both their mechanical properties and biological activity. Future biomaterials can maintain organ transport and self-healing functions, biocompatibility, biodegradability, bioactivity, and tissue regeneration activity [1,2]. Biomaterials are generally classified as natural, metal and alloy-based,

doi:10.6342/NTU202502722

ceramic-based, polymer-based, or composite materials for tissue engineering scaffolds, each of which has a variety of applications [3,4]. It has been reported that surgeries to treat bone defects in orthopedics has a growing rate [5], and the development of biomaterials for orthopedic implants has received much attention [6–10]. The design and fabrication techniques for bone tissue engineering have been reported in the review literature, addressing engineering processes and functional properties [11–14]. Although most bone implants are metal-based, polymers and their composites are projected to become more suitable in the future [15]. In recent reviews, next-generation bone tissue bio-based materials, especially biodegradable polymers and nanotechnology, have received much attention [16–18].

Polylactic acid (PLA) is the most commonly used semi-crystalline bio-based polymer approved by the U.S. Food and Drug Administration (FDA) for its desired biocompatibility and biodegradability [19]. In order to improve some of its limitations in terms of mechanical properties, toughness, hydrophilicity, and cell affinity, composites of PLA with other polymers or inorganic additives have been studied in the literature. For example, hydroxyapatite (HA) has been added to PLA to study the in vitro osteogenic differentiation of human mesenchymal stem cells [20]. According to previous reports [21,22], the current improvement of tough PLA was achieved through polymer blending, copolymerization, plasticization, or composite modifications. Blending PLA with other elastomeric polymers is relatively easy and often considered to be the most effective method. PLA with biodegradable polymers such as polycaprolactone (PCL), poly(butylene succinate) (PBS), poly(butylene succinate-co-adipate) (PBSA), and poly(butylene adipate-co-terephthalate) (PBAT) have been discussed. Recent literature has reported the mechanical and physical properties of blends of PBS and PBAT with various compositions, including behavior after supercritical CO_2 foaming [23,24]. The mechanical and physical properties of PLA/PBS or PLA/PBAT blends with proper compositions have been investigated in previous reports, demonstrating their morphology, mechanical properties, and potential applications as scaffolds in tissue engineering [25–31]. Biomaterials for tissue engineering preferably contained bioactive components such as chitosan (a natural polysaccharide) or HA (the main component of human bone tissue) in structured scaffolds to facilitate the regenerative process. The fabrications of PLA-based scaffolds with other biodegradable polymers and bioactive materials have been shown in the literature [32–38]. It has been reported that loaded nano-HA (nHA) particles could promote cell proliferation and mimic the structure of the bone extracellular matrix [20,35–39].

To the best of our knowledge, most literature reports have presented the properties and applications of biodegradable binary polymer blends (for example, PLA/PBS or PLA/PBAT) [28,29,31] or a single polymer with nHA particles added [36,40,41]. Although some studies on ternary systems have been carried out [38,40–42], more experimental measurements are still needed. The aim of this study was to explore the properties of novel polymer blends containing three biodegradable polymers (PLA, PBS and PBAT) with inorganic nHA added. The main component of the blends was PLA, which is suitable for bone graft applications due to its good mechanical strength. The elongation and toughness limits of PLA can be improved by blending with ductile PBS and PBAT. Biodegradable PBS also showed good cell viability [38]. PBAT has a strong but underexploited potential for bone growth in vivo, and the studies on including nHA in PBAT are still limited [35,36]. Therefore, this study proposes a novel bone graft biomaterial, a PLA/PBS/PBAT/nHA composite, produced using a twin-screw extruder. No organic solvent was used in this study to avoid any safety concerns as implant biomaterials. The mechanical and physical properties of various formulations of this blend were measured and promising blends for further bone graft applications are illustrated.

2. Materials and Methods

2.1. Materials

Polylactic acid (PLA, Ingeo 4032D) was purchased from NaturalWorks LLC, Minnetonka, MN, USA. It is semi-crystalline, with an average D-lactide content of 1.4 wt%.

doi:10.6342/NTU202502722

Poly(butylene succinate) (Bio PBS, FZ 91), a semi-crystalline polyester, was purchased from PTT MCC Biochem Co. Ltd., Bangkok, Thailand. Poly(butylene adipate-co-terephthalate) (PBAT, ecoflex F blend C1200) was purchased from BASF SE, Ludwigshafen, Deutschland. The physical and mechanical properties of these polymers are listed in Table 1. Nano-hydroxyapatite (nHA, CAS registry number 12167-74-7) was purchased from Sigma-Aldrich, UNI-ONWARD Corp., Taiwan, with purity greater than 97 wt%, mean particle size of 72–80 nm, molecular weight of 502.3, and melting temperature of about 1100 °C.

Table 1. Physical and mechanical properties of polymers used in this study [a].

Physical Properties	PLA	PBS	PBAT
Density (g/cm^3)	1.24	1.26	1.25–1.27
Melt flow index (g/10 min, at 190 °C, 2.16 kg)	7	5	2.7–4.9
Melting temperature, T_m (°C)	155–170	115	110–120
Tensile yield strength (MPa)	60	39	36
Tensile modulus (GPa)	3.5	0.58	–
Tensile elongation (%)	6.0	350	560

[a]: according to the suppliers.

2.2. Preparation of Composite Blends

PLA, PBS, and PBAT polymers were first dried in a vacuum oven at 80 °C for 6 h before compounding. These blends were prepared using a twin-screw extruder (Process 11, Thermo Fisher Scientific, Waltham, MA, USA). The extruder was equipped with a volumetric feeder and a strand pelletizer for blending the polymers. The diameter of the screw extruder is 11 mm, with an L/D ratio of 40. Polymers were fed into the hopper of the extruder for the compounding process. The extruder has six zones, from feed to die, where the extrusion temperatures were controlled independently. The feed rate of the polymer pellets was 1 kg h^{-1}, and the screw speed was 50 rpm. The temperature settings for the feed and mixing zones were adjusted to be 200–210–220–225–225–220 °C. After blending, a water bath was used to cool the extruded products. These products were then granulated and dried for a sufficient time before mechanical property testing. Plate specimens with a thickness of 1.2 ± 0.2 mm were made by compression molding at 200 °C for 5 min, followed by cooling to room temperature. The specimens were packed in plastic bags and stored in cool surroundings before tests. The extruded products for polymers with added nHA were prepared with the same procedure. Samples with various formulations were also used for thermal, chemical composition, morphology, and water absorption analyses.

Table 2 lists the formulations of PLA-based polymer blends in this study. The specimen code PLA60 represented a polymer blend containing 60 wt% PLA and two other polymers (25 wt% PBS and 15 wt% PBAT), without the addition of nHA. Sample series A and B listed in Table 2 included specimen codes with various amounts of nHA added. For example, specimen A0 listed in Table 2 represented a blend containing 70 wt% PLA, 20 wt% PBS, 10 wt% PBAT, and no added nHA. Specimens A3, A5, and A7 in sample series A had the same PLA/PBS/PBAT composition as specimen A0, but with the addition of 3, 5, and 7 wt% nHA, respectively. Sample series B contained 80 wt% PLA, 15 wt% PBS, 5 wt% PBAT, with 0, 3, 5, and 7 wt% nHA added to specimens B0, B3, B5, and B7, respectively. It has been pointed out that nanocomposites comprising nHA favored the biocompatibility of bone formation [10,36–39,43,44]. The average particle size of nHA used in this study was within the range of nHA particle sizes reported in the literature [44].

doi:10.6342/NTU202502722

Table 2. Formulations of PLA/PBS/PBAT/nHA blends in this study.

Specimen Code	PLA (wt%)	PBS (wt%)	PBAT (wt%)	nHA (wt%)
		Sample with 60 wt% PLA		
PLA60	60	25	15	0
		Sample series A		
A0	70	20	10	0
A3	70	20	10	3
A5	70	20	10	5
A7	70	20	10	7
		Sample series B		
B0	80	15	5	0
B3	80	15	5	3
B5	80	15	5	5
B7	80	15	5	7

2.3. Analysis and Testing

2.3.1. Fourier-Transform Infrared Spectroscopy (FTIR)

Fourier-transform infrared spectroscopy (FTIR, Thermo Fisher Scientific Summit LITE Spectrometer, Madison, WI, USA) using the ATR technique was employed for analyzing the chemical structures of the polymer blends. The wavenumber in the tests ranged from 4000 to 500 cm^{-1}. The resolution was 4 cm^{-1}, and the number of scans was 32.

2.3.2. X-ray Diffraction Analysis

The intensity of crystallinity of the polymer blends was analyzed using an X-ray diffractometer (XRD, Rigaku, Tokyo, Japan) with Cu-K_α radiation (λ = 1.54 Å) operated at 40 kV and 15 mA. The XRD data were collected in the 2θ angle range from 5 to 40°, with a scanning rate at 10° min^{-1}.

2.3.3. Differential Scanning Calorimeter Measurements

The thermal and crystallization behavior of various polymer blends was analyzed using differential scanning calorimetry (DSC, Hitachi High-Tech Science DSC-7000, Tokyo, Japan) under a nitrogen atmosphere. Each sample of 4–6 mg was heated at a rate of 10 °C min^{-1} from 30 to 200 °C and held at 200 °C for 5 min in the first heating process to remove any thermal history. The sample was cooled to −50 °C at a rate of 10 °C min^{-1} and kept at −50 °C for 5 min. In the second heating process, the sample was heated from −50 to 200 °C at a rate of 10 °C min^{-1}. The glass transition temperature, cold crystallization temperature, melting temperature, enthalpy of cold crystallization, and enthalpy of melting were recorded for each sample.

DSC (Hitachi High-Tech Science DSC-7000, Tokyo, Japan) was also employed to evaluate the nonisothermal crystallization behavior of various polymer blends. The prepared samples were kept in aluminum pans under nitrogen atmosphere. The samples were first heated from 30 to 200 °C at 10 °C min^{-1} and then maintained at 200 °C for 5 min to remove any thermal history. Next, the samples were cooled to 50 °C at various rates of 2.5, 5, 7.5, and 10 °C min^{-1}. Finally, heat flow traces were recorded for analysis.

2.3.4. Mechanical Testing

The tensile and impact strength for various polymer blends were measured in this study. A universal material testing machine (Cometech QC-508M2F equipment, Taichung, Taiwan) was used. The tensile tests were conducted at a tensile rate of 50 mm min^{-1} using dumbbell specimens (ASTM D638 Type IV, length: 33 mm, width: 6 mm, thickness: 3 mm, the gauge length being 50 mm). The impact tests (ASTM D412; the degree between pendulum and sample was set at 150°) were performed using a Ceast pendulum impact tester (Model Resil 50B) and a Ceast notch cutting machine. The Izod method was employed. A 2.75 J hammer was sufficient to break all specimens tested for impact strength. At least

doi:10.6342/NTU202502722

five repeated tests were conducted for tensile and impact strength measurements. The averaged values and standard deviations for these mechanical properties were recorded.

2.3.5. Surface Morphology

A scanning electron microscope (SEM, TESCAN VEGA 3 SBH, Brno, Czech Republic) was used to observe the surface morphology and the dispersion of nHA in the PLA/PBS/PBAT/nHA blends. The SEM was operated at an acceleration voltage of 20 kV and a magnification of 3000×. All samples were dried under vacuum and sputter-coated with gold before SEM experiments. The chemical composition of the blends was studied using an energy-dispersive X-ray spectroscope (EDX) attached to the SEM (Nova NanoSEM 230, currently supported by Thermo Fisher, Waltham, MA, USA).

2.3.6. TEM Measurements

A transmission electron microscope (TEM, Hitachi H-7650, Tokyo, Japan) was used to investigate the distribution of nHA in the PLA/PBS/PBAT/nHA blends. Ultrathin sections of sample were prepared using a cryomicrotome with a diamond knife in a dry N_2 atmosphere at −100 °C. The thin film pieces were placed on a copper grid and the TEM analyses were conducted at a low voltage of 70 kV to prevent electron beam damage.

2.3.7. Thermogravimetric Analysis (TGA)

The thermogravimetric analyses for the polymer blends were performed using a thermogravimetric analyzer (TGA, Pyris 6, Perkin Elmer, New Castle, DE, USA) to investigate the thermal stability of the blended samples. Approximately 8 mg of each polymer blend sample was heated from 40 to 600 °C under a nitrogen atmosphere at a heating rate of 10 °C min^{-1}. TGA thermograms were recorded during the heating process and differential thermogravimetric analyses (DTGAs) were also performed.

2.3.8. Water Absorption Measurements

The water absorption for various polymer blends was investigated in this study. The specimens with 20 mm × 10 mm × 2 mm were dried in a vacuum oven at 50 °C for 48 h. The specimens were weighed after the drying process using a balance (Precisa ES 225 SM-DR, Dietikon, Switzerland, readability 0.01 mg). The specimens were then completely immersed in distilled water at 25 °C for 24 h and longer, up to 8 days. After immersing the specimens in distilled water for t days (t = 1, 2, 5, and 8), they were taken out and wiped with filter paper before weighing for water absorption. The water absorption percentages for various samples were determined from weight gain after the water immersion process.

3. Results and Discussion

3.1. Tensile Strength Test Results for PLA/PBS/PBAT Blends

The mechanical strength of polymer blends without the addition of nHA was first tested to screen for acceptable formulations. The tensile strength test results for these polymer blends without nHA are presented in Table 3. It is observed that specimen PLA60 had a maximum tensile stress (tensile strength) of 37.6 ± 1.8 MPa, while specimens A0 and B0 both had maximum tensile stress greater than 45 MPa. The tensile strength of human cortical and cancellous bone, although age-dependent, is 50–150 and 10–100 MPa, respectively [10,45,46]. According to the literature [42], tensile strength higher than 40 MPa meets the need for bone tissue engineering material. It is observed from Table 3 that specimens A0 and B0 almost reached the lower limit of the tensile strength of human cortical bone. The elongations at maximum tensile stress were about 8%. The tensile modulus results for specimens A0 and B0 were also better than that of human cancellous bone [8]. Therefore, PLA-based polymer blends containing 70 or 80 wt% PLA in this study were considered acceptable biomaterials for bone grafts. Specimens in series A and B listed in Table 2 were used for further physical and mechanical property analyses.

doi:10.6342/NTU202502722

Table 3. Tensile test results of PLA/PBS/PBAT blends.

Sample of PLA/PBS/PBAT Blends	Maximum Tensile Stress (MPa)	Elongation at Maximum Tensile Stress (%)	Tensile Modulus (MPa)
PLA60	37.6 ± 1.8	7.0 ± 0.5	584.8 ± 71.9
A0	47.1 ± 2.9	7.9 ± 0.4	642.0 ± 109.1
B0	49.6 ± 1.6	8.0 ± 0.6	686.1 ± 91.3

3.2. FTIR Measurement Results for PLA/PBS/PBAT/nHA Blends

The chemical structures for various PLA/PBS/PBAT/nHA blends were characterized using FTIR spectroscopy. The results for all specimens are presented in Figure 1. The band around the wavenumber of 3000 cm^{-1} represented the symmetric and asymmetric stretching vibration of CH_3 in PLA. The peak at 1750 cm^{-1} showed the stretching of the C=O group of PLA as well as PBS and PBAT. The bands at 1181 cm^{-1} and 1082 cm^{-1} belonged to the peaks of C-O-C. The peak at 1040 cm^{-1} is attributed to C-CH_3 [42,47–50]. The characteristic peaks at 602 cm^{-1} and 570 cm^{-1} represented the characteristic peaks of $PO_3{}^{-4}$ in nHA [42,48,50].

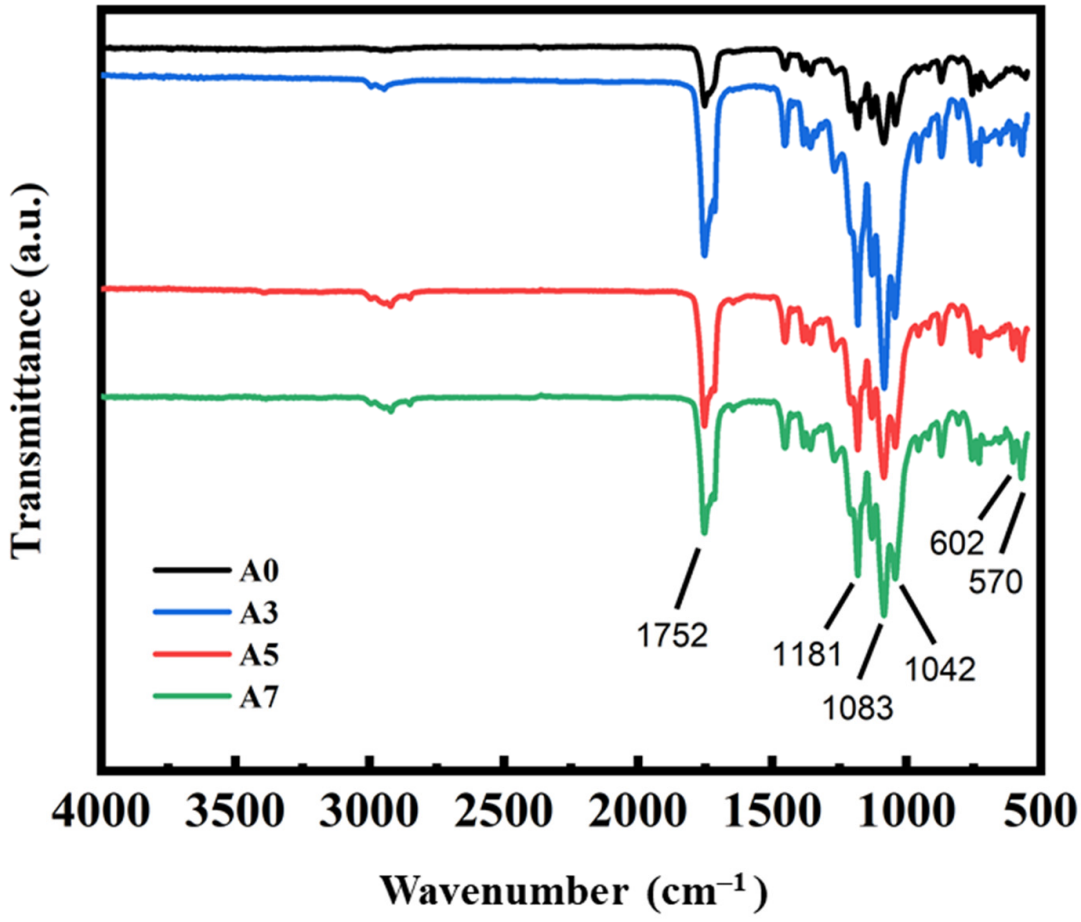

(a)

Figure 1. *Cont.*

doi:10.6342/NTU202502722

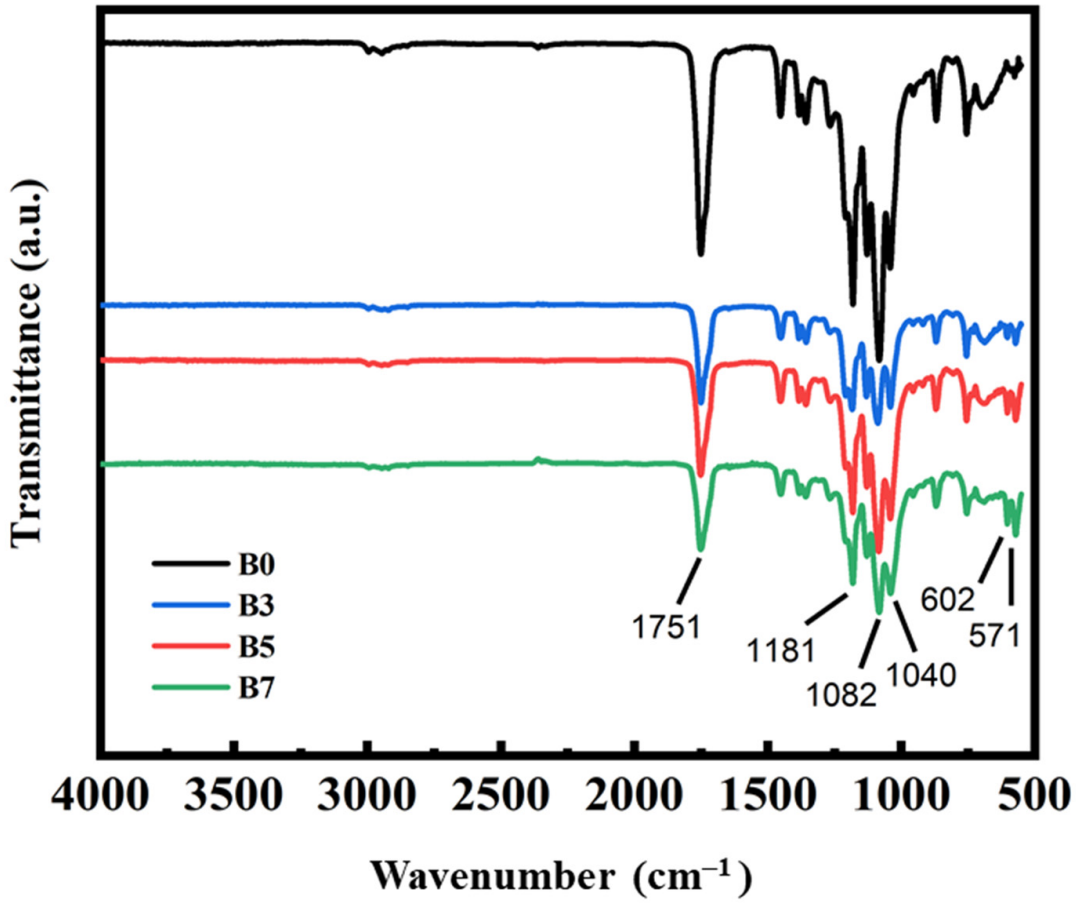

(**b**)

Figure 1. FTIR measurement results for polymer blends: (**a**) sample series A and (**b**) sample series B, with various amounts of nHA added.

It was observed that no nHA peaks were present in specimens A0 and B0, to which no nHA particles were added during the preparation of the polymer blends. The characteristic peaks of nHA in the FTIR spectra for other specimens in Figure 1a,b clearly indicated the existence of nHA in the blends.

3.3. XRD Measurement Results for PLA/PBS/PBAT/nHA Blends

XRD analysis was performed to further confirm the presence of nHA in the PLA/PBS/PBAT/nHA polymer blends and to identify the crystalline species in the polymer blends. The results are presented in Figure 2a,b for sample series A and B with various amounts of nHA added. The diffraction peaks between 2 θ at 15° and 20° were owing to the characteristic pattern of PLA. The diffraction peaks of PBS were observed at 22.5°. The diffraction peaks at 25.9°, 28°, and 32–35° contributed to the characteristic peaks of nHA [42,49,50]. There were no nHA peaks for specimens A0 and B0 without added nHA in the PLA/PBS/PBAT blends. It is also shown that the characteristic peaks of nHA were observed for specimens A3 to A7 and B3 to B7.

doi:10.6342/NTU202502722

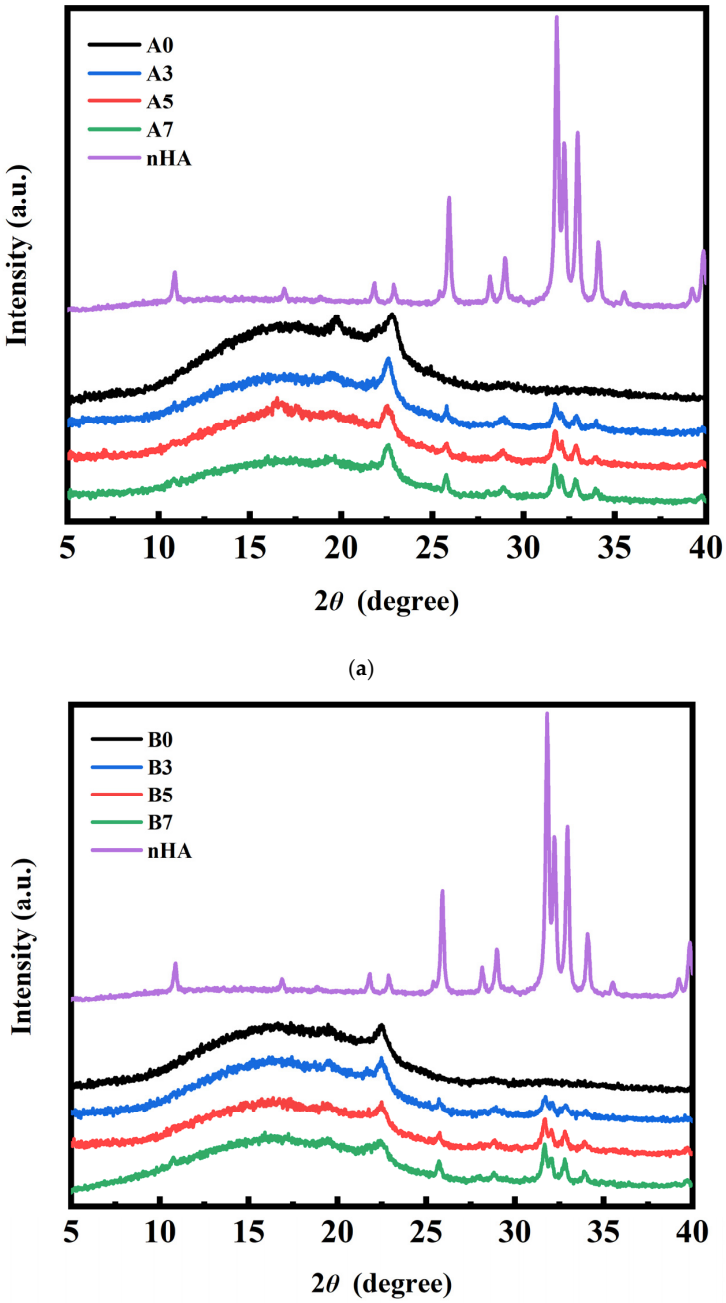

Figure 2. XRD measurement results for polymer blends: (**a**) sample series A and (**b**) sample series B, with various amounts of nHA added.

3.4. DSC and Crystallization Analysis Results for PLA/PBS/PBAT/nHA Blends

DSC analyses were used to measure the reliable thermal history and crystallization of semi-crystalline polymers. The second heating curves of the DSC measurements for sample series A and B with various amounts of nHA added are shown in Figure 3a,b. The glass transition temperature of PLA ($T_{g,PLA}$), cold crystallization temperature (T_{cc}), melting temperature of PLA ($T_{m,PLA}$), enthalpy changes of cold crystallization (ΔH_{cc}), and enthalpy changes of melting of blends (ΔH_m), as listed in Table 4, were retrieved from the DSC thermogram. Addition of nHA affected the crystallization behavior of the PLA/PBS/PBAT

doi:10.6342/NTU202502722

blends and, therefore, their physical properties [42,51]. The relative crystallinity X_c of blends with various formulations was calculated by:

$$X_c = \frac{\Delta H_m - \Delta H_{cc}}{\omega_{PLA}\Delta H_{o,PLA} + \omega_{PBS}\Delta H_{0,\ PBS} + \omega_{PBAT}\Delta H_{0,PBAT}} \times 100\% \quad (1)$$

where ω_{PLA}, ω_{PBS}, and ω_{PBAT} represented the weight fractions of PLA, PBS, and PBAT in the polymer blends, respectively. $\Delta H_{0,PLA}$, $\Delta H_{0,PBS}$, and $\Delta H_{0,PBAT}$ denoted the enthalpy of fusion values for 100% crystalline polymers. The theoretical values ΔH_0 of PLA, PBS, and PBAT are 93.1, 200, and 114 J g^{-1}, respectively [42,51–54].

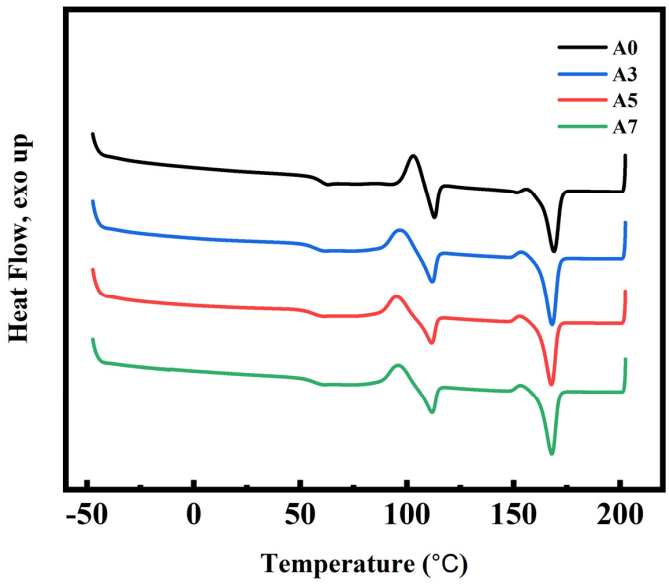

(**a**)

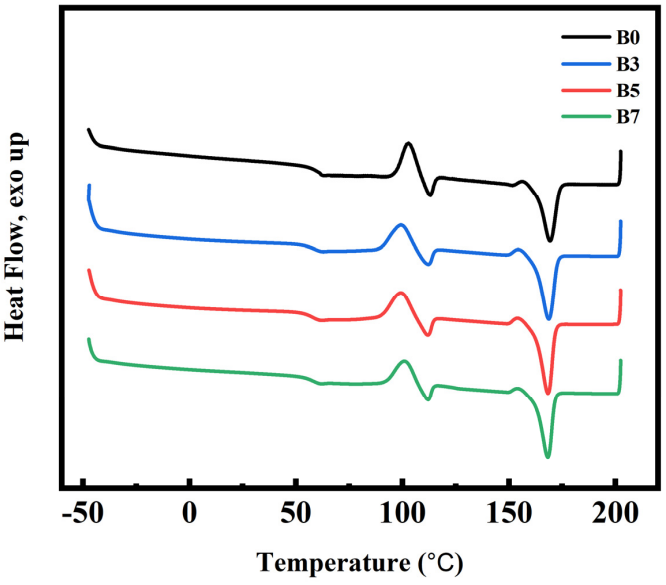

(**b**)

Figure 3. DSC curves (second heating) for polymer blends: (**a**) sample series A and (**b**) sample series B, with various amounts of nHA added.

doi:10.6342/NTU202502722

Table 4. DSC test results and the calculated degree of crystallinity for various polymer blends.

Specimen Code	$T_{g,PLA}$ (°C)	T_{cc} (°C)	$T_{m,PLA}$ (°C)	ΔH_{cc} (J g^{-1})	ΔH_m (J g^{-1})	X_c (%)
A0	62	103	169	12.0	36.3	20.1
A3	63	100	169	13.0	41.9	24.8
A5	63	99	168	14.9	45.2	26.0
A7	61	99	168	13.5	45.0	27.0
B0	62	103	169	15.7	37.9	20.1
B3	63	101	169	18.6	41.3	20.6
B5	63	102	169	15.6	40.2	22.3
B7	63	102	169	14.8	38.5	21.5

As discussed in the literature, the thermodynamic compatibility between PLA and PBS or PLA and PBAT was poor [26,51,55–57]. Nanoparticles were used as a nucleating agent in the crystallization process to increase crystal growth [55–58]. As shown in Table 4, the relative crystallinity X_c in the PLA/PBS/PBAT blend (specimen A0) was 20.1%. The relative crystallinity X_c in polymer blends with the addition of various amounts of nHA (specimens A3, A5, and A7) increased from 24.8 to 27.0%. Increased crystallinity of polymer blends would lead to better mechanical properties. It is observed from Table 4 that sample series B (specimens B0, B3, B5, and B7) also had a similar slight increase in relative crystallinity X_c as the added amount of nHA increased.

3.5. Nonisothermal Crystallization Behavior of PLA/PBS/PBAT/nHA Blends

Heterogeneous nucleation effects in nonisothermal crystallized polymer nanocomposites characterized by DSC have been discussed in the literature [59,60]. Figure 4 shows the heat flow curves of the prepared specimens in this study during cooling from 200 °C to 50 °C at rates of 2.5, 5, 7.5, and 10 °C min^{-1}.

The cooling traces showed that no obvious peak was observed in specimen A0, and its melt crystallization ability was poor. When the nHA content in the specimen increased from 0 to 3 wt%, the appearance of crystallization behavior was observed during the cooling process at 2.5 °C min^{-1}, which exhibited an increase in the crystallization enthalpy value ΔH_{hc} from 0 to 7.8 J g^{-1}. This result can be attributed to the introduced nHA, which may play a role as a nucleating agent and lead to heterogeneous nucleation behavior. As the nHA content further increased, the ΔH_{hc} values increased slightly. Compared with specimen A0, specimen B0 showed a relatively high melt crystallization ability, exhibiting a ΔH_{hc} value of 10.1 J g^{-1} at a cooling rate of 2.5 °C min^{-1} in the absence of nHA. However, similar ΔH_{hc} values were observed in B3, B5, and B7 specimens, indicating that no significant crystallinity change was obtained upon the addition of nHA.

All nonisothermal DSC-measured data are listed in Table 5. The different tendencies of the sample series A and B may result in the basic crystallization ability of PLA in different compositions. The PLA content in specimen A0 was lower, resulting in limited melt crystallization during the cooling process. When nHA was added, a nucleation effect occurred, making crystal formation less difficult. Therefore, as the nHA content increased, the ΔH_{hc} increased significantly. On the other hand, specimen B0 had a relatively higher PLA content and had advantages in crystallization. The addition of nHA in sample series B may not have produced significant improvements in crystallization compared to neat specimen B0 without nHA.

doi:10.6342/NTU202502722

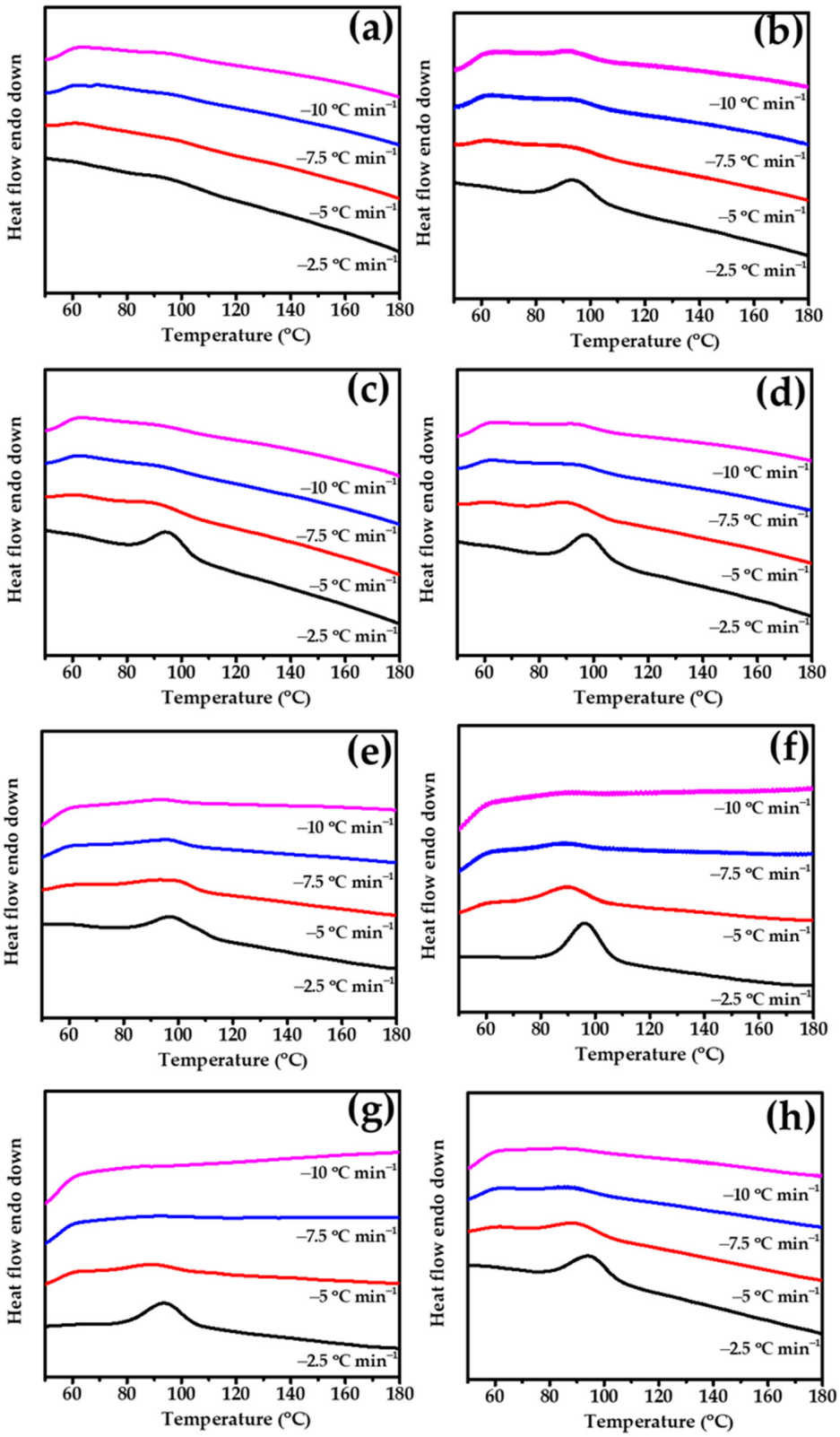

Figure 4. DSC curves of prepared specimens in the cooling process at 2.5, 5, 7.5, and 10 °C min^{-1} (**a**) A0, (**b**) A3, (**c**) A5, (**d**) A7, (**e**) B0, (**f**) B3, (**g**) B5, and (**h**) B7.

doi:10.6342/NTU202502722

Table 5. Crystallization enthalpy values of sample series A and B under various cooling rates.

Specimen Code	Cooling Rate (°C min^{-1})			
	2.5	5	7.5	10
	ΔH_{hc} (J g^{-1})			
A0	0	0	0	0
A3	7.80	1.08	0.63	0.37
A5	9.88	1.70	0.45	0.41
A7	10.90	2.72	0.91	0.50
B0	10.12	3.46	0.74	0.55
B3	11.96	3.31	0.94	0.46
B5	10.09	2.56	0.84	0.36
B7	10.91	2.71	0.94	0.48

3.6. Tensile and Impact Strength Test Results for PLA/PBS/PBAT/nHA Blends

Tensile and impact strength tests were conducted in this study to examine the mechanical properties of various polymer blends. Typical tensile stress measurement results of sample series A and B with various amounts of nHA added are graphically shown in Figure 5. The maximum tensile stress (tensile strength), elongation at maximum tensile stress, tensile modulus, and impact strength data obtained from repeated tests in this study are listed in Table 6. It was observed that sample series B containing 80 wt% PLA exhibited higher tensile strength, up to 57.9 ± 1.0 MPa, while the tensile strength of sample series A with 70 wt% PLA was about 47 to 50 MPa. The elongation of sample series A and B both ranged from 7 to 8%, better than neat PLA (6%, as shown in Table 1) or human bone (1–3% for cortical bone and 3–7% for cancellous bone) [8]. The tensile modulus for sample series A with various nHA contents ranged from 642 to 905 MPa, while that of sample series B could reach 1.0 GPa. Tensile strength and tensile modulus increased with increasing nHA addition, reaching the highest values for polymer blends containing 5 wt% nHA (specimens A5 and B5). Polymer blends with a higher 7 wt% nHA (specimens A7 and B7) showed a slight decrease in tensile strength, suggesting that there might be an optimal nHA addition. Impact strength measurements indicated the toughness of the polymer blend. The impact strength of neat PLA was about 2.5 kJ m^{-2} [21]. All polymer blends yielded better toughness by blending PLA with ductile PBS and PBAT. It can be seen from Table 6 that the additional amount of nHA in this study had no significant effect on the impact strength results for a specific sample series. Examination of these comparisons indicated that specimens B3 or B5 could be the formulations with acceptable mechanical strength for composite bone graft materials. It was deduced from the mechanical property measurements that the added nHA nanoparticles acted as nucleating agents during the crystallization process of the polymer blends, thereby increasing the crystallinity and tensile strength.

Table 6. Tensile and impact test results of polymer blends with various compositions of nHA.

Specimen Code	Maximum Tensile Stress (MPa)	Elongation at Maximum Tensile Stress (%)	Tensile Modulus (MPa)	Impact Strength (kJ m^{-2})
A0	47.1 ± 2.9	7.9 ± 0.4	642.0 ± 109.1	4.83 ± 0.19
A3	47.5 ± 0.7	7.5 ± 0.3	887.8 ± 57.2	4.32 ± 0.17
A5	50.2 ± 1.0	7.4 ± 0.4	905.5 ± 64.1	4.64 ± 0.21
A7	47.4 ± 0.3	6.7 ± 0.3	707.5 ± 15.0	4.20 ± 0.07
B0	49.6 ± 1.6	8.0 ± 0.6	686.1 ± 91.3	3.36 ± 0.20
B3	57.8 ± 0.7	7.1 ± 0.2	1039.4 ± 37.5	3.21 ± 0.16
B5	57.9 ± 1.0	7.3 ± 0.2	1062.2 ± 97.8	3.42 ± 0.17
B7	56.7 ± 1.0	7.3 ± 0.1	962.6 ± 17.4	3.19 ± 0.25

doi:10.6342/NTU202502722

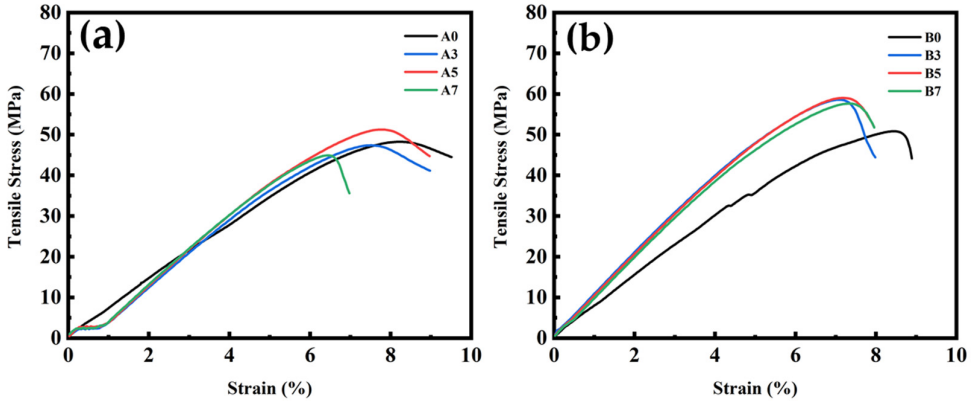

Figure 5. Typical tensile stress measurement results for polymer blends: (**a**) sample series A and (**b**) sample series B, with various amounts of nHA added.

3.7. SEM Analysis Results for PLA/PBS/PBAT/nHA Blends

SEM analyses of fractured surfaces have been demonstrated in the literature discussing polymer composite morphology and additive distribution in the polymer matrix [61–63]. The transition from ductile to brittle in polymer composites and the morphology–mechanical properties relationship can be examined using SEM analyses. SEM images of the impact-fractured surfaces for sample series A and B of polymer blends in this study are shown in Figures 6 and 7, respectively.

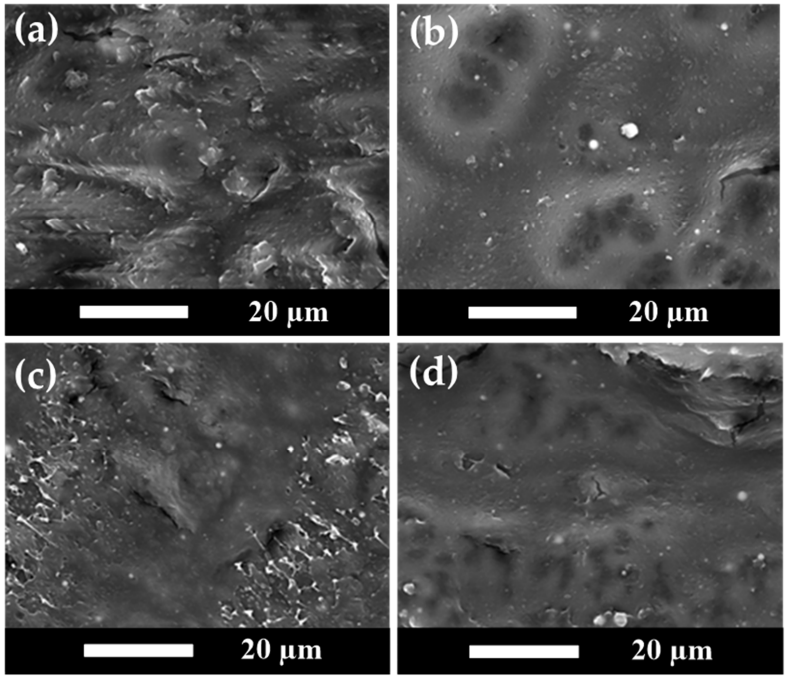

Figure 6. Comparison of the SEM images for polymer blend sample series A with various amounts of nHA added in (**a**) Specimen A0, (**b**) Specimen A3, (**c**) Specimen A5, and (**d**) Specimen A7.

Figure 6a shows the SEM image of specimen A0. Figure 6b–d show the SEM images of specimens A3, A5, and A7, respectively. Figure 6a indicates that specimen A0 without nHA presented a relatively rough and tough fractured surface. For specimen A3 with 3 wt% nHA added, well-dispersed nHA particles can be observed as small white dots in Figure 6b. With the higher amount of added nHA, a brittle fractured morphology with cracks appeared, as shown in Figure 6c,d. A transition in fractured surface morphology from relatively rough and ductile to hard and brittle was observed. These SEM results

doi:10.6342/NTU202502722

are also supported by the TEM results discussed in the next section, showing that the nanoparticles were uniformly distributed. The effect of nHA addition on tensile and impact strength was consistent with the SEM results, where the polymer blends became harder and brittle with increasing nHA addition. As the amount of nHA added increased, the mechanical tensile strength showed an increasing trend.

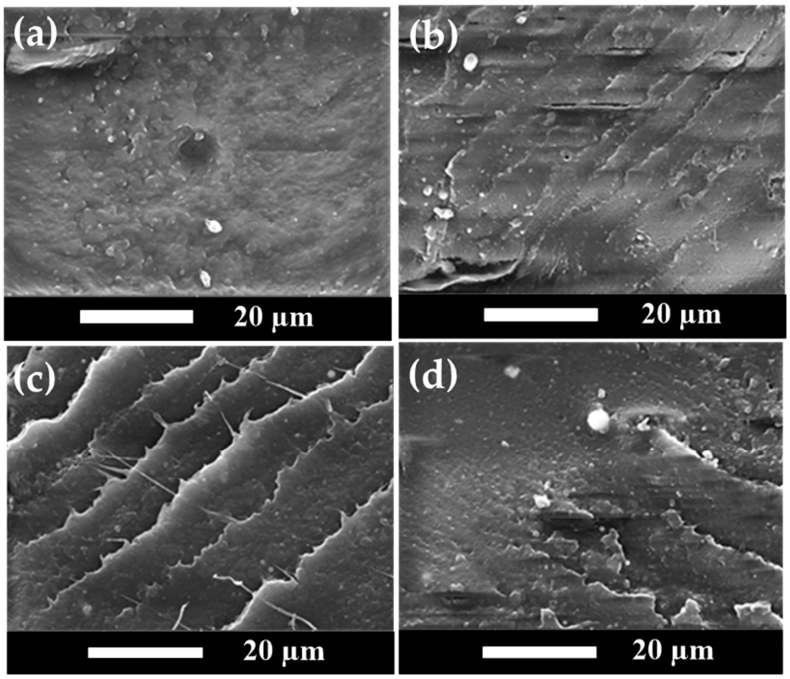

Figure 7. Comparison of the SEM images for polymer blend sample series B with various amounts of nHA added in (**a**) Specimen B0, (**b**) Specimen B3, (**c**) Specimen B5, and (**d**) Specimen B7.

Figure 7 shows similar SEM images for sample series B, containing 80 wt% PLA. An impact-fractured surface morphology consistent with Figure 6 was observed. No nHA particles were detected in Figure 7a, which presented a relatively rough surface. When nHA particles were added to the polymer blends, they produced sharp fractured surface morphologies, as shown in Figure 7b–d. The nHA particles were well dispersed in the polymer matrix and became aggregated at higher nHA contents. As the amount of nHA added increased, the fracture morphology once again exhibited hard and brittle characteristics. To confirm the chemical compositions of nanoparticles shown in the SEM images, the EDX spectrum for a typical polymer blend of specimen B7 is shown in Figure 8. The characteristic peaks of Ca and P elements shown in Figure 8 indicated the nHA particles in specimens.

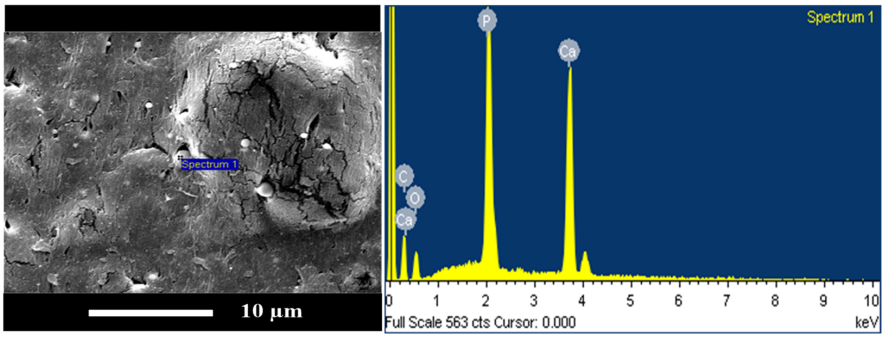

Figure 8. Typical results of the EDX spectra of a polymer blend (specimen B7, with the addition of 7 wt% nHA).

doi:10.6342/NTU202502722

3.8. TEM Measurement Results for PLA/PBS/PBAT/nHA Blends

TEM images of sample series A are shown in Figure 9 at 20,000× magnification. No nHA particle images were detected in specimen A0. In addition, phase separation morphology in the blend can be observed in Figure 9a, with a continuous region (or lighter region) as the major component PLA matrix and a darker region as the minor PBS/PBAT dispersed phase. With the addition of 3 wt% nHA, the TEM image shown in Figure 9b exhibits the presence of small black dots of nHA, with a particle size in the range of 70–100 nm. Furthermore, the PBS/PBAT dispersed phase became smaller in size with the addition of nHA particles, indicating that the addition of nHA particles helped to disperse polymer phases during the twin-screw mixing process. With a further increased amount of nHA addition from 5 to 7 wt%, the degree of uniform dispersion of the polymer phases also increased, and PBS/PBAT phases became even smaller, as seen in the images shown in Figure 9c,d. However, it is noted that with a higher amount of nHA addition, nHA particles became larger due to aggregation during mixing. For 7 wt% of nHA addition, a near-micrometer size of nHA particles was observed, as seen in the image shown in Figure 9d. Similar results for TEM images of sample series B are presented in Figure 10. For specimen B0, no nHA particle images were detected, as seen in Figure 10a. When the addition of nHA increased from 3 to 7 wt% as shown in Figure 10b–d, an increased number of fine black dots of nHA particles was displayed. TEM images also showed nHA-induced morphological refinement, indicating that nHA helped disperse polymer domains.

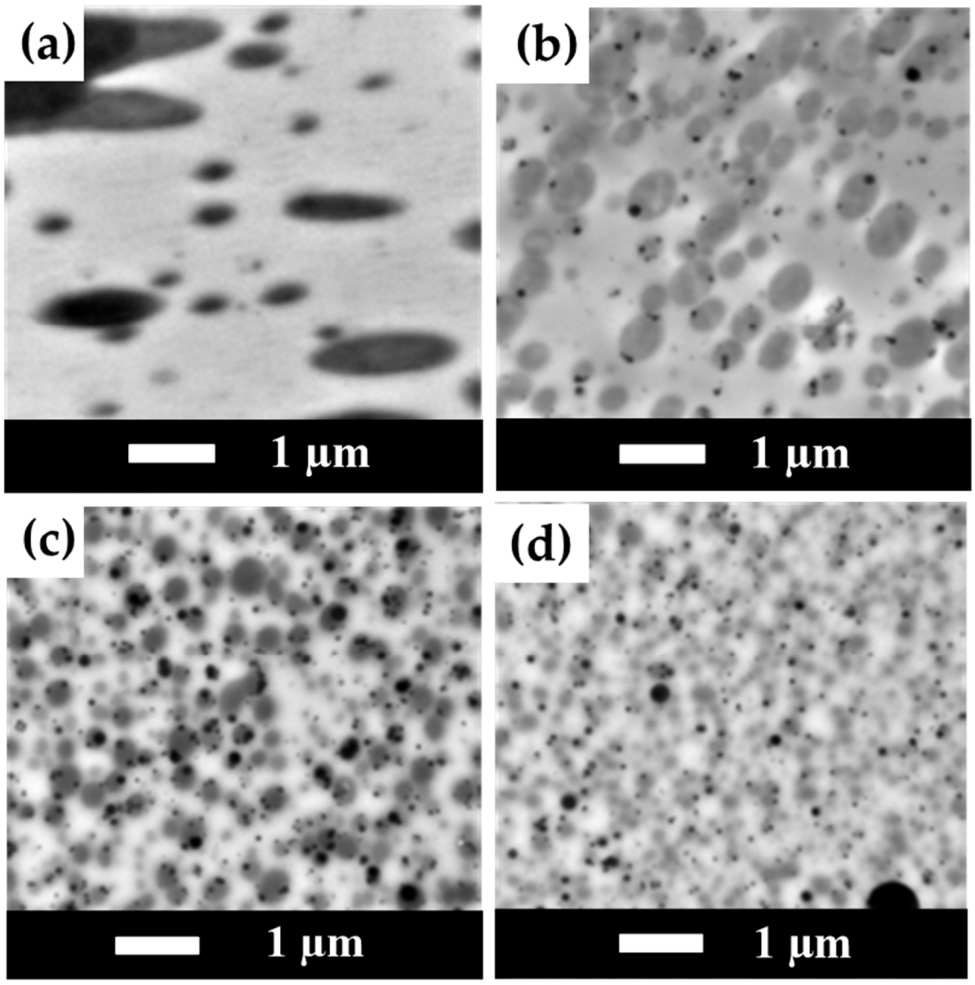

Figure 9. TEM images for polymer blends of sample series A with various amounts of nHA added (magnification 20,000×). (**a**) Specimen A0, (**b**) Specimen A3, (**c**) Specimen A5, and (**d**) Specimen A7.

doi:10.6342/NTU202502722

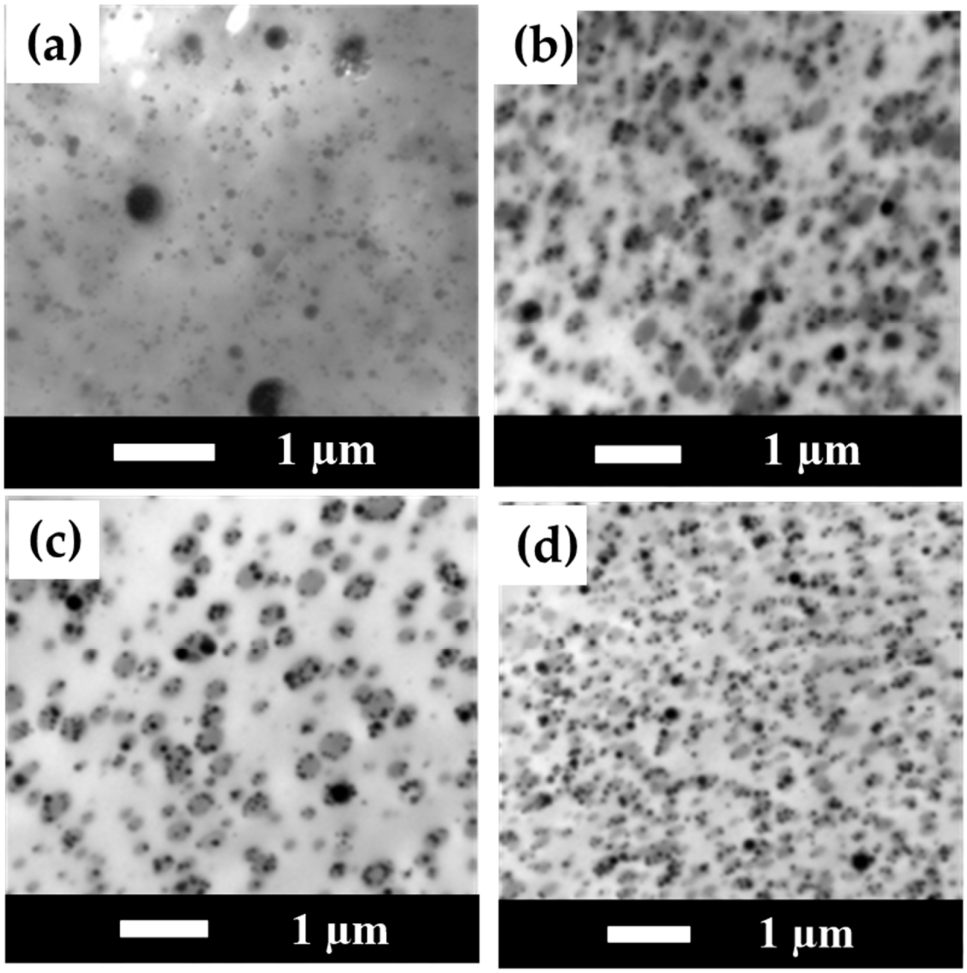

Figure 10. TEM images for polymer blends of sample series B with various amounts of nHA added (magnification 20,000×). (**a**) Specimen B0, (**b**) Specimen B3, (**c**) Specimen B5, and (**d**) Specimen B7.

3.9. TGA for PLA/PBS/PBAT/nHA Blends

This study examined the thermal stability of polymer blends with different formulations using thermogravimetric analysis (TGA). The results for sample series A and B are shown with TGA and DTGA thermograms in Figures 11 and 12, respectively. Table 7 lists the decomposition temperatures for 5% and 50% weight loss ($T_{5\%}$ and $T_{50\%}$), the temperature of maximum decomposition rate (T_{max}), and residual weight percent at 600 °C (W_R) for all specimens measured in this study. For sample series A, the TGA thermograms in Figure 11a show that the main decomposition temperature of each specimen (A0 to A7) was between 300 and 400 °C. The DTGA thermograms shown in Figure 11b depict the two-step decomposition of each specimen. The first peak indicated the maximum decomposition rate of PLA [64], and the second peak was owing to the maximum decomposition rate of PBS/PBAT. As shown in Figure 11 and Table 7, adding nHA did not seem to significantly affect the T_{max} of the polymer blends. The residual weight percent in the temperature range of 500 to 600 °C increased reasonably well with increasing thermally stable inorganic nHA content, as shown in Figure 11a and Table 7. The similar TGA and DTGA thermograms of sample series B are shown in Figure 12, with data also listed in Table 7. The main decomposition temperature range was also between 300 and 400 °C, as shown in Figure 12a. The increase in residual weight percent for four specimens of sample series B was again consistent with the increasing amount of nHA added. From the TGA results, polymer blends in this study all had good thermal stability for bone graft material applications.

doi:10.6342/NTU202502722

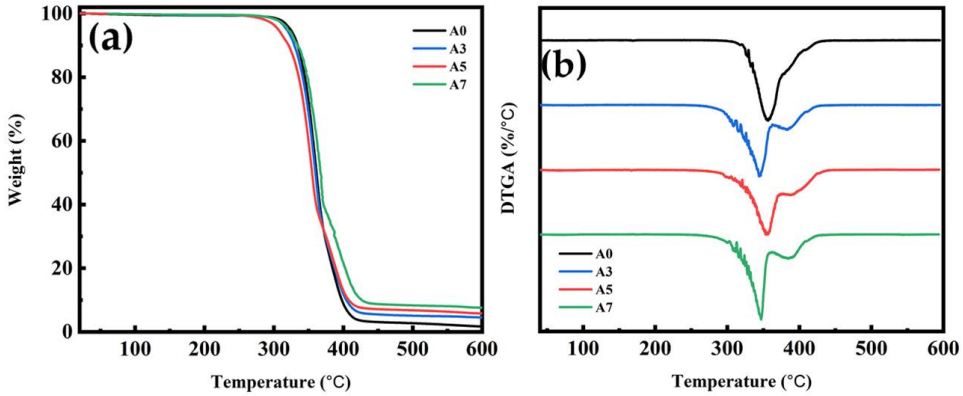

Figure 11. Thermogravimetric analysis results of (**a**) TG and (**b**) DTG thermograms for sample series A, with various amounts of nHA added.

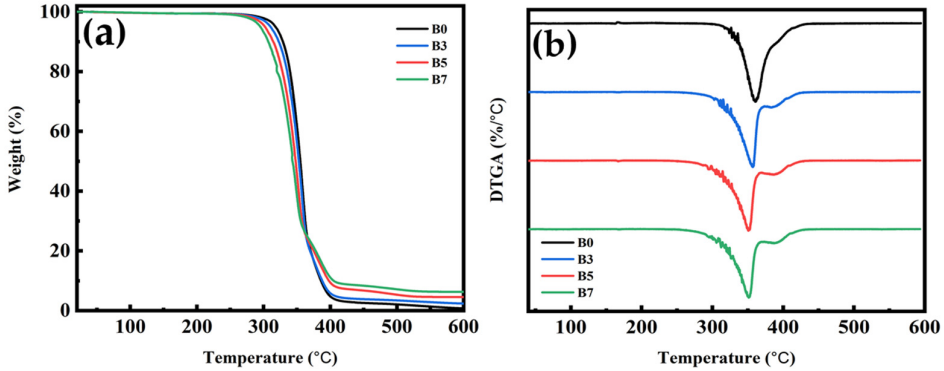

Figure 12. Thermogravimetric analysis results of (**a**) TG and (**b**) DTG thermograms for sample series B, with various amounts of nHA added.

Table 7. Thermogravimetric measurement results for PLA/PBS/PBAT/nHA blends.

Specimen Code	$T_{5\%}$ (°C)	$T_{50\%}$ (°C)	T_{max} (°C)	W_R (%) at 600 °C
A0	325	361	361	1.6
A3	318	360	360	4.5
A5	306	354	355	5.7
A7	319	367	366	7.6
B0	317	355	371	0.7
B3	310	353	369	2.3
B5	302	348	362	4.5
B7	295	343	352	6.3

3.10. Water Absorption Measurement Results for PLA/PBS/PBAT/nHA Blends

The water absorption percentage gain (WA) was calculated by:

$$\mathrm{WA}(\%) = \frac{W_t - W_d}{W_d} \times 100\% \quad (2)$$

where W_d was the weight of the sample after drying (dried at 50 °C for 2 days before the water absorption test) and W_t was the weight of the sample measured after immersion in distilled water for t days (t = 1, 2, 5, and 8). The water absorption results for all specimens after immersion in distilled water for 24 h are shown in Figure 13. For sample series A, due to the hydrophilicity of nHA, the water absorption tended to increase with the increase in nHA addition. Sample series B also exhibited a similar water absorption trend. Compared

doi:10.6342/NTU202502722

to sample series A, sample series B displayed lower water absorption due to its higher PLA content. For the 24 h test, the water absorption of specimens B5 and B7 was about 15% better than that of specimen B0. The water absorption results for a longer time are depicted in Figure 14 for all specimens. It is demonstrated that after five days of water immersion, the degree of water absorption of each specimen increased by about 40% to 50% compared to the degree of water absorption on the first day. After absorbing water for eight days, the degree of water absorption increased by about 70 to 80% compared with one-day water absorption results. These increased water absorption percentages were consistent with those shown in the literature for composites involving PLA [65,66]. The results of water absorption indicated that the addition of hydrophilic nHA enhanced the water absorption rate, which is beneficial to the application of polymer blends in bone tissue engineering.

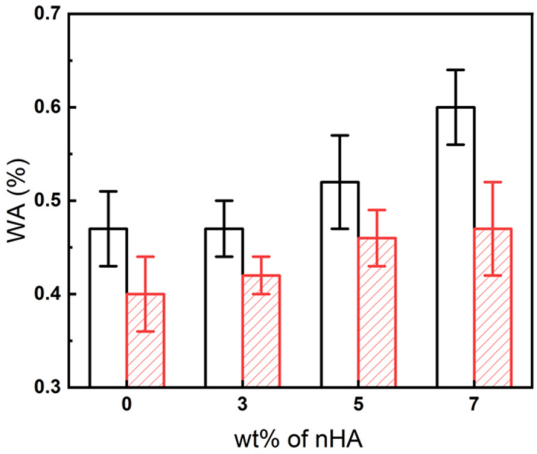

Figure 13. Comparison of water absorption percentage gain (WA) at 24 h for all specimens with various amounts of nHA added. (▭: sample series A; ▨: sample series B).

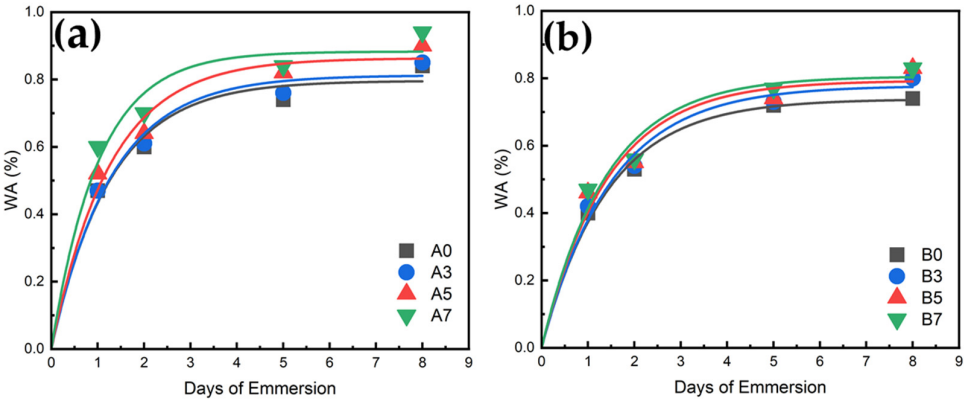

Figure 14. Water absorption profiles for (**a**) sample series A and (**b**) sample series B.

4. Conclusions

The physical and mechanical properties of novel bio-based polymer blends of PLA/PBS/PBAT/nHA were investigated in this study. The aim was to screen promising formulations of polymer blends with biocompatible and osteoconductive nHA to provide options for bone graft materials. Various analytical results for physical and mechanical property tests were reported. The conclusions are as follows: (1) Polymer blend formulations containing 70 or 80 wt% PLA content with the addition of 3 to 5 wt% nHA exhibited tensile strengths ranging from 47 to 57 MPa, suitable for bone graft applications. The elongation and impact strength of these formulations were also satisfactory. (2) The thermal degradation temperatures of various PLA/PBS/PBAT/nHA blends ranged from 300 to 400 °C, suggesting that the polymer blends had satisfactory thermal stability. (3) The

doi:10.6342/NTU202502722

addition of nHA in the polymer blends increased water absorption due to its hydrophilicity. Addition of 5 wt% nHA resulted in about a 15% increase in water absorption in the 24 h water immersion test compared to polymer blends without nHA.

Author Contributions: Conceptualization, P.-H.C. and C.-W.C.; data curation, P.-H.C., H.-I.M. and C.-A.D.; formal analysis, P.-H.C., C.-S.S. and J.-C.T.; funding acquisition, C.-W.C.; investigation, C.-W.C. and F.-H.L.; methodology, P.-H.C., C.-W.C., H.-I.M., C.-A.D., C.-S.S. and J.-C.T.; supervision, C.-W.C. and F.-H.L.; writing—original draft, P.-H.C.; writing—review and editing, C.-W.C. All authors have read and agreed to the published version of the manuscript.

Funding: The authors gratefully acknowledge the financial support from the National Science and Technology Council of Taiwan (NSTC 111-2222-E-027-005).

Institutional Review Board Statement: Not applicable.

Data Availability Statement: Data are contained within the article.

Acknowledgments: The authors are grateful to the National Taiwan University, the National Taipei University of Technology, and Ming Chi University of Technology for supporting the experimental equipment. Valuable comments and assistance from Chun-Ta Chen, Ming-You Chen, Jui-Yang Chou, and Yu-Lin Wang are highly appreciated.

Conflicts of Interest: The authors declare no conflict of interest.

References

1. Liu, A.P.; Appel, E.A.; Ashby, P.D.; Baker, B.M.; Franco, E.; Gu, L.; Haynes, K.; Joshi, N.S.; Kloxin, A.M.; Kouwer, P.H.J.; et al. The living interface between synthetic biology and biomaterial design. *Nat. Mater.* **2022**, *21*, 390–397. [CrossRef] [PubMed]
2. Eldeeb, A.E.; Salah, S.; Elkasabgy, N.A. Biomaterials for tissue engineering applications and current updates in the field: A comprehensive review. *AAPS PharmSciTech* **2022**, *23*, 267. [CrossRef] [PubMed]
3. Ajmal, S.; Hashmi, F.A.; Imran, I. Recent progress in development and applications of biomaterials. *Mater. Today Proc.* **2022**, *62*, 385–391. [CrossRef]
4. Williams, D.F. Challenges with the development of biomaterials for sustainable tissue engineering. *Front. Bioeng. Biotechnol.* **2019**, *7*, 127. [CrossRef] [PubMed]
5. Pollock, J.R.; Moore, M.L.; Hogan, J.S.; Haglin, J.M.; Brinkman, J.C.; Doan, M.K.; Chhabra, A. Orthopaedic group practice size is increasing. *Sports Med. Arthrosc. Rehabil. Ther. Technol.* **2021**, *3*, e1937–e1944. [CrossRef] [PubMed]
6. Szpalski, C.; Wetterau, M.; Barr, J.; Warren, S.M. Bone tissue engineering: Current strategies and techniques—Part I: Scaffolds. *Tissue Eng. Part B Rev.* **2012**, *18*, 246–257. [CrossRef] [PubMed]
7. Polo-Corrales, L.; Latorre-Esteves, M.; Ramirez-Vick, J.E. Scaffold design for bone regeneration. *J. Nanosci. Nanotechnol.* **2014**, *14*, 15–56. [CrossRef]
8. Lee, S.S.; Du, X.; Kim, I.; Ferguson, S.J. Scaffolds for bone-tissue engineering. *Matter* **2022**, *5*, 2722–2759. [CrossRef]
9. Haugen, H.J.; Lyngstadaas, S.P.; Rossi, F.; Perale, G. Bone grafts: Which is the ideal biomaterial? *J. Clin. Periodontol.* **2019**, *46* (Suppl. S21), 92–102. [CrossRef]
10. Qu, H.; Fu, H.; Han, Z.; Sun, Y. Biomaterials for bone tissue engineering scaffolds: A review. *RSC Adv.* **2019**, *9*, 26252–26262. [CrossRef]
11. Koons, G.L.; Diba, M.; Mikos, A.G. Materials design for bone—Tissue engineering. *Nat. Rev. Mater.* **2020**, *5*, 584–603. [CrossRef]
12. Ravoor, J.; Thangavel, M.; Elsen, R.S. Comprehensive review on design and manufacturing of bioscaffolds for bone reconstruction. *ACS Appl. Bio Mater.* **2021**, *4*, 8129–8158. [CrossRef] [PubMed]
13. Bahraminasab, M.; Janmohammadi, M.; Arab, S.; Talebi, A.; Nooshabadi, V.T.; Koohsarian, P.; Nourbakhsh, M.S. Bone scaffolds: An incorporation of biomaterials, cells, and biofactors. *ACS Biomater. Sci. Eng.* **2021**, *7*, 5397–5431. [CrossRef] [PubMed]
14. Collins, M.N.; Ren, G.; Young, K.; Pina, S.; Reis, R.L.; Oliveira, J.M. Scaffold fabrication technologies and structure/function properties in bone tissue engineering. *Adv. Funct. Mater.* **2021**, *31*, 2010609. [CrossRef]
15. Szczesny, G.; Kopec, M.; Politis, D.J.; Kowalewski, Z.L.; Łazarski, A.; Szolc, T. A review on biomaterials for orthopaedic surgery and traumatology: From past to present. *Materials* **2022**, *15*, 3622. [CrossRef] [PubMed]
16. Sheikh, Z.; Najeeb, S.; Khurshid, Z.; Verma, V.; Rashid, H.; Glogauer, M. Biodegradable materials for bone repair and tissue engineering applications. *Materials* **2015**, *8*, 5744–5794. [CrossRef] [PubMed]
17. Wei, S.; Ma, J.-X.; Xu, L.; Gu, X.-S.; Ma, X.-L. Biodegradable materials for bone defect repair. *Mil. Med. Res.* **2020**, *7*, 54. [CrossRef]
18. Modrák, M.; Trebunová, M.; Balogová, A.F.; Hudák, R.; Živcák, J. Biodegradable materials for tissue engineering: Development, classification and current applications. *J. Funct. Biomater.* **2023**, *14*, 159. [CrossRef]
19. Yu, H.; Liu, H.; Shen, Y.; Ao, Q. Synthetic biodegradable polymer materials in the repair of tumor-associated bone defects. *Front. Bioeng. Biotechnol.* **2023**, *11*, 1096525. [CrossRef]

doi:10.6342/NTU202502722

20. Bernardo, M.P.; da Silva, B.C.R.; Hamouda, A.E.I.; de Toledo, M.A.S.; Schalla, C.; Rütten, S.; Goetzke, R.; Mattoso, L.H.C.; Zenke, M.; Sechi, A. PLA/Hydroxyapatite scaffolds exhibit in vitro immunological inertness and promote robust osteogenic differentiation of human mesenchymal stem cells without osteogenic stimuli. *Sci. Rep.* **2022**, *12*, 2333. [CrossRef]
21. Zhao, X.; Hu, H.; Wang, X.; Yu, X.; Zhou, W.; Peng, S. Super tough poly(lactic acid) blends: A comprehensive review. *RSC Adv.* **2020**, *10*, 13316–13368. [CrossRef]
22. Nofar, M.; Sacligil, D.; Carreau, P.J.; Kamal, M.R.; Heuzey, M.-C. Poly(lactic acid) blends: Processing, properties and applications. *Int. J. Biol. Macromol.* **2019**, *125*, 307–360. [CrossRef] [PubMed]
23. De Matos Costa, A.R.; Crocitti, A.; de Carvalho, L.H.; Carroccio, S.C.; Cerruti, P.; Santagata, G. Properties of biodegradable films based on poly(butylene Succinate) (PBS) and poly(butylene Adipate-co-Terephthalate) (PBAT) blends. *Polymers* **2020**, *12*, 2317. [CrossRef] [PubMed]
24. Hu, D.; Xue, K.; Liu, Z.; Xu, Z.; Zhao, L. The essential role of PBS on PBAT foaming under supercritical CO_2 toward green engineering. *J. CO2 Util.* **2022**, *60*, 101965. [CrossRef]
25. Sun, Z.; Wang, L.; Zhou, J.; Fan, X.; Xie, H.; Zhang, H.; Zhang, G.; Shi, X. Influence of polylactide (PLA) stereocomplexation on the microstructure of PLA/PBS blends and the cell morphology of their microcellular foams. *Polymers* **2020**, *12*, 2362. [CrossRef] [PubMed]
26. Su, S.; Kopitzky, R.; Tolga, S.; Kabasci, S. Polylactide (PLA) and its blends with poly(butylene succinate) (PBS): A brief review. *Polymers* **2019**, *11*, 1193. [CrossRef] [PubMed]
27. Zhang, X.; Liu, Q.; Shi, J.; Ye, H.; Zhou, Q. Distinctive tensile properties of the blends of poly(l-lactic acid) (PLLA) and poly(butylene succinate) (PBS). *J. Polym. Environ.* **2018**, *26*, 1737–1744. [CrossRef]
28. Ou-Yang, Q.; Guo, B.; Xu, J. Preparation and characterization of poly(butylene succinate)/polylactide blends for fused deposition modeling 3D printing. *ACS Omega* **2018**, *3*, 14309–14317. [CrossRef]
29. Yu, P.; Mi, H.-Y.; Huang, A.; Geng, L.-H.; Chen, B.-Y.; Kuang, T.-R.; Mou, W.-J.; Peng, X.-F. Effect of Poly(butylenes succinate) on poly(lactic acid) foaming behavior: Formation of open cell structure. *Ind. Eng. Chem. Res.* **2015**, *54*, 6199–6207. [CrossRef]
30. Zhao, H.; Liu, H.; Liu, Y.; Yang, Y. Blends of poly(butylene adipate-co-terephthalate) (PBAT) and stereocomplex polylactide with improved rheological and mechanical properties. *RSC Adv.* **2020**, *10*, 10482–10490. [CrossRef]
31. Kang, Y.; Chen, P.; Shi, X.; Zhang, G.; Wang, C. Preparation of open-porous stereocomplex PLA/PBAT scaffolds and correlation between their morphology, mechanical behavior, and cell compatibility. *RSC Adv.* **2018**, *8*, 12933–12943. [CrossRef] [PubMed]
32. Canales, D.A.; Pinones, N.; Saavedra, M.; Loyo, C.; Palza, H.; Peponi, L.; Leones, A.; Baier, R.V.; Boccaccini, A.R.; Grünelwald, A.; et al. Fabrication and assessment of bifunctional electrospun poly(L-lactic acid) scaffolds with bioglass and zinc oxide nanoparticles for bone tissue engineering. *Int. J. Biol. Macromol.* **2023**, *228*, 78–88. [CrossRef] [PubMed]
33. Kaliva, M.; Georgopoulou, A.; Dragatogiannis, D.A.; Charitidis, C.A.; Chatzinikolaidou, M.; Vamvakaki, M. Biodegradable chitosan-graft-poly(l-lactide) copolymers for bone tissue engineering. *Polymers* **2020**, *12*, 316. [CrossRef] [PubMed]
34. Yao, Q.; Song, Z.; Li, J.; Zhang, L. Micromorphology, mechanical, crystallization and permeability properties analysis of HA/PBAT/PLA (HA, hydroxyapatite; PBAT, poly(butylene adipate-co-butylene terephthalate); PLA, polylactide) degradability packaging films. *Polym. Int.* **2020**, *69*, 301–307. [CrossRef]
35. Dos Santos Silva, A.; Rodrigues, B.V.M.; Oliveira, F.C.; Carvalho, J.O.; de Vasconcellos, L.M.R.; de Araújo, J.C.R.; Marciano, F.R.; Lobo, A.O. Characterization and in vitro and in vivo assessment of poly(butylene adipate-co-terephthalate)/nano-hydroxyapatite composites as scaffolds for bone tissue engineering. *J. Polym. Res.* **2019**, *26*, 53. [CrossRef]
36. Santana-Melo, G.F.; Rodrigues, B.V.M.; da Silva, E.; Ricci, R.; Marciano, F.R.; Webster, T.J.; Vasconcellosa, L.M.R.; Lobo, A.O. Electrospun ultrathin PBAT/nHAp fibers influenced the in vitro and in vivo osteogenesis and improved the mechanical properties of neoformed bone. *Colloids Surf. B* **2017**, *155*, 544–552. [CrossRef] [PubMed]
37. Zhang, J.; Li, J.; Jia, G.; Jiang, Y.; Liu, Q.; Yang, X.; Pan, S. Improving osteogenesis of PLGA/HA porous scaffolds based on dual delivery of BMP-2 and IGF-1 via a polydopamine coating. *RSC Adv.* **2017**, *7*, 56732–56742. [CrossRef]
38. Khan, M.A.; Hussain, Z.; Liaqat, U.; Liaqat, M.A.; Zahoor, M. Preparation of PBS/PLLA/HAP composites by the solution casting method: Mechanical properties and biocompatibility. *Nanomaterials* **2020**, *10*, 1778. [CrossRef]
39. Gui, X.; Peng, W.; Xu, X.; Su, Z.; Liu, G.; Zhou, Z.; Liu, M.; Li, Z.; Song, G.; Zhou, C.; et al. Synthesis and application of nanometer hydroxyapatite in biomedicine. *Nanotechnol. Rev.* **2022**, *11*, 2154–2168. [CrossRef]
40. Wang, W.; Zhang, B.; Li, M.; Li, J.; Zhang, C.; Han, Y.; Wang, L.; Wang, K.; Zhou, C.; Liu, L.; et al. 3D printing of PLA/n-HA composite scaffolds with customized mechanical properties and biological functions for bone tissue engineering. *Compos. B Eng.* **2021**, *224*, 109192. [CrossRef]
41. Mou, Z.-L.; Zhao, L.-J.; Zhang, Q.-A.; Zhang, J.; Zhang, Z.-Q. Preparation of porous PLGA/HA/collagen scaffolds with supercritical CO_2 and application in osteoblast cell culture. *J. Supercrit. Fluids* **2011**, *58*, 398–406. [CrossRef]
42. Yan, D.; Wang, Z.; Guo, Z.; Ma, Y.; Wang, C.; Tan, H.; Zhang, Y. Study on the properties of PLA/PBAT composite modified by nanohydroxyapatite. *J. Mater. Res. Technol.* **2020**, *9*, 11895–11904. [CrossRef]
43. Park, J.-W.; Hwang, J.-U.; Back, J.-H.; Jang, S.-W.; Kim, H.-J.; Kim, P.-S.; Shin, S.; Kim, T. High strength PLGA/Hydroxyapatite composites with tunable surface structure using PLGA direct grafting method for orthopedic implants. *Compos. B Eng.* **2019**, *178*, 107449. [CrossRef]
44. Lowe, B.; Hardy, J.G.; Walsh, L.J. Optimizing nanohydroxyapatite nanocomposites for bone tissue engineering. *ACS Omega* **2020**, *5*, 1–9. [CrossRef] [PubMed]

doi:10.6342/NTU202502722

45. Velasco, M.A.; Narváez-Tovar, C.A.; Garzón-Alvarado, D.A. Design, materials, and mechanobiology of biodegradable scaffolds for bone tissue engineering. *BioMed Res. Int.* **2015**, *2015*, 729076. [CrossRef] [PubMed]
46. Shelton, T.J.; Delman, C.; McNary, S.; Taylor, J.R.; Marder, R.A. Aging decreases the ultimate tensile strength of bone-partellar tendon-bone allografts. *Arthroscopy* **2021**, *37*, 2173–2180. [CrossRef] [PubMed]
47. Rodrigues, S.C.S.; de Mesquita, F.A.S.; de Carvalho, L.H.; Alves, T.S.; Folkersma, R.; Araújo, R.S.d.R.M.; Oliveira, A.D.; Barbosa, R. Preparation and characterization of polymeric films based on PLA, PBAT and corn starch and babassu mesocarp starch by flat extrusion. *Mater. Res. Express* **2021**, *8*, 035305. [CrossRef]
48. Gheisari, H.; Karamian, E.; Abdellahi, M. A novel hydroxyapatite–Hardystonite nanocomposite ceramic. *Ceram. Int.* **2015**, *41*, 5967–5975. [CrossRef]
49. Rasheed, M.; Jawaid, M.; Parveez, B.; Bhat, A.H.; Alamery, S. Morphology, structural, thermal, and tensile properties of bamboo microcrystalline cellulose/poly(Lactic Acid)/poly(Butylene Succinate) Composites. *Polymers* **2021**, *13*, 465. [CrossRef]
50. Solechan, S.; Suprihanto, A.; Widyanto, S.A.; Triyono, J.; Fitriyana, D.F.; Siregar, J.P.; Cionita, T. Characterization of PLA/PCL/Nano-Hydroxyapatite (nHA) biocomposites prepared via cold isostatic pressing. *Polymers* **2023**, *15*, 559. [CrossRef]
51. Qiu, T.Y.; Song, M.; Zhao, L.G. Testing, characterization and modelling of mechanical behaviour of poly (lactic-acid) and poly (butylene succinate) blends. *Mech. Adv. Mater. Mod. Process.* **2016**, *2*, 7. [CrossRef]
52. Qahtani, M.; Wu, F.; Misra, M.; Gregori, S.; Mielewski, D.F.; Mohanty, A.K. Experimental design of sustainable 3D-printed poly(Lactic acid)/biobased poly(butylene succinate) blends via fused deposition modeling. *ACS Sustain. Chem. Eng.* **2019**, *7*, 14460–14470. [CrossRef]
53. Righetti, M.C.; Di Lorenzo, M.L.; Cinelli, P.; Gazzano, M. Temperature dependence of the rigid amorphous fraction of poly(butylene succinate). *RSC Adv.* **2021**, *11*, 25731–25737. [CrossRef] [PubMed]
54. Bai, J.; Pei, H.; Zhou, X.; Xie, X. Reactive compatibilization and properties of low-cost and high-performance PBAT/thermoplastic starch blends. *Eur. Polym. J.* **2021**, *143*, 110198. [CrossRef]
55. Zhao, X.; Zhang, D.; Yu, S.; Zhou, H.; Peng, S. Recent advances in compatibility and toughness of poly(lactic acid)/poly(butylene succinate) blends. *e-Polymers* **2021**, *21*, 793–810. [CrossRef]
56. Wang, B.; Jin, Y.; Kang, K.; Yang, N.; Weng, Y.; Huang, Z.; Men, S. Investigation on compatibility of PLA/PBAT blends modified by epoxy-terminated branched polymers through chemical micro-crosslinking. *e-Polymers* **2020**, *20*, 39–54. [CrossRef]
57. Zhou, Y.; Qiu, S.; Waterhouse, G.I.N.; Zhang, K.; Xu, J. Enhancing the properties of PBAT/PLA composites with novel phosphorus-based ionic liquid compatibilizers. *Mater. Today Commun.* **2021**, *27*, 102407. [CrossRef]
58. De Luna, M.S.; Filippone, G. Effects of nanoparticles on the morphology of immiscible polymer blends—Challenges and opportunities. *Eur. Polym. J.* **2016**, *79*, 198–218. [CrossRef]
59. Zhao, Q.; Wang, B.; Qin, C.; Li, Q.; Liu, C.; Shen, C.; Wang, Y. Nonisothermal melt and cold crystallization behaviors of biodegradable poly(lactic acid)/Ti3C2Tx MXene nanocomposites. *J. Therm. Anal. Calorim.* **2022**, *147*, 2239–2251. [CrossRef]
60. Mata-Padilla, J.M.; Avila-Orta, C.A.; Almendarez-Camarillo, A.; Martinez-Colunga, J.G.; Hernandez-Hernandez, E.; Cruz-Delgado, V.J.; Gonzalez-Morones, P.; Solis-Rosales, S.G.; Gonzalez-Calderon, J.A. Non-isothermal crystallization behavior of isotactic polypropylene/copper nanocomposites. *J. Therm. Anal. Calorim.* **2021**, *143*, 2919–2932. [CrossRef]
61. Gao, H.; Qiang, T. Fracture surface morphology and impact strength of cellulose/PLA composites. *Materials* **2017**, *10*, 624. [CrossRef]
62. Pivsa-Art, W.; Pivsa-Art, S. Effect of talc on mechanical characteristics and fracture toughness of poly(lactic acid)/poly(butylene succinate) blend. *J. Polym. Environ.* **2019**, *27*, 1821–1827. [CrossRef]
63. Mao, H.-I.; Hsu, T.-S.; Chen, C.-W.; Huang, K.-W.; Rwei, S.-P. Sunthesis and characteristics of poly(ethylene terephthalate) with EO-PO-EO triblock copolymers: A thermal and mechanical property study. *J. Appl. Polym. Sci.* **2022**, *139*, e51065. [CrossRef]
64. Zhao, T.; Yu, J.; Zhang, X.; Han, W.; Zhang, S.; Pan, H.; Zhang, Q.; Yu, X.; Bian, J.; Zhang, H. Thermal, crystallization, and mechanical properties of polylactic acid (PLA)/poly(butylene succinate) (PBS) blends. *Polym. Bull.* **2023**, 1–24. [CrossRef]
65. Ecker, J.V.; Haider, A.; Burzic, I.; Huber, A.; Eder, G.; Hild, S. Mechanical properties and water absorption behaviour of PLA and PLA/wood composites prepared by 3D printing and injection moulding. *Rapid Prototyp. J.* **2019**, *25*, 672–678. [CrossRef]
66. Avci, A.; Eker, A.A.; Bodur, M.S.; Candan, Z. Water absorption characterization of boron compounds-reinforced PLA/flax fiber sustainable composite. *Int. J. Biol. Macromol.* **2023**, *233*, 123546. [CrossRef] [PubMed]

Disclaimer/Publisher's Note: The statements, opinions and data contained in all publications are solely those of the individual author(s) and contributor(s) and not of MDPI and/or the editor(s). MDPI and/or the editor(s) disclaim responsibility for any injury to people or property resulting from any ideas, methods, instructions or products referred to in the content.

doi:10.6342/NTU202502722

molecules

MDPI

Article

Foaming of Bio-Based PLA/PBS/PBAT Ternary Blends with Added Nanohydroxyapatite Using Supercritical CO_2: Effect of Operating Strategies on Cell Structure

Pei-Hua Chen [1,2], Chin-Wen Chen [3,*], Tzu-Hsien Chan [3], Hsin-Ying Lin [3], Ke-Ling Tuan [3], Chie-Shaan Su [4], Jung-Chin Tsai [5] and Feng-Huei Lin [1,*]

[1] Department of Biomedical Engineering, National Taiwan University, Taipei 106319, Taiwan; d10528004@ntu.edu.tw or 16185@s.tmu.edu.tw
[2] Department of Orthopedics, Shuang Ho Hospital, Taipei Medical University, New Taipei City 235041, Taiwan
[3] Department of Molecular Science and Engineering, Institute of Organic and Polymeric Materials, National Taipei University of Technology, Taipei 106344, Taiwan; aa523383@gmail.com (T.-H.C.); barbie900608@gmail.com (H.-Y.L.); t110350011@ntut.org.tw (K.-L.T.)
[4] Department of Chemical Engineering and Biotechnology, National Taipei University of Technology, Taipei 106344, Taiwan; cssu@ntut.edu.tw
[5] Department of Chemical Engineering, Ming Chi University of Technology, New Taipei City 243303, Taiwan; jctsai@mail.mcut.edu.tw
* Correspondence: cwchen@ntut.edu.tw (C.-W.C.); double@ntu.edu.tw (F.-H.L.)

Abstract: This study explored the innovative foaming behavior of a novel biodegradable polymer blend consisting of polylactic acid/poly(butylene succinate)/poly(butylene adipate-co-terephthalate) (PLA/PBS/PBAT) enhanced with nanohydroxyapatite (nHA), using supercritical carbon dioxide ($SCCO_2$) as an environmentally friendly physical foaming agent. The aim was to investigate the effects of various foaming strategies on the resulting cell structure, aiming for potential applications in tissue engineering. Eight foaming strategies were examined, starting with a basic saturation process at high temperature and pressure, followed by rapid decompression to ambient conditions, referred to as the (1T-1P) strategy. Intermediate temperature and pressure variations were introduced before the final decompression to evaluate the impact of operating parameters further. These strategies included intermediate-temperature cooling (2T-1P), intermediate-temperature cooling with rapid intermediate decompression (2T-2P), and intermediate-temperature cooling with gradual intermediate decompression (2T-2P, stepwise ΔP). SEM imaging revealed that the (2T-2P, stepwise ΔP) strategy produced a bimodal cell structure featuring small cells ranging from 105 to 164 μm and large cells between 476 and 889 μm. This study demonstrated that cell size was influenced by the regulation of intermediate pressure reduction and the change in intermediate temperature. The results were interpreted based on classical nucleation theory, the gas solubility principle, and the effect of polymer melt strength. Foaming results of average cell size, cell density, expansion ratio, porosity, and opening cell content are reported. The hydrophilicity of various foamed polymer blends was evaluated by measuring the water contact angle. Typical compressive stress–strain curves obtained using DMA showed a consistent trend reflecting the effect of foam stiffness.

Keywords: PLA/PBS/PBAT/nHA polymer blend; supercritical CO_2; foaming strategy; bimodal cell structure

Received: 30 March 2025
Revised: 26 April 2025
Accepted: 30 April 2025
Published: 5 May 2025

Citation: Chen, P.-H.; Chen, C.-W.; Chan, T.-H.; Lin, H.-Y.; Tuan, K.-L.; Su, C.-S.; Tsai, J.-C.; Lin, F.-H. Foaming of Bio-Based PLA/PBS/PBAT Ternary Blends with Added Nanohydroxyapatite Using Supercritical CO_2: Effect of Operating Strategies on Cell Structure. *Molecules* **2025**, *30*, 2056. https://doi.org/10.3390/molecules30092056

Copyright: © 2025 by the author. Licensee MDPI, Basel, Switzerland. This article is an open access article distributed under the terms and conditions of the Creative Commons Attribution (CC BY) license (https://creativecommons.org/licenses/by/4.0/).

doi:10.6342/NTU202502722

1. Introduction

Tissue engineering has developed rapidly in the past four decades, with the goal of achieving the regeneration of human tissues or organs. Biomaterial scaffolds are important to multidisciplinary tissue engineering research [1–3]. Appropriately engineered tissues are being implanted in patients clinically [3–5]. Porous biomaterials are extremely useful in medical applications, where the cell structure, porosity, and interconnectivity are important for the functionality and biocompatibility of the tissue matrix. Voids in the material facilitate tissue growth and outward nutrient and waste mass transfer. Appropriate cell structures and porosities vary with tissue-specific biomaterials [6–8]. Porous biomaterials have a wide range of medical applications in subcutaneous tissue, bone, cardiovascular system, brain, eyes, etc., and have been reviewed in recent literature [9–14]. Biomaterials are generally divided into natural materials, metals and alloy materials, ceramic materials, polymer materials, and composite materials, each of which has its advantages and disadvantages [3,5,11,15,16]. Currently, metal-based or ceramic-based implant materials are mainly used. Polymer-based materials and their composites are more viable in the future due to their tunable, biodegradable properties and processing capabilities [17,18].

According to recent literature reports, biodegradable materials have important clinical indications, including drug delivery, tissue engineering, medical imaging, vaccine carriers, biosensing, fracture fixation, ligament reconstruction, and meniscal repair [19,20]. The synthetic biodegradable polymers most investigated are poly(ε-caprolactone) (PCL), polylactic acid (PLA), polyglycolic acid (PGA), and the copolymer of PLA and PGA [21,22]. PLA is a semi-crystalline polymer approved by the U.S. Food and Drug Administration (FDA) with desired biocompatibility and biodegradability [22]. In order to improve the shortcomings of PLA, such as toughness, hydrophilicity, and cell affinity, previous literature has studied composites of PLA with other bio-based polymers or inorganic additives. The morphology, microstructure, thermal properties, and mechanical properties of PLA with poly(butylene succinate) (PBS) or PLA with poly(butylene adipate-co-terephthalate) (PBAT) polymer blends have been studied in previous reports as potential scaffold materials in tissue engineering [23–29]. Inorganic bioactive materials are added to polymer blends to achieve the necessary infrastructure. For example, hydroxyapatite (HA) or nanohydroxyapatite (nHA) are major components of human bone tissue and are added to various polymer blends [30,31].

According to the literature we are aware of, most polymer scaffold materials are binary bio-based polymer blends (e.g., PLA/PBS or PLA/PBAT) or single polymers with additives such as nanohydroxyapatite (nHA) particles [24–31]. Some studies on ternary systems (e.g., PLGA/HA/collagen or PLA/PBAT/nHA) have been conducted [30,32], and more hybrid polymer/inorganic systems are expected to emerge. We recently presented thermal, physical, and mechanical studies of a novel bio-based PLA/PBS/PBAT ternary blend with added nHA [33]. Based on our previous study [33], a PLA/PBS/PBAT blend (80/15/5 by weight) with 5 wt% of added nHA met the needs of tissue engineering materials [32]. The thermal and mechanical properties of PLA/PBS/PBAT/nHA blends have been described in our previous study [33]. The added nHA helped increase the hydrophilicity and improve the blend's strength. It was stated in our previous study [33] that the 5 wt% added nHA was uniformly distributed in the polymer blend from the TEM measurement image. This novel bio-based PLA/PBS/PBAT blend with added nHA is a promising tissue engineering material, and the foaming properties of the blend were further investigated in this study.

For tissue engineering applications, porous polymer foams accounted for the most significant market share [34]. The preferred porous material must have an open-cell mor-

doi:10.6342/NTU202502722

phology and interconnected cell structure. Foaming using physical blowing agents, especially carbon dioxide or nitrogen, has received much attention in academic research and industrial applications [35]. The use of supercritical carbon dioxide ($SCCO_2$) for polymer foaming has been reviewed in the literature [34–37]. PLA in porous form is widely used in biomedical applications, and many studies on the use of $SCCO_2$ to form porous PLA or PLA composites have been proposed in the literature [38]. Foaming polymer blends containing semi-crystalline PLA using $SCCO_2$ is complex due to the CO_2-induced crystallization of PLA [39]. Yang et al. [40] presented the foaming of PLA with $SCCO_2$ at a fixed saturation pressure of 16 MPa. A foaming temperature window was proposed according to the crystal structure of PLA. Different cell size and volume expansion ratio distributions were obtained after foaming at different temperatures and pressures. Chen et al. [41] showed a similar foaming temperature window for the foaming behavior of two PLA specimens with different D-isomer contents. A two-step temperature-induced forming process was used. During the first saturation process, $SCCO_2$ was saturated into PLA at 16 MPa and 150 °C for 1 h. The second foaming process was carried out at different forming temperatures, and various foaming results were analyzed to obtain the foaming temperature window. Huang et al. proposed a multiple saturation temperature method under fixed pressure [42]. They reported that in addition to the first stage of high-temperature saturation and cooling procedures, a second stage of heating and cooling was ultimately added to complete rapid decompression foaming. Various operating parameters were discussed to obtain bimodal open-cell PLA with suitable cell size for tissue engineering applications. The foaming of a polymer blend of PLA/PBS using $SCCO_2$ has been presented in the literature, where the PBS phase might act as a heterogeneous nucleation site. Li et al. [43] studied the effects of PBS content and foaming temperature for PLA/PBS at a fixed foaming pressure of 10.3 MPa. The PLA/PBS blend was first heated to a higher temperature of 180 °C to eliminate thermal history and then cooled to a lower temperature for a single-stage foaming process. The temperature and material composition window to obtain open-cell results was demonstrated. A similar melt-saturated foaming strategy proposed by Wang et al. [44] was used to prepare highly expanded open-cell PLA for oil-water separation. Yu et al. studied the effect of adding PBS to PLA-based polymer blends on foaming behavior [27]. The PBS phase with low melt strength helped reduce the viscosity of the blend, and the interface between PLA and PBS acted as a cell nucleation site. It was found that PLA/PBS (80/20 by weight) could produce a highly open cell structure and obtain a bimodal cell size distribution through a two-step pressure reduction process. The foaming of PBAT was studied by Wang et al. [45] using $SCCO_2$ and nitrogen co-blowing agents to improve the shrinkage of PBAT foam through a single decompression process.

The literature has also demonstrated two-step pressure-reduction foaming processes of polymers and their blends with additives [46–48]. The polymer sample was soaked in $SCCO_2$ for a certain saturation time and then depressurized to an intermediate pressure for the first time. After being maintained at the intermediate pressure for a selected holding time, the sample was rapidly depressurized to ambient conditions to complete the foaming process. A bimodal cell size distribution could also be observed through the two-step decompression process. Large cells were obtained during the first slow pressure reduction, and small cells were received during the second rapid depressurization [47,48]. The desired large and small cell sizes for tissue engineering applications were obtained by adjusting the foaming process parameters.

To the best of our knowledge, $SCCO_2$ foaming of PLA/PBS/PBAT ternary polymer blends with added nHA has not been shown in the literature. With the dispersed PBS/PBAT phase in PLA, possible nucleation sites can be expected at the interface between

doi:10.6342/NTU202502722

polymers to facilitate the foaming process. This study aims to investigate the $SCCO_2$ foaming strategy of a recently reported blend of PLA/PBS/PBAT (80/15/5 by weight) with the addition of 5 wt% nHA. The main foaming parameters are the saturation and foaming temperature, pressure, and time. The foaming process included $SCCO_2$ saturation into the polymer matrix, foaming at appropriate temperature and pressure, and finally, rapid decompressing to obtain the desired foamed product. The feasible operating parameters for obtaining bimodal cellular structure porous materials were studied and discussed. The innovation of this study is the foaming of a ternary polymer blend with the addition of nHA, leading to the formation of a bimodal cell structure by employing a gradual pressure reduction process.

2. Results and Discussion

2.1. Foaming Results from Strategies with (1T-1P), (2T-1P), and (2T-2P) Operating Conditions

The role of selecting appropriate operating conditions during the foaming process is significant, especially for PLA-based biodegradable polymer blends. Much previous literature has investigated the foaming temperature and pressure conditions of polymer systems containing mainly PLA. The range of operating conditions was expressed as a foaming window [39–41]. In a recent review article, Sarver and Kiran [35] elaborated on this forming window. As reported in these review articles, the operating temperature range was 100 to 160 °C, and the pressure range was 100 to 200 bar. The simple one-step foaming strategy involves a saturation process of $SCCO_2$ absorption into polymer blends at saturation temperature (T_s) and pressure (P_s), followed by rapid decompression to ambient conditions, which is referred to as the (1T-1P) foaming strategy in this study.

In tissue engineering material research, there is discussion about the bimodal distribution of small and large cells [49,50], and more research on various polymer systems is still in progress. According to the literature, in order to obtain a bimodal distribution during the foaming process, a two-step operation is required by changing the temperature or pressure [27,42,46,47,51,52]. In the two-step process, variable temperature operation is the most common in the literature due to the important influence of temperature on polymer crystal formation and melt strength changes. The polymer or its blend was heated to a higher saturation temperature (T_s) and pressure (P_s), and maintained in the saturated state for a particular saturation time (t_s). This step allowed $SCCO_2$ to be absorbed into the polymer matrix. The system was then reduced to an intermediate or foaming temperature (T_f) and held for a certain holding or foaming time (t_f) before being rapidly depressurized from P_s to ambient conditions to complete the batch foaming process. This study refers to this as the (2T-1P) foaming strategy. If the operating pressure P_s dropped rapidly to an intermediate pressure level, i.e., the foaming pressure (P_f), within the foaming time interval (t_f) before the final rapid pressure release, we call it a (2T-2P) foaming strategy in this study.

In previous literature (PLA/PBS, the weight ratio of 80/20) [27], the saturation temperature (T_s) used was 150 °C. It is also noticed that at higher T_s above 160 °C, the melt strength of PLA was insufficient to withstand the internal pressure during the absorption process [41]. Therefore, the saturation temperature T_s in this study was selected as 150 °C. Based on the solubility data of $SCCO_2$ in biodegradable polymers measured in previous literature [53–55], the saturation time (t_s) was selected as 90 min, at which the CO_2 uptake in the PLA-based blends in this study was estimated to be close to equilibrium. This saturation time is reasonable compared to the values used in previous literature [40,41,56–58]. Firstly, the (1T-1P) foaming strategy was adopted, and the experiments were carried out at a saturation temperature of 150 °C and saturation pressures of 130, 150, and 170 bar. Based on these preliminary results, the highest expansion ratio can be obtained when the

doi:10.6342/NTU202502722

saturation pressure (P_s) was selected as 150 bar, and it is reasonable to set P_s as 150 bar in this study.

Figure 1 shows the operating conditions for three foaming strategies and their resulting SEM images: (A) one-step (1T-1P) process, (B) two temperature levels (2T-1P) process with intermediate cooling to 110 °C, holding time was 10 min, and (C) two temperature levels and two pressure levels (2T-2P) process, with intermediate temperature cooling to 110 °C and intermediate rapid pressure reduction from 150 to 100 bar. The intermediate pressure at 100 bar was selected based on the foaming window shown in the literature [35]. The intermediate temperature at 110 °C chosen in this study is reasonable, which is about the middle temperature in the previously reported foaming window [40,41]. A foaming time t_f of 10 min was used in the (2T-1P) and (2T-2P) strategies.

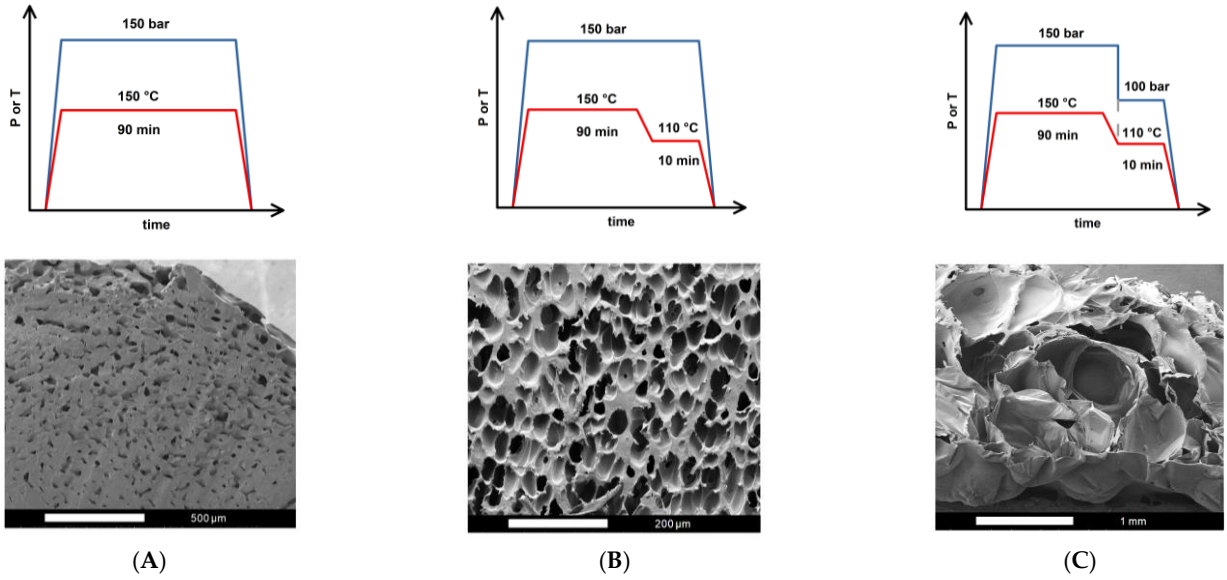

Figure 1. Operating conditions and SEM images for foaming strategies: (**A**) Strategy A with one-step (1T-1P) process, (**B**) Strategy B with two temperature levels (2T-1P) process, with intermediate cooling to 110 °C, and (**C**) Strategy C with two temperature levels and two pressure levels (2T-2P) process, with intermediate cooling to 110 °C and intermediate rapid pressure reduction to 100 bar.

From the SEM observation of the (1T-1P) foaming strategy A, it is evident that the foamed product contained sparsely distributed small cells, while a significant portion of the sample remained unfoamed. This outcome suggests that during the (1T-1P) foaming process, only a small amount of absorbed CO_2 underwent nucleation to form small bubbles during the rapid pressure drop, leaving behind a large unfoamed region. The defining feature of the (1T-1P) strategy is its isothermal operation, meaning that the polymer blend absorbed CO_2 at a single elevated temperature and then initiated foaming by a sudden release of pressure to ambient conditions. However, due to the lack of a second temperature zone to adjust the melt strength and foaming ability, the PLA/PBS/PBAT/nHA blend could not form a large or bimodal cell structure. This limitation is particularly critical for polymer blends, where achieving a well-defined porous structure depends on carefully controlling both temperature and pressure conditions. Without an additional temperature change stage, the melt strength remained inappropriate to support stable bubble growth, leading to the unsatisfactory formation of only small cells with an average size of 27.6 µm using strategy A.

The (2T-1P) foaming strategy B shown in Figure 1 included an additional temperature cooling (from 150 to 110 °C) and holding at 110 °C for 10 min. During the cooling and holding process, bubbles nucleated and presented an unimodal cell structure after rapid

doi:10.6342/NTU202502722

decompression. With foaming strategy B, no large cells were detected from the SEM images. This may be because the nucleation energy barrier was not overcome within the holding time to induce the nucleation and cell growth. Only during the final rapid decompression step did relatively short nucleation and small-cell formation occur [59,60]. Small cells with an average size of 34.2 μm were obtained through foaming strategy B. To obtain both small and large cells for tissue engineering applications, consideration of two-step pressure manipulation was further investigated.

The (2T-2P) foaming strategy C shown in Figure 1 included temperature cooling (from 150 to 110 °C) and holding at 110 °C for 10 min. As the temperature reached 110 °C, the pressure was quickly reduced from 150 to 100 bar and held in this intermediate pressure for 10 min before final rapid depressurization to ambient conditions. This foaming strategy produced mainly large cells with an average size of 408.7 μm and a lower cell density. The cell size and structure produced by strategy C are completely different from those by strategy B, mainly due to a rapid, intermediate pressure drop from 150 to 100 bar. According to classical nucleation theory [48,61], the free energy barrier for nucleation is inversely proportional to the square of pressure supersaturation, which is defined as the difference between the critical bubble pressure and the operating pressure. When the operating pressure was quickly reduced by 50 bar, it is possible that excessive cell nucleation was induced during the quick, intermediate decompression and a high degree of cell growth during the holding time, resulting in almost no small cell size during the final rapid decompression to ambient conditions. SEM images showed large cells, indicating excessive expansion of the bubbles and possible coalescence. This result expresses that larger cells can be obtained through a two-step depressurization operation, but the degree of the intermediate depressurization and the time of holding the intermediate pressure should be adjusted to obtain a bimodal cell structure.

Figure 2 plots the relative frequency of cell size distribution for three foaming strategies A, B, and C. It shows that unimodal cell structures were obtained from these three strategies. This study observed that the (1T-1P) foaming strategy A had a lower expansion ratio of 1.36 and a smaller cell size. The (2T-1P) foaming strategy B increased the expansion ratio to 2.72, but the cell size was still small. The (2T-2P) foaming strategy C, which changed both temperature and pressure in the intermediate stage, produced almost all large cells with a higher expansion ratio of 5.41. The intermediate pressure change is beneficial for obtaining larger cells, but a gradual pressure change might be needed to get desirable bimodal cell structure products.

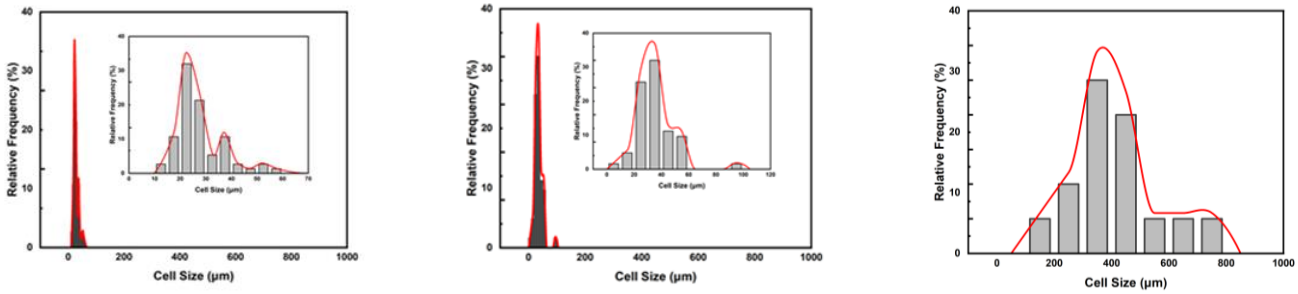

(**A**) (**B**) (**C**)

Figure 2. Plots of the relative frequencies of cell size distribution results for foaming strategies: (**A**) Strategy A with one-step (1T-1P) process, (**B**) Strategy B with two temperature levels (2T-1P) process, with intermediate cooling to 110 °C, and (**C**) Strategy C with two temperature levels and two pressure levels (2T-2P) process, with intermediate cooling to 110 °C and intermediate rapid pressure reduction to 100 bar.

doi:10.6342/NTU202502722

2.2. Foaming Results from Strategies with (2T-2P, Stepwise ΔP) Operating Conditions: Pressure Effect

Based on the three foaming strategies discussed above, the temperature change process accompanied by a stepwise decrease in pressure (2T-2P, stepwise ΔP) was further investigated. Figure 3 shows a schematic diagram of the (2T-2P, stepwise ΔP) foaming strategy. The saturation pressure and temperature remained at 150 bar and 150 °C, respectively. The saturation time was maintained at 90 min to ensure sufficient absorption of CO_2 into the polymer blends. After the saturation stage, the operating temperature drops to an intermediate value (T_f) (or the foaming temperature) and remains there for a holding time (t_f). During this holding time, the operating pressure was gradually reduced from 150 bar to an intermediate value (P_f) (or the foaming pressure), with each pressure reduction step being 10 bar min^{-1}. With the gradual change in pressure, a porous product with a bimodal cell structure is expected to be obtained, in which large cells are formed during the intermediate holding time, and small cells are formed during the final rapid decompression step [27,46–48].

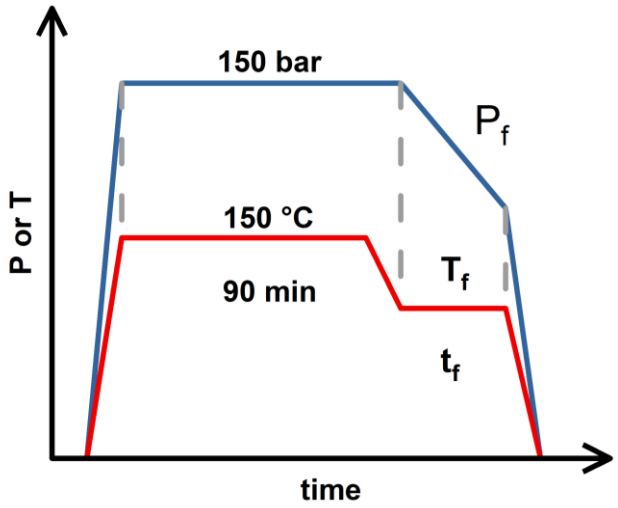

Figure 3. The schematic diagram for operating conditions of the (2T-2P, stepwise ΔP) foaming strategy.

Firstly, the effect of foaming pressure (P_f) was studied, where the foaming temperature (T_f) was maintained at 110 °C. Three (2T-2P, stepwise ΔP) foaming strategies were investigated based on different intermediate pressure effects: (D) stepwise pressure drop to 120 bar with a holding time (t_f) of 3 min, (E) stepwise pressure drop to 100 bar with a holding time of 5 min, and (F) stepwise pressure drop to 80 bar with a holding time of 7 min. Figure 4 shows the SEM images and relative frequencies of cell size distribution obtained for the three foaming strategies: D, E, and F.

doi:10.6342/NTU202502722

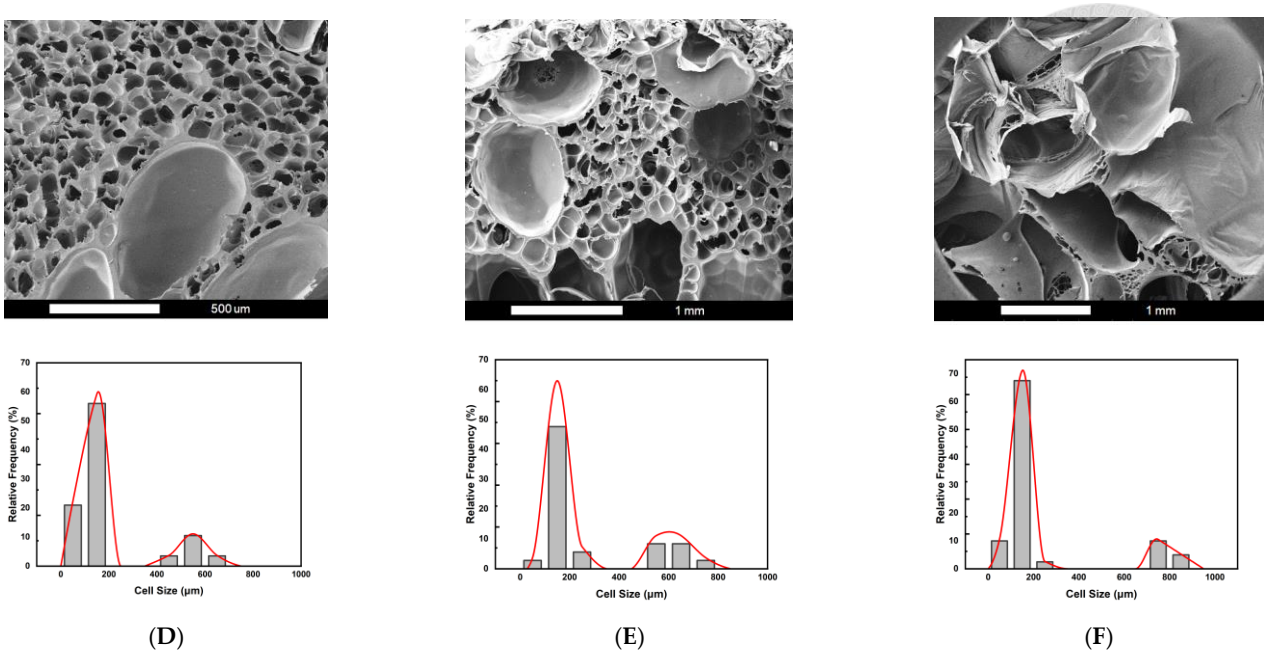

(**D**) (**E**) (**F**)

Figure 4. The SEM images and relative frequencies of cell size distribution results for (2T-2P, stepwise ΔP) foaming strategies: (**D**) Strategy D with stepwise pressure drop to 120 bar and with a holding time of 3 min, (**E**) Strategy E with stepwise pressure drop to 100 bar and with a holding time of 5 min, and (**F**) Strategy F with stepwise pressure drop to 80 bar and with a holding time of 7 min.

It is observed that bimodal cell structures were obtained with the (2T-2P, stepwise ΔP) foaming processes. Generally speaking, the average small cell size ranged from 110 to 160 μm for the three foaming strategies: D, E, and F. However, the average large cell size depended on the degree of pressure change. Both the operating temperature and pressure have an important influence on the cell size and structure. For foaming strategies D, E, and F, the intermediate temperature (T_f) was maintained constant at 110 °C. The effects of the remaining operating parameters, namely the degree of pressure variation and the foaming time (t_f), are discussed below.

For these three foaming strategies at the same intermediate temperature, as the pressure decreased in the intermediate foaming stage, the solubility of $SCCO_2$ in the polymer becomes smaller, resulting in the gradual release of gas from the polymer matrix. When CO_2 escaped, it created a supersaturated state, which caused bubbles to form. The extent of the pressure drop affected the number and size of bubbles. The pressure drop extent of foaming strategy D was the smallest among the three pressure reduction strategies, and the resulting average large cell size was also the smallest, about 562 μm.

This result is consistent with the classical nucleation theory, where the maximum free energy barrier related to forming a new phase is inversely proportional to the square of pressure supersaturation. Cell nucleation and growth occurred during the time when the pressure was gradually reduced. The pressure drop of 30 bar in foaming strategy D lasted for 3 min, which was insufficient to allow the growing nuclei to form larger cell sizes compared to the other two foaming strategies, E and F, with longer foaming times. If a larger cell size is desired, the degree of pressure drop should be increased.

The results of foaming strategy E show that when the intermediate pressure was reduced to 100 bar and the foaming time was extended to 5 min, larger cells could be obtained, and the average cell size was about 602 μm. The results for strategy F showed a gradual pressure drop to 80 bar over a period of 7 min, with an average large cell size of 775 μm. A pressure drop of 70 bar in foaming strategy F might reduce the nucleation barrier to a low enough level to result in the growth of large cells. Examining the pressure effects shown in Figure 4, it can be noted that intermediate stepwise pressure drops can

doi:10.6342/NTU202502722

adjust the desired cell size and bimodal cell structure. Various cell sizes might be required for different applications in tissue engineering [6]. For example, bimodal cell structure is advantageous for bone tissue engineering scaffolds, and large cell sizes up to 800 μm still contribute to bone formation [62]. Figure 5 plots the average large cell sizes for foaming strategies D, E, and F. It supplies a guideline for choosing the operating pressure condition to obtain desired bimodal cell structures.

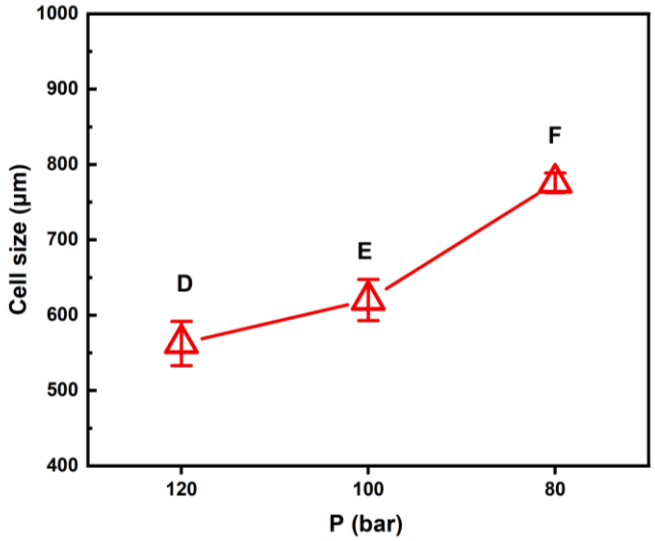

Figure 5. Effect of the foaming pressure on the large cell size obtained from foaming strategies D, E, and F.

2.3. Foaming Results from Strategies with (2T-2P, Stepwise ΔP) Operating Conditions: Temperature Effect

The effect of foaming temperature (T_f) was further examined, with the foaming pressure (P_f) gradually reduced from 150 to 100 bar, as described in Section 2.2 under foaming strategy E. Three variations of the (2T-2P, stepwise ΔP) foaming strategy were investigated, each with a different intermediate or foaming temperature (T_f): (G) T_f set at 100 °C, (E) T_f set at 110 °C, and (H) T_f set at 120 °C. The foaming time (t_f) was maintained at 5 min for all three strategies. Figure 6 presents the SEM images and corresponding cell size distribution frequencies for strategies G, E, and H. Under the same foaming pressure conditions, temperature emerged as a critical factor influencing the solubility and diffusivity of supercritical CO_2 within the polymer blend. It also affected the molecular chain mobility and melt strength during the foaming process [52,63], ultimately impacting the resulting cell structure.

doi:10.6342/NTU202502722

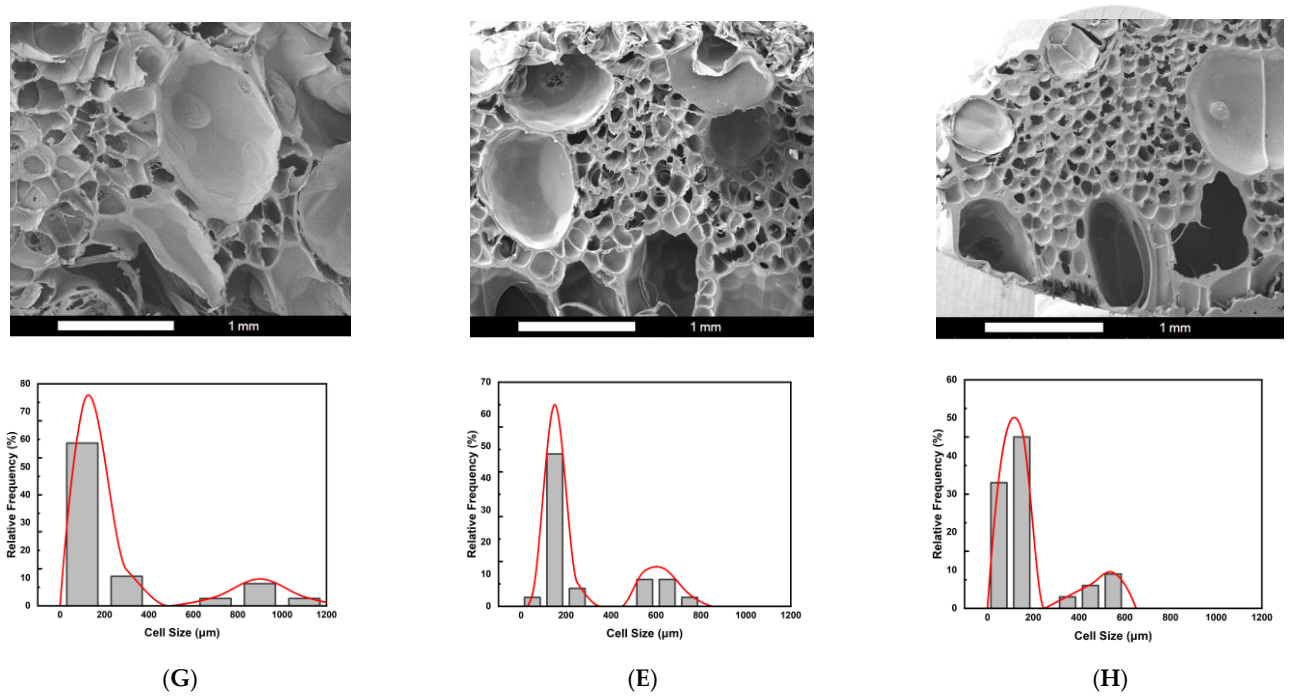

(**G**) (**E**) (**H**)

Figure 6. The SEM images and relative frequencies of cell size distribution results for (2T-2P, stepwise ΔP) foaming strategies: (**G**) Strategy G with intermediate temperature at 100 °C, (**E**) Strategy E with intermediate temperature at 110 °C, and (**H**) Strategy H with intermediate temperature at 120 °C.

It was observed that all three foaming strategies produced a bimodal cell structure, with average small cells ranging from 105 to 164 μm. However, the average large cell sizes varied under each foaming temperature condition. All three temperatures fell within the foaming window of PLA, as reported in previous studies [39–41], making them suitable for foaming the PLA-based blends in this study. For strategies G, E, and H, the results show a decreasing trend in macrocell size as the foaming temperature changed from 100 °C to 120 °C. This trend can be attributed to the changes in $SCCO_2$ solubility within the PLA-based blends of this study and the effects on the melt strength of these blends.

Foaming strategy G, operated at a foaming temperature (T_f) of 100 °C, produced the largest average macrocell size of 889 μm among the three strategies. This result can be explained first by gas solubility. In strategy G, the larger temperature drop from the high saturation temperature to the lower foaming temperature resulted in a higher gas density, increasing the solubility of $SCCO_2$ in the polymer blend. During stepwise decompression, higher $SCCO_2$ contents led to greater supersaturation, generally promoting larger cell formation. In addition to $SCCO_2$ solubility, the melt strength of the polymer blend played an important role. According to the literature [52], sufficient melt viscosity can stabilize cell growth. At 100 °C, the polymer blend exhibited relatively higher melt strength than those at the other two foaming temperatures, which benefited the bubble expansion and, thus, the formation of larger macrocells. This explains the result observed with strategy G, where the combination of melt strength effect and stepwise pressure reduction created a favorable environment for large cell growth, ultimately producing a bimodal cell structure after the final decompression.

Foaming strategies E and H were conducted at higher foaming temperatures (T_f) of 110 °C and 120 °C, respectively. This resulted in a smaller temperature drop from the initial saturation temperature compared to strategy G. The smaller temperature drop maintained the $SCCO_2$ density lower than that of strategy G. The lower solubility of $SCCO_2$ may have resulted in the reduction in the macrocell size compared to the 100 °C condition. Additionally, the melt strength of the polymer blend decreased at these higher foaming

doi:10.6342/NTU202502722

temperatures. During the final rapid cooling and sudden drop in pressure to ambient conditions, the melt strength of the polymer blend increased again. As reported in the literature [40,64], the sudden increase in melt strength might promote the retraction of polymer chains, leading to bubble shrinkage and further reducing the final macrocell size. As shown in Figure 6, the average macrocell sizes for foaming strategies E and H were 602 μm and 476 μm, respectively. A graphical illustration of the decreasing trend of the average macrocell size from strategies G, E, and H is shown in Figure 7.

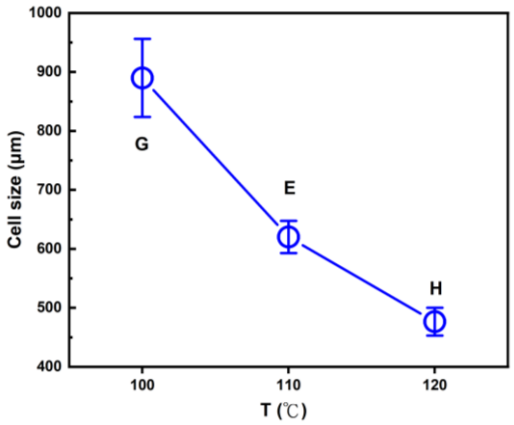

Figure 7. Effect of the foaming temperature on the large cell size obtained from (2T-2P, stepwise ΔP) foaming strategies G, E, and H.

2.4. Comparison of Foaming Results from All Operating Strategies in This Study

The experimental results of all foaming strategies in this study are summarized in Table 1. It was observed that foaming strategies A and B produced only small cells with relatively low expansion ratios (less than 3) and high cell densities. The opening cell contents of foaming strategies A and B are lower because the operating pressure drops too quickly, resulting in larger unfoamed spaces and more closed cells. When applying foaming strategy C involving a rapid, intermediate pressure drop of 50 bar, only large cells with an increased expansion ratio of up to 5.41 were obtained. The opening cell content increased to 67.8, possibly due to cell coalescence when the cells grew to a large size.

Table 1. Summarized foaming results from all operating strategies in this study.

Operating Strategy	Expansion Ratio	Porosity (%)	Cell Density (cell/cm^3)	Cell size (μm) (Small/Large)	Opening Cell Content (%)
A	1.36 ± 0.08	26.5 ± 4.4	(1.75 ± 0.17) × 10^7	27.6 ± 1.1/—	12.7 ± 2.2
B	2.72 ± 0.21	65.2 ± 2.8	(1.89 ± 0.05) × 10^7	34.2 ± 1.9/—	45.0 ± 1.5
C	5.41 ± 0.40	81.5 ± 1.4	(1.64 ± 0.02) × 10^4	—/408.7 ± 38.7	67.8 ± 0.5
D	4.30 ± 0.02	76.7 ± 0.1	(1.05 ± 0.01) × 10^6	109.9 ± 3.2/562.0 ± 29.4	60.0 ± 1.2
E	7.29 ± 0.30	86.3 ± 0.5	(3.24 ± 0.01) × 10^5	164.2 ± 8.4/602.1 ± 27.3	66.9 ± 0.7
F	14.01 ± 0.93	92.9 ± 0.4	(5.86 ± 0.02) × 10^5	138.2 ± 5.4/775.6 ± 13.0	77.8 ± 0.6
G	17.96 ± 0.20	94.4 ± 0.1	(3.27 ± 0.01) × 10^5	151.1 ± 12.1/889.8 ± 66.2	84.3 ± 0.4
H	4.48 ± 0.16	77.7 ± 0.7	(1.06 ± 0.01) × 10^6	105.9 ± 5.1/476.4 ± 23.6	57.8 ± 1.2

The remaining five foaming strategies all resulted in bimodal cell distribution, which is advantageous in tissue engineering and regenerative medicine applications. Comparing foaming strategies D, E, and F, the expansion ratios increased from 4.3 to 14.0 as the intermediate pressure drop increased. The macrocellular size (from 562 ± 29.4 to 775 ± 13.0 μm) and opening cell content (from 60.2 ± 1.2 to 77.8 ± 0.6%) also showed an increasing trend. Larger cells indicate that the bubbles may have merged during the expansion process, forming interconnected cells and leading to higher opening cell content. The macrocell

doi:10.6342/NTU202502722

sizes obtained from strategies G and H showed their dependence on the intermediate foaming temperature. In this study, the largest macrocell size of the foamed product prepared by strategy G at the intermediate temperature of 100 °C was 889.8 ± 66.2 μm, and the highest opening cell content was 84.3 ± 0.4%. Foaming strategy H, which was operated at a higher intermediate foaming temperature of 120 °C, had a smaller macrocell size of 476.4 ± 23.6 μm and a smaller opening cell content of 57.8 ± 1.2% compared to strategy G.

The graphical presentations of the large and small cell sizes, cell densities, expansion ratios, and porosities, and opening cell contents of the foamed polymer blends in this study using various foaming strategies are illustrated in Figure 8a–d, respectively. It is demonstrated that with the stepwise pressure drop in the intermediate stage of the foaming process, bimodal cell structures can be achieved with porosity ranging from 76.7% to 94.4% and opening cell content from 57.8% to 84.3%. These data suggest that this study's foamed polymer blends are suitable for bioscaffold use in tissue engineering [5,6,13].

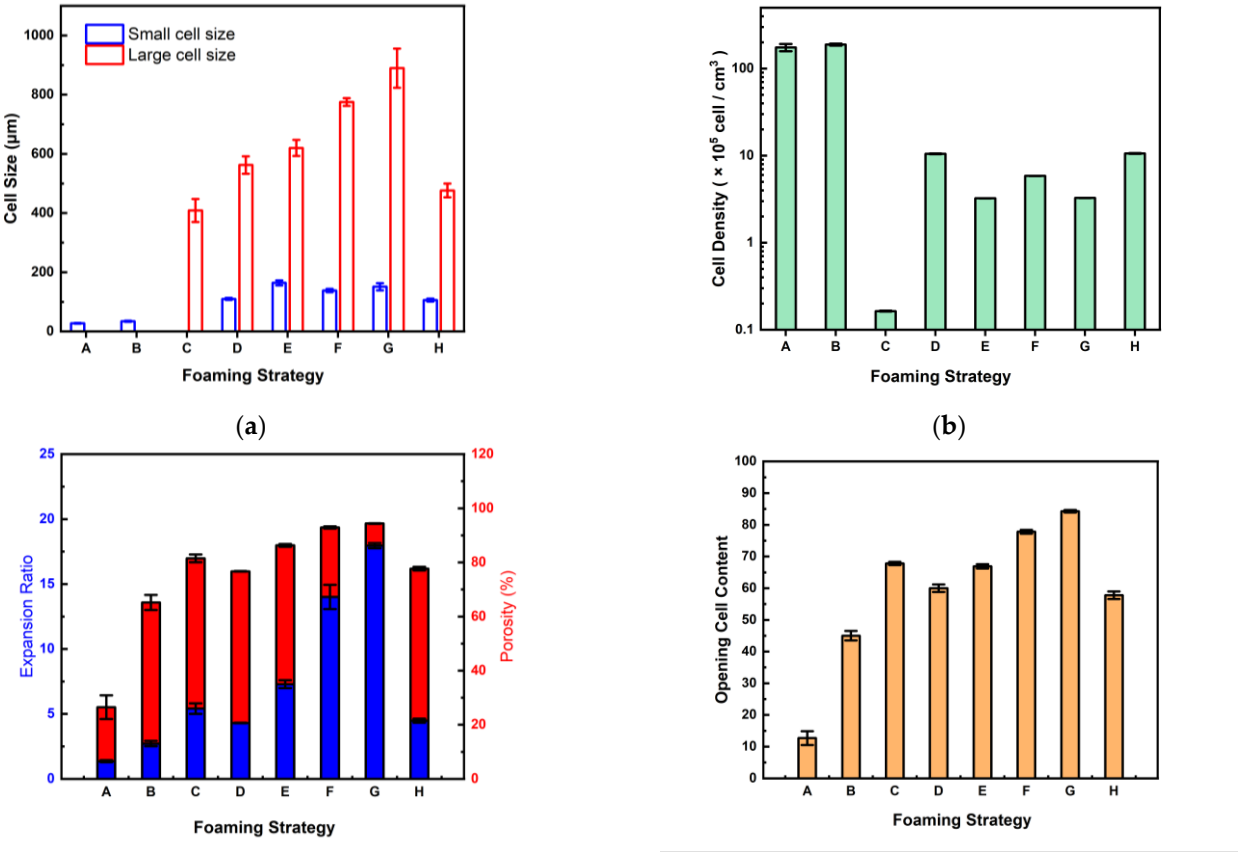

Figure 8. The experimental results of (**a**) cell size, (**b**) cell density, (**c**) expansion ratio and porosity, and (**d**) opening ratio of the foamed polymer blend in this study using various foaming strategies from A to H.

The water contact angle measurements demonstrate the hydrophilicity of the foamed polymer blends produced using various foaming strategies. Figure 9 presents a representative water contact angle result for the blend processed with foaming strategy E. The initial water contact angle was recorded as 68.5 ± 0.2°, gradually decreasing to 50.7 ± 0.1° after 30 min. In comparison, the contact angle of the unfoamed PLA/PBS/PBAT/nHA blend was 87.5 ± 1.0°, which was close to the hydrophobic nature. These results indicate that the bimodal cell structure achieved through foaming strategy E expressed enhanced hydrophilicity. Similarly, all other foamed products with a bimodal structure displayed a

doi:10.6342/NTU202502722

comparable trend in hydrophilicity, attributed to the formation of large open cells that facilitated water absorption.

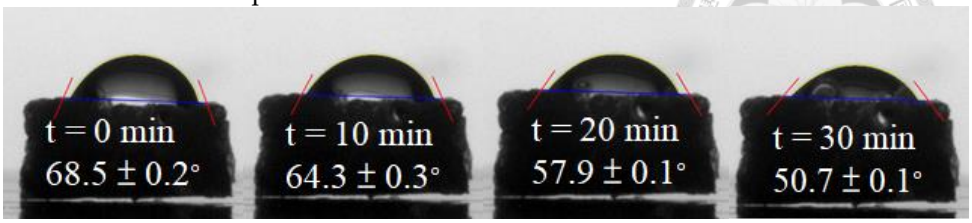

Figure 9. The water contact angle of the foamed polymer blend using foaming strategy E.

The decreased behavior of the water contact angle with time is discussed below for the foamed polymer blends treated using the (2T-2P, stepwise ΔP) foaming strategies described in Sections 2.2 and 2.3. All of these foams had a bimodal cell structure, and the results show that the foamed products with larger macrocells had lower water contact angles. For example, as shown in Figure 10a, the initial water contact angles of the foamed products from strategies D, E, and F were 76.0°, 68.5°, and 54.4°, respectively. This is because strategy F produced the foamed products with larger macrocells and a larger opening cell content than the foamed products produced by strategies D and E. After a period of 30 min, the water contact angle of the foamed product produced by strategy F decreased to 27.4°, which was lower than the water contact angles of the foamed products produced by strategies D and E (61.4° and 50.7°, respectively). Figure 10b shows similar trends for the foamed products prepared using strategies G, E, and H. The decreasing water contact angle curves shown in Figure 10a,b highlight the enhanced hydrophilicity of the bimodal foamed products due to interconnected macrocells.

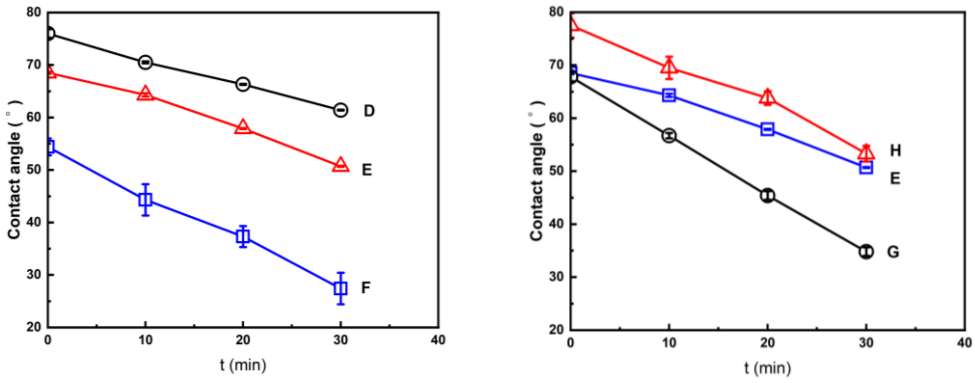

Figure 10. The decreasing trend of water contact angle for the foamed polymer blends from (**a**) foaming strategies D, E, and F; (**b**) foaming strategies G, E, and H.

Figure 11 shows the DMA measurement results of the foamed products processed using the (2T-2P, stepwise ΔP) foaming strategy described in Sections 2.2 and 2.3. All foamed products had a bimodal structure. Figure 11a presents the compressive stress–strain curves of the foamed products produced using foaming strategies D, E, and F. The strain data were recorded using dynamic mechanical analyzer (DMA, 7e, Perkin Elmer, Waltham, MA, USA) at a constant increasing load stress rate of 10 kPa min^{-1}, starting from 7 kPa up to 1.13 MPa. The foamed product from strategy F displayed a greater strain value under fixed compressive stress than those from strategies D and E. This is consistent with the increasing trend of average macrocell size obtained from these strategies. Specifically, the foamed product from strategy D had a compressive stress of 0.76 MPa at 5% strain. For the foamed products from strategies E and F, at the same 5% strain value, the corresponding compressive stress dropped to 0.45 MPa and 0.12 MPa, respectively. These

doi:10.6342/NTU202502722

results indicate that the foamed product with smaller macrocells using strategy D exhibited higher stiffness, whereas the foamed products with increasing macrocell sizes using strategies E to F exhibited better toughness. Figure 11b shows a similar trend for the foamed products produced using strategies G, E, and H, indicating that the foamed product using foaming strategy H (with macrocell size of 476.4 ± 23.6 μm) exhibited higher stiffness. In contrast, the foamed product prepared using foaming strategy G (with a macrocell size of 889.8 ± 66.2 μm) exhibited enhanced toughness.

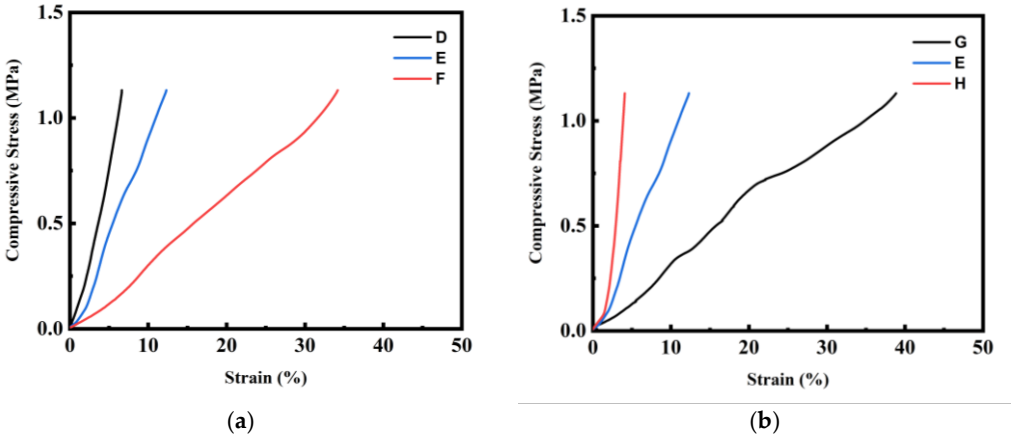

Figure 11. The compressive stress–strain curves for the foamed polymer blends from (**a**) foaming strategies D, E, and F; (**b**) foaming strategies G, E, and H.

3. Materials and Methods

3.1. Material

The materials used in this study are the same as those in our previous research [33], and according to the supplier, the main physical properties of these materials are as follows. Polylactic acid (PLA, Ingeo 4032D), with an average D-lactide content of PLA of 1.4 wt%, was purchased from NaturalWorks LLC, Minnetonka, MN, USA. The melting temperature of PLA is 155–170 °C, and its melt flow index (at 190 °C and 2.16 kg) is 7 g/10 min. Poly(butylene succinate) (Bio PBS, FZ 91) was purchased from PTT MCC Biochem Co. Ltd., Bangkok, Thailand. The melting temperature of PBS is 115 °C, and its melt flow index (at 190 °C and 2.16 kg) is 5 g/10 min. Poly(butylene adipate-co-terephthalate) (PBAT, ecoflex F blend C1200) was purchased from BASF SE, Ludwigshafen, Deutschland. The melting temperature of PBAT is 110–120 °C, and its melt flow index (at 190 °C and 2.16 kg) is 2.7–4.9 g/10 min. Nano-hydroxyapatite (nHA, CAS registry number 12167-74-7) was purchased from Sigma-Aldrich, UNI-ONWARD Corp, Taiwan. The purity of nHA is greater than 97 wt%, with a mean particle size of 72–80 nm, molecular weight of 502.3, and a melting temperature of about 1100 °C.

3.2. Preparation of Composite Blends

The polymer blends (PLA/PBS/PBAT) added with nHA were prepared using a twin-screw extruder (Process 11, Thermo Fisher Scientific, Waltham, MA, USA). All PLA, PBS, and PBAT polymers were first dried in a vacuum oven (Channel, VO45L, KO TSAO specialty Instrument & Supplies Co. Ltd, Taipei, Taiwan) at 80 °C for 6 h before charging into the extruder. The formulation of the blends PLA/PBS/PBAT used in this study is 80/15/5 in weight percentage, added with an additional 5 wt% nHA. The extruder for blending the polymers was equipped with a volumetric feeder and a strand pelletizer (Process 11, Thermo Fisher Scientific, Waltham, MA, USA). The diameter of the screw extruder is 11 mm, and the L/D ratio is 40. Polymers were fed into the hopper of the extruder, where the

doi:10.6342/NTU202502722

extrusion temperatures were controlled independently. The feed rate of the polymer pellets was 1 kg h^{-1}, and the screw speed was 50 rpm. The temperature settings for the feed and mixing zones were 220–225–225–225–225–220–210–200 °C. After the blending process, the extruded products were cooled by a water bath and were then granulated and dried for a sufficient time. Rectangular specimens with 3 mm × 7 mm and thickness of 2 mm were made by compression molding at 200 °C for 5 min, followed by cooling to room temperature. The specimens were packed in plastic bags and stored in cool surroundings before the foaming experiments.

3.3. Saturation and Foaming Steps

Saturation and foaming steps were included to obtain a porous structure of the polymer blend. Supercritical CO_2 diffused into the polymer blend at high pressure (saturation pressure, P_s) and high temperature (saturation temperature, T_s) with a saturation time of t_s. The foaming stage involved changes in intermediate temperature and pressure, namely, foaming temperature (T_f), foaming pressure (P_f), and foaming time (t_f), and finally, rapid decompression to ambient conditions to obtain the final foamed product. A schematic diagram for the foaming process of the PLA/PBS/PBAT/nHA samples in this study is shown in Figure 12. The polymer blend sample was put into a high-pressure vessel (Applied Separations 70770, Allentown, PA, USA). The chamber was placed inside a self-made electric heater with an openable cover and temperature controller. The uncertainty of temperature was ± 2 °C in this study. The chamber was purged with low-pressure CO_2 for 5 min to remove any air inside. The chamber was heated to the desired temperature by the electric heater and pressurized to the operating pressure using an ISCO 260D syringe pump (Teledyne Technologies, Lincoln, NE, USA). This study emphasized investigating various strategies of saturation and foaming of the PLA/PBS/PBAT polymer blends added with nHA. The detailed temperature and pressure operating parameters for various foaming strategies are listed in the results and discussion section.

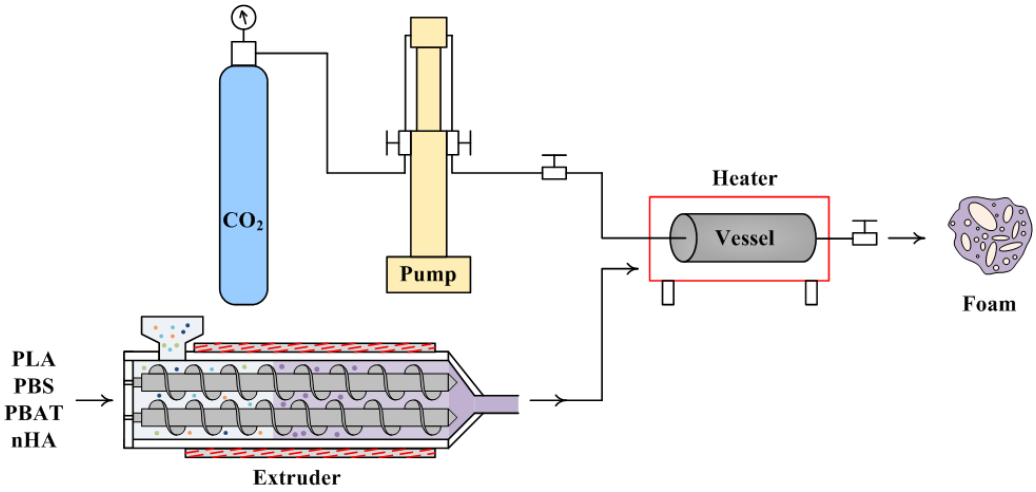

Figure 12. Schematic diagram of the experimental foaming process.

3.4. Determination of the Characteristic Structures and Properties of Foamed Polymer Blends

The characteristic structures of the fracture surfaces of the foamed polymer blends were observed using a scanning electron microscope (SEM, Nova NanoSEM 230, Hillsboro, OR, USA). Prior to SEM measurements, the foamed samples were dried under a vacuum and sputtered with gold.

The expansion ratio φ of the foamed sample was determined by Equation (1) [27,41]:

doi:10.6342/NTU202502722

$$\varphi = \frac{\rho_s}{\rho_f} \quad (1)$$

where ρ_s and ρ_f are the densities of the solid (unfoamed) and foamed samples, respectively. These densities were measured by the water replacement method according to ASTM D792 [55,57].

The cell density N_0 (cells/cm^3) is the number of cells per unit volume (cm^3) of foamed polymer, was determined from Equation (2) [27,40,41]:

$$N_0 = \frac{6[1 - (\rho_f / \rho_s)]}{\pi D^3} \times 10^{12} \quad (2)$$

where D is the average cell diameter (μm) measured from the SEM images.

The porosity of the foamed samples was evaluated using the expansion result by Equation (3) [27,41]:

$$\varepsilon = \frac{\varphi - 1}{\varphi} \quad (3)$$

The opening cell content (OCC) is an important factor for the tissue material. It is determined by the ratio of the open-cell volume (V_{open}) to the total volume (V_{total}) of the foamed sample, as shown by Equation (4) [43]:

$$\mathrm{OCC} = \frac{V_{open}}{V_{total}} = 1 - \frac{V_{true}}{V_{total}} \quad (4)$$

The open-cell volume is calculated by subtracting the true volume (V_{true}, the close-cell volume plus the cell wall volume) from the total volume. The open-cell volume values were measured by a nitrogen pycnometer (AccuPyc II 1340, Micrometric, Norcross, GA, USA)

3.5. Water Contact Angle and Mechanical Compression Measurements

Water contact angle measurements for various foamed polymer blends were performed using a contact angle analyzer (SEO Phoenix, S.E.O. Co. Ltd., Ansung City, Republic of Korea). The initial water contact angle and its changes with time were recorded for up to 30 min. The compressive stress–strain data of the foamed polymer blends were obtained using a dynamic mechanical analyzer (DMA, Perkin Elmer 7e, Waltham, MA, USA). The specimens were tested under a loading range from 7 kPa to 1.13 MPa at a constant rate of 10 kPa min^{-1}. A similar DMA experiment for porous PDLLA/bioglass composites has been shown in the literature [65].

4. Conclusions

In this study, supercritical CO_2 was used as an environmentally friendly physical foaming agent to investigate the foaming behavior of biodegradable PLA/PBS/PBAT ternary blends with the addition of nanohydroxyapatite (nHA). Eight different foaming strategies were explored, varying operating temperature, pressure, and duration. It was observed that intermediate temperature adjustments and pressure drop regulations are critical before the final rapid decompression to ambient conditions, ensuring a foamed product with an acceptable expansion ratio and cell size.

A stepwise intermediate decompression strategy was employed to produce foams with a bimodal cell structure. Under different foaming temperatures and pressures, the average size of the smaller cells in the bimodal structure ranged from 105 to 160 μm, while the large cells ranged from 476 to 889 μm. The gas solubility principle and classical nucleation theory were applied to explain the effects of stepwise pressure reduction. This study

doi:10.6342/NTU202502722

found that with the increase of the intermediate pressure drop, the nucleation energy barrier decreased, resulting in the bimodal structure's enlargement of the macrocell size. Furthermore, increasing the intermediate foaming temperature led to a decrease in the size of the larger cells. The temperature effect was attributed to the lower CO_2 solubility at higher intermediate temperatures and the possibly more pronounced polymer retraction effect during the final rapid decompression stage. The stepwise pressure variation strategy produced foams with diverse cell sizes and opening cell contents ranging from 60% to 84%, making them suitable for tissue engineering applications.

Water contact angles were measured for each foamed polymer blend, and their changes over 30 min were recorded. The results confirmed that all foamed products exhibited hydrophilic behavior, and the hydrophilicity increased with the increase in macrocell size and opening cell content. Compressive stress–strain measurements were conducted using a dynamic mechanical analyzer (DMA). Mechanical results show that the foamed polymer blends with smaller macrocells had higher stiffness, while those with larger macrocells showed higher toughness.

Author Contributions: P.-H.C.: conceptualization, data curation, validation and writing—original draft; C.-W.C.: methodology, investigation, validation, supervision, funding acquisition, writing—review and editing; T.-H.C.: data curation; H.-Y.L.: data curation; K.-L.T.: data curation; C.-S.S.: investigation, validation, funding acquisition and supervision; J.-C.T.: validation; F.-H.L.: investigation and validation. All authors have read and agreed to the published version of the manuscript.

Funding: This work was supported by the National Science and Technology Council of Taiwan (NSTC 113-2221-E-027-002).

Institutional Review Board Statement: Not applicable.

Informed Consent Statement: Not applicable.

Data Availability Statement: Data are contained within the article.

Conflicts of Interest: The authors declare that they have no conflicts of interest. The authors declare no competing financial interests.

References

1. Esmaeili, Y.; Bidram, E.; Bigham, A.; Atari, M.; Azadani, R.N.; Tavakoli, M.; Salehi, S.; Mirhaj, M.; Basiri, A.; Mirzavandi, Z.; et al. Exploring the evolution of tissue engineering strategies over the past decade: From cell-based strategies to gene-activated matrix. *Alex. Eng. J.* **2023**, *81*, 137–169. https://doi.org/10.1016/j.aej.2023.08.080.
2. Al-Shalawi, F.D.; Ariff, A.H.M.; Jung, D.-W.; Ariffin, M.K.A.M.; Kim, C.L.S.; Brabazon, D.; Al-Osaimi, M.O. Biomaterials as implants in the orthopedic field for regenerative medicine: Metal versus synthetic polymers. *Polymers* **2023**, *15*, 2601. https://doi.org/10.3390/polym15122601.
3. Ajmal, S.; Hashmi, F.A.; Imran, I. Recent progress in development and applications of biomaterials. *Mater. Today Proc.* **2022**, *62*, 385–391. https://doi.org/10.1016/j.matpr.2022.04.233.
4. Paternoster, J.L.; Vranckx, J.J. State of the art of clinical applications of tissue engineering in 2022. *Tissue Eng. Part B Rev*. **2022**, *28*, 592–612. https://doi.org/10.1089/ten.teb.2021.0017.
5. Jang, J.-W.; Min, K.-E.; Kim, C.; Shin, J.; Lee, J.; Yi, S. Review: Scaffold characteristics, fabrication methods, and biomaterials for the bone tissue engineering. *Int. J. Precis. Eng. Manuf.* **2023**, *24*, 511–529. https://doi.org/10.1007/s12541-022-00755-7.
6. Mukasheva, F.; Adilova, L.; Dyussenbinov, A.; Yernaimanova, B.; Abilev, M.; Akilbekova, D. Optimizing scaffold pore size for tissue engineering: Insights across various tissue types. *Front. Bioeng. Biotechnol*. **2024**, *12*, 1444986. https://doi.org/10.3389/fbioe.2024.1444986.
7. Kumeria, T. Advances on porous nanomaterials for biomedical application (drug delivery, sensing, and tissue engineering). *ACS Biomater. Sci. Eng*. **2022**, *8*, 4025−4027. https://doi.org/10.1021/acsbiomaterials.2c01103.
8. Swanson, W.B.; Ma, P.X. Textured and porous biomaterials. In *Biomaterials Science, An Introduction to Materials in Medicine*, 4th ed.; Academic Press: Cambridge, MA, USA, 2020; pp. 601–622. https://doi.org/10.1016/B978-0-12-816137-1.00039-8.

doi:10.6342/NTU202502722

9. Koons, G.L.; Diba, M.; Mikos, A.G. Materials design for bone- tissue engineering. *Nat. Rev. Mat.* **2020**, *5*, 584–603. https://doi.org/10.1038/s41578-020-0204-2.
10. Xiao, M.; Yao, J.; Shao, Z.; Chen, X. Silk-based 3D porous scaffolds for tissue Engineering. *ACS Biomater. Sci. Eng.* **2024**, *10*, 2827–2840. https://doi.org/10.1021/acsbiomaterials.4c00373.
11. Chen, H.; Song, G.; Xu, T.; Meng, C.; Zhang, Y.; Xin, T.; Yu, T.; Lin, Y.; Han, B. Biomaterial scaffolds for periodontal tissue engineering. *J. Funct. Biomater.* **2024**, *15*, 233. https://doi.org/10.3390/jfb15080233.
12. Liu, T.; Wang, Y.; Kuang, T. Oriented porous polymer scaffolds in tissue engineering: A comprehensive review of preparation strategies and applications. *Macromol. Mater. Eng*. **2024**, *309*, 2300246. https://doi.org/10.1002/mame.202300246.
13. Hernandez, J.L.; Woodrow, K.A. Medical applications of porous biomaterials: Features of porosity and tissue-specific implications for biocompatibility. *Adv. Healthc. Mater*. **2022**, *11*, e2102087. https://doi.org/10.1002/adhm.202102087.
14. Velázquez de la Paz, F. Jr. M. M. F.; Hann, A.J.; Thanarak, J.; Reilly, G.C.; Claeyssens, F.; Green, N.H.; Zhang, Y.S. Porous biomaterials for tissue engineering: A review. *J. Mater. Chem. B* **2022**, *10*, 8111. https://doi.org/10.1039/d1tb02628c.
15. Williams, D.F. Challenges with the development of biomaterials for sustainable tissue engineering. *Front. Bioeng. Biotechnol*. **2019**, *7*, 127. https://doi.org/10.3389/fbioe.2019.00127.
16. Szczesny, G.; Kopec, M.; Politis, D.J.; Kowalewski, Z.L.; Łazarski, A.; Szolc, T. A review on biomaterials for orthopaedic surgery and traumatology: From past to present. *Materials* **2022**, *15*, 3622. https://doi.org/10.3390/ma15103622.
17. Donnaloja, F.; Jacchetti, E.; Soncini, M.; Raimondi, M.T. Natural and synthetic polymers for bone scaffolds optimization. *Polymers* **2020**, *12*, 905. https://doi.org/10.3390/polym12040905.
18. Xu, C.; Liu, Z.; Chen, X.; Gao, Y.; Wang, W.; Zhuang, X.; Zhang, H.; Dong, X. Bone tissue engineering scaffold materials: Fundamentals, advances, and challenges. *Chin. Chem. Lett*. **2024**, *35*, 109197. https://doi.org/10.1016/j.cclet.2023.109197.
19. Modrák, M.; Trebunová, M.; Balogová, A.F.; Hudák, R.; Živcák, J. Biodegradable materials for tissue engineering: Development, classification and current applications. *J. Funct. Biomater*. **2023**, *14*, 159. https://doi.org/10.3390/jfb14030159.
20. Zhang, S.; Fang, H.; Tian, H. Recent advances in degradable biomedical polymers for prevention, diagnosis and treatment of diseases. *Biomacromolecules* **2024**, *25*, 7015−7057. https://doi.org/10.1021/acs.biomac.4c01193.
21. Wei, S.; Ma, J.-X.; Xu, L.; Gu, X.-S.; Ma, X.-L. Biodegradable materials for bone defect repair. *Mil. Med. Res.* **2020**, *7*, 54. https://doi.org/10.1186/s40779-020-00280-6.
22. Yu, H.; Liu, H.; Shen, Y.; Ao, Q. Synthetic biodegradable polymer materials in the repair of tumor-associated bone defects. *Front. Bioeng. Biotechnol*. **2023**, *11*, 1096525. https://doi.org/10.3389/fbioe.2023.1096525.
23. Sun, Z.; Wang, L.; Zhou, J.; Fan, X.; Xie, H.; Zhang, H.; Zhang, G.; Shi, X. Influence of polylactide (PLA) stereocomplexation on the microstructure of PLA/PBS blends and the cell morphology of their microcellular foams. *Polymers* **2020**, *12*, 2362. https://doi.org/10.3390/polym12102362.
24. Su, S.; Kopitzky, R.; Tolga, S.; Kabasci, S. Polylactide (PLA) and its blends with poly(butylene succinate) (PBS): A brief review. *Polymers* **2019**, *11*, 1193. https://doi.org/10.3390/polym11071193.
25. Zhang, X.; Liu, Q.; Shi, J.; Ye, H.; Zhou, Q. Distinctive tensile properties of the blends of poly(l-lactic acid) (PLLA) and poly(butylene succinate) (PBS). *J. Polym. Environ*. **2018**, *26*, 1737–1744. https://doi.org/10.1007/s10924-017-1064-8.
26. Ou-Yang, Q.; Guo, B.; Xu, J. Preparation and characterization of poly(butylene succinate)/polylactide blends for fused deposition modeling 3D printing. *ACS Omega* **2018**, *3*, 14309–14317. Available online: http://pubs.acs.org/journal/acsodf (accessed on 20 March 2025).
27. Yu, P.; Mi, H.-Y.; Huang, A.; Geng, L.-H.; Chen, B.-Y.; Kuang, T.-R.; Mou, W.-J.; Peng, X.-F. Effect of poly(butylenes succinate) on poly(lactic acid) foaming behavior: Formation of open cell structure. *Ind. Eng. Chem. Res.* **2015**, *54*, 6199−6207. https://doi.org/10.1021/acs.iecr.5b00477.
28. Zhao, H.; Liu, H.; Liu, Y.; Yang, Y. Blends of poly(butylene adipate-co-terephthalate) (PBAT) and stereocomplex polylactide with improved rheological and mechanical properties. *RSC Adv.* **2020**, *10*, 10482–10490. https://doi.org/10.1039/c9ra10827k.
29. Kang, Y.; Chen, P.; Shi, X.; Zhang, G.; Wang, C. Preparation of open-porous stereocomplex PLA/PBAT scaffolds and correlation between their morphology, mechanical behavior, and cell compatibility. *RSC Adv.* **2018**, *8*, 12933–12943. https://doi.org/10.1039/c8ra01305e.
30. Mou, Z.-L.; Zhao, L.-J.; Zhang, Q.-A.; Zhang, J.; Zhang, Z.-Q. Preparation of porous PLGA/HA/collagen scaffolds with supercritical CO_2 and application in osteoblast cell culture. *J. Supercrit. Fluids* **2011**, *58*, 398–406. https://doi.org/10.1016/j.supflu.2011.07.003.
31. Lowe, B.; Hardy, J.G.; Walsh, L.J. Optimizing nanohydroxyapatite nanocomposites for bone tissue engineering. *ACS Omega* **2020**, *5*, 1–9. https://doi.org/10.1021/acsomega.9b02917.

doi:10.6342/NTU202502722

32. Yan, D.; Wang, Z.; Guo, Z.; Ma, Y.; Wang, C.; Tan, H.; Zhang, Y. Study on the properties of PLA/PBAT composite modified by nanohydroxyapatite. *J. Mater. Res. Technol.* **2020**, *9*, 11895–11904. https://doi.org/10.1016/j.jmrt.2020.08.062.
33. Chen, P.-H.; Chen, C.-W.; Mao, H.-I.; Dai, C.-A.; Su, C.-S.; Tsai, J.-C.; Lin, F.-H. Bio-based PLA/PBS/PBAT ternary blends added with nanohydroxyapatite: A thermal, physical and mechanical study. *Polymers* **2023**, *15*, 4585. https://doi.org/10.3390/polym15234585.
34. Di Maioa, E.; Kiran, E. Foaming of polymers with supercritical fluids and perspectives on the current knowledge gaps and challenges. *J. Supercrit. Fluids* **2018**, *134*, 157–166. https://doi.org/10.1016/j.supflu.2017.11.013.
35. Sarver, J.A.; Kiran, E. Foaming of polymers with carbon dioxide—The year-in-review-2019. *J. Supercrit. Fluids* **2021**, *173*, 105166. https://doi.org/10.1016/j.supflu.2021.105166.
36. Kiran, E. Supercritical fluids and polymers-The year in review—2014. *J. Supercrit. Fluids* **2016**, *110*, 126–153. https://doi.org/10.1016/j.supflu.2015.11.011.
37. Zhou, Y.; Tian, Y.; Peng, X. Applications and challenges of supercritical foaming technology. *Polymers* **2023**, *15*, 402. https://doi.org/10.3390/polym15020402.
38. Peng, K.; Mubarak, S.; Diao, X.; Cai, Z.; Zhang, C.; Wang, J.; Wu, L. Progress in the preparation, properties, and applications of PLA and Its composite microporous materials by supercritical CO_2: A review from 2020 to 2022. *Polymers* **2022**, *14*, 4320. https://doi.org/10.3390/polym14204320.
39. Li, B.; Zhao, G.; Wang, G.; Zhang, L.; Gong, J.; Shi, Z. Super high-expansion poly(lactic acid) foams with excellent oil-adsorption and thermal-insulation properties fabricated by supercritical CO_2 foaming. *Adv. Sustain. Syst.* **2021**, *5*, 2000295. https://doi.org/10.1002/adsu.202000295.
40. Yang, Y.; Li, X.; Zhang, Q.; Xia, C.; Chen, C.; Chen, X.; Yu, P. Foaming of poly(lactic acid) with supercritical CO2: The combined effect of crystallinity and crystalline morphology on cellular structure. *J. Supercrit. Fluids* **2019**, *145*, 122–132. https://doi.org/10.1016/j.supflu.2018.12.006.
41. Chen, J.; Yang, L.; Mai, Q.; Li, M.; Wu, L.; Kong, P. Foaming behavior of poly(lactic acid) with different D-isomer content based on supercritical CO2-induced crystallization. *J. Cell. Plast.* **2021**, *57*, 675–694. https://doi.org/10.1177/0021955X20950242.
42. Huang, J.-N.; Jing, X.; Geng, L.-H.; Chen, B.-Y.; Mi, H.-Y.; Peng, X.-F. A novel multiple soaking temperature (MST) method to prepare polylactic acid foams with bi-modal open-pore structure and their potential in tissue engineering applications. *J. Supercrit. Fluids* **2015**, *103*, 28–37. https://doi.org/10.1016/j.supflu.2015.04.019.
43. Li, B.; Zhao, G.; Wang, G.; Zhang, L.; Gong, J.; Shi, Z. Biodegradable PLA/PBS open-cell foam fabricated by supercritical CO_2 foaming for selective oil-adsorption. *Sep. Purif. Technol.* **2021**, *257*, 117949. https://doi.org/10.1016/j.seppur.2020.117949.
44. Wang, S.; Yang, W.; Li, X.; Hu, Z.; Wang, B.; Li, M.; Dong, W. Preparation of high-expansion open-cell polylactic acid foam with superior oil-water separation performance. *Int. J. Biol. Macromol.* **2021**, *193*, 1059–1067. https://doi.org/10.1016/j.ijbiomac.2021.11.033.
45. Wang, Z.; Zhao, J.; Wang, G.; Xu, Z.; Zhang, A.; Dong, G.; Zhao, G. Lightweight, low-shrinkage and high elastic poly(butylene adipate-co-terephthalate) foams achieved by microcellular foaming using N_2 & CO_2 as co-blowing agents. *J. CO_2 Util.* **2022**, *64*, 102149. https://doi.org/10.1016/j.jcou.2022.102149.
46. Salerno, A.; Di Maio, E.; Iannace, S.; Netti, P.A. Solid-state supercritical CO_2 foaming of PCL and PCL-HA nano-composite: Effect of composition, thermal history and foaming process on foam pore structure. *J. Supercrit. Fluids* **2011**, *58*, 158–167. https://doi.org/10.1016/j.supflu.2011.05.009.
47. Chen, C.-X.; Peng, H.-H.; Guan, Y.-X.; Yao, S.-J. Morphological study on the pore growth profile of poly(ε-caprolactone) bi-modal porous foams using a modified supercritical CO_2 foaming process. *J. Supercrit. Fluids* **2019**, *143*, 72–81. https://doi.org/10.1016/j.supflu.2018.07.029.
48. Ju, J.; Gu, Z.; Liu, X.; Zhang, S.; Peng, X.; Kuang, T. Fabrication of bimodal open-porous poly (butylene succinate)/cellulose nanocrystals composite scaffolds for tissue engineering application. *Int. J. Biol. Macromol*. **2020**, *147*, 1164–1173. https://doi.org/10.1016/j.ijbiomac.2019.10.085.
49. Tammaro, D.; Lombardi, L.; Maffettone, P.L. Bimodal cell distributions in foaming of olefin block copolymers using high-throughput experimentation. *Chem. Eng. Sci.* **2025**, *304*, 121067. Available online: http://creativecommons.org/licenses/by/4.0/ (accessed on 20 March 2025).
50. Xu, L.Q.; Huang, H.-X. Formation mechanism and tuning for bi-modal cell structure in polystyrene foams by synergistic effect of temperature rising and depressurization with supercritical CO2. *J. Supercrit. Fluids* **2016**, *109*, 177–185. https://doi.org/10.1016/j.supflu.2015.07.020.

doi:10.6342/NTU202502722

51. Liao, X.; Nawaby, A.V.; Whitfield, P.S. Carbon dioxide-induced crystallization in poly(L-lactic acid) and its effect on foam morphology. *Polm. Int.* **2010**, *59*, 1709–1718. https://doi.org/10.1002/pi.2901.
52. Zhou, H.; Hu, D.; Zhu, M.; Xue, K.; Wei, X.; Park, C.B.; Wang, X.; Zhao, L. Review on poly (butylene succinate) foam: Modification, foaming behavior and applications. *Sustain. Mater. Technol.* **2023**, *38*, e00720. https://doi.org/10.1016/j.susmat.2023.e00720.
53. Li, G.; Li, H.; Turng, L.S.; Gong, S.; Zhang, C.; Measurement of gas solubility and diffusivity in polylactide. *Fluid Phase Equilib.* **2006**, *246*, 158–166. https://doi.org/10.1016/j.fluid.2006.05.030.
54. Lin, S.; Yang, J.; Yan, J.; Zhao, Y.; Yang, B. Sorption and diffusion of supercritical carbon dioxide in a biodegradable polymer. *J. Macromol. Sci. Phys.* **2010**, *49*, 286–300. https://doi.org/10.1080/01495930903352308.
55. Sato, Y.; Takikawa, T.; Sorakubo, A.; Takishima, S.; Masuoka, H.; Imaizumi, M. Solubility and diffusion coefficient of carbon dioxide in biodegradable polymers. *Ind. Eng. Chem. Res.* **2000**, *39*, 4813–4819. https://doi.org/10.1021/ie0001220.
56. Hu, D.; Xue, K.; Liu, Z.; Xu, Z.; Zhao, L. The essential role of PBS on PBAT foaming under supercritical CO_2 toward green engineering. *J. CO_2 Utili.* **2022**, *60*, 101965. https://doi.org/10.1016/j.jcou.2022.101965.
57. Yin, D.; Mi, J.; Zhou, H.; Wang, X.; Fu, H. Microcellular foaming behaviors of chain extended poly (butylene succinate)/polyhedral oligomeric silsesquioxane composite induced by isothermal crystallization. *Polym. Degrad. Stab*. **2019**, *167*, 228–240. https://doi.org/10.1016/j.polymdegradstab.2019.07.010.
58. Li, B.; Zhao, G.; Wang, G.; Zhang, L.; Gong, J. Fabrication of high-expansion PLA foams based on pre-isothermal cold crystallization and supercritical CO_2 foaming. *Polym. Degrad. Stab.* **2018**, *156*, 75–88. https://doi.org/10.1016/j.polymdegradstab.2018.08.009.
59. Zhou, H.; Song, J.; Ding, X.; Qu, Z.; Wang, X.; Mi, J.; Wang, J. Cellular morphology evolution of chain extended poly(butylene succinate)/organic montmorillonite nanocomposite foam. *J. Appl. Polym. Sci.* **2019**, *5*, 47107.https://doi.org/10.1002/APP.47107.
60. Jacobs, L.J.M.; Kemmere, M.F.; Keurentjes, J.T.F. Sustainable polymer foaming using high pressure carbon dioxide: A review on fundamentals, processes and applications. *Green Chem.* **2008**, *10*, 731–738. https://doi.org/10.1039/b801895b.
61. Yang, J.; Jiang, T.; Liu, B.; Zhang, C.; Zeng, X.; He, L.; Gong, W. Experimental and numerical analysis of bubble nucleation in foaming polymer. *Mater. Des.* **2021**, *203*, 109577. https://doi.org/10.1016/j.matdes.2021.109577.
62. Abbasi, N.; Stephen Hamlet, S.; Love, R.M.; Nguyen, N.-T. Porous scaffolds for bone regeneration. *J. Sci.: Adv. Mater. Devices* **2020**, *5*, 1–9. https://doi.org/10.1016/j.jsamd.2020.01.007.
63. Huang, L.; Wang, A.; Xu, R.; Lei, C. PBS melt strength improving for supercritical CO_2 Foaming molding by physical adsorption and crystallization. *Polym. Bull.* **2024**, *81*, 11629–11643. https://doi.org/10.1007/s00289-0l24-05251-8.
64. Goncalves, L.F.F.F.; Reis, R.L.; Fernandes, E.M. Forefront research of foaming strategies on biodegradable polymers and their composites by thermal or melt-based processing technologies: Advances and perspectives. *Polymers* **2024**, *16*, 1286. https://doi.org/10.3390/polym16091286.
65. Blaker, J.J.; Maquet, V.; Jerome, R.; Boccaccini, A.R.; Nazhat, S.N. Mechanical properties of highly porous PDLLA/bioglass composite foams as scaffold for bone tissue engineering. *Acta Biomater*. **2005**, *1*, 643–652. https://doi.org/10.1016/j.actbio.2005.07.003.

Disclaimer/Publisher's Note: The statements, opinions and data contained in all publications are solely those of the individual author(s) and contributor(s) and not of MDPI and/or the editor(s). MDPI and/or the editor(s) disclaim responsibility for any injury to people or property resulting from any ideas, methods, instructions or products referred to in the content.

doi:10.6342/NTU202502722